

**Effect of an Embankment Reconstruction Using a Wicking Geotextile in the Drainage and
Strength of Subgrade**

by

Camila B. S. de Alvarenga

A thesis submitted in partial fulfillment of the requirements for the degree of

Master of Science

in

Geotechnical Engineering

Department of Civil and Environmental Engineering

University of Alberta

© Camila B. S. de Alvarenga, 2021

ABSTRACT

Railways are essential for the transportation of goods and people and are an integral component of Canada's economy (Leishman et al. 2017). As a part of the Canadian Pacific Railway's (CP) Grade Stabilization/Remediation Plan, a 45 m section of a railway embankment located at Fort Saskatchewan County in Alberta, Canada, was remediated. The reconstruction consisted of replacing ballast and sub-ballast with clean materials and installing two geotextiles: a 4.6 m wide reinforcing geotextile (Mirafi® RS580i) and a 7.3 m wide wicking geotextile (Mirafi® H2Ri). The first was placed in the ballast and sub-ballast interface, while the second was placed between the subgrade and sub-ballast, aiming to address issues such as poor drainage and moisture retention. This site provided the opportunity of observing the enhancement of drainage brought by the performed reconstruction, as it enables testing adjacent remediated and control sections. This process facilitates the direct comparison between these locations. The site materials were tested in the laboratory. Both sections were instrumented with 5TE sensors, which can determine the volumetric water content (VWC), bulk electrical conductivity, and temperature from the soil around, aiming to compare the sections regarding their moisture levels directly. A Diviner 2000 probe was also used to read moisture profiles at each site visit. Precipitation data was acquired from weather stations near the study site and compared to the VWC levels seen at the site. A known method that relates the VWC and precipitation called the antecedent precipitation index (API) was used to ease the understanding of precipitation events' influence in the variation of moisture content and strength of the embankment at both sections.

The key findings of the first year of monitoring are that the remediated section VWC levels were less sensitive to precipitation events than the ones from the control section. No changes were observed in VWC of the remediated subgrade, even with high amounts of precipitation. However,

higher VWC levels were observed at the remediated subgrade compared to the control section in October/2020 after a long period without precipitation took place. A series of factors could contribute to this observation.

The remediated section presented consistent strength levels throughout the study and presented a significantly higher minimum strength level than the control section. Therefore, the remediation done potentially improves the embankment bearing capacity during periods of heavy rainfall. This improvement may be beneficial for mitigating the issues seen at the site before the reconstruction.

ACKNOWLEDGEMENTS

I would like to express my gratitude to CP and NSERC for sponsoring this research and to all people that helped with our field and laboratory work: Danny Wong, Adam Dowie, and Troy Dunkin from Canadian Pacific Railway; Shaun Clark from Edmonton Railway Contracting LTD.; Dr. Ahlam Abdulnabi and Dr. Louis Kabwe, from the University of Alberta; my fellow students Jorge Rodriguez, Danial Behnia, Kevin Wallin, Evan Deane, Reza Mousapour and Adam Woods also from UofA, and Kelvin Sattler, from the University of Saskatchewan.

I am grateful to all the people that were with me along the way. During my studies, I met the most extraordinary people, and I am happy to have them in my life. First, I would like to thank Dr. Michael Hendry and Dr. Parisa Abdulzaragh for all the patience, knowledge, and great pieces of advice when I most needed them; I also thank you for providing me the opportunity to conduct this research.

I would also like to extend my appreciation to Dr. Derek Martin for being the one who first accepted me at UofA and for being such an inspiring professor. Thanks to Jennifer Stogowski and Vivian Giang for helping since my first day at the university; it meant the world to me.

This work is also dedicated to my family in Brazil, my friends and my partner for life. Nathália Machado and Fernanda Imamura, for being with me when I most struggled with the courses and for making my lunch break so much better. Liniker Monteiro, thank you for willing to live this adventure in Canada with me. I cannot thank you enough for your love, support and kindness.

No words can express how lucky I am for having so many special people in my life.

LIST OF TABLES

Table 2.1. List of geotextiles for the testing program. From (Azevedo & Zornberg, 2013).....	24
Table 3.1. Physical Specifications of 5TE Sensors (Meter Environment, 2019).....	31
Table 3.2- Measurement Specifications of 5TE Sensors (Meter Environment, 2019).	32
Table 3.3. Characteristics of Mirafi® RS580i. From Tencate (2018).	38
Table 3.4. Characteristics of Mirafi® H2Ri. From Tencate (2015).....	38
Table 3.5. Summary of access pipes at control section.....	40
Table 3.6. Summary of access pipes at remediated section.	40
Table 3.7. Repair Dimensions.....	42
Table 4.1. Soil Sample Details.....	48
Table 5.1. Summary of geotechnical index properties of the embankment materials.	59
Table 5.2. Issues found during data collection.....	64
Table 6.1. Number of days considered in the API model for each track location.	72
Table 6.2. Summary of attenuation coefficients used for each track location.	72
Table 6.3. Summary of variation of VWC within sections for direct comparison.....	82

LIST OF FIGURES

Figure 1.1-Scotford subdivision location on CP network. (Canadian Pacific Railway, 2020).....	3
Figure 1.2- Satellite Images of Instrumented Site at Scotford Mile 153.8. (Google Earth, 2020).....	3
Figure 1.3. Track conditions at the research site before renovation (Abdulrazagh 2019 – with permission).	4
Figure 1.4. Location of weather stations for weather data on-site. (Google Earth, 2020).....	4
Figure 2.1. Cross-section of a ballasted track.	7
Figure 2.2. Progressive shear failure mechanism (Li et al. 1996).....	10
Figure 2.3. Formation of subgrade squeeze zones beneath track substructure filled with ballast (Li et al. 1996)	10
Figure 2.4. Illustration of the development of a) frost heave and b) thawing of the track (Li et al. 2002). 12	
Figure 2.5. Failure envelopes for a) Saturated soils, b) Unsaturated soils, and c) Stress point envelope (Gui & Yu, 2008).	16
Figure 2.6. Non-linearity of Shear Strength Envelope (Vanapalli et al. 1996).....	16
Figure 2.7. Comparison of SWCCs for different soil types (Fredlund and Xing, 1994).	17
Figure 2.8. Edge treatments by quadrant for Mirafi® H2Ri geosynthetic at a) test site 4 and b) test site 6 (Bradley et al. 2017).	23
Figure 2.9. Moisture data for site 4. (Bradley et al. 2017).....	23
Figure 2.10. Position of moisture sensors at SH 21 (Zornberg et al. 2017).....	26
Figure 2.11. Moisture content distribution along the shoulder of SH 21: (a) In the section with conventional geotextile, (b) In the section with wicking geotextile (Zornberg et al. 2017).	26
Figure 2.12. Water removal rate at different test stages (Wang et al. 2017).....	27
Figure 3.1. 5TE Moisture Sensors (Hoskin Scientific Ltd, n.d.).	30
Figure 3.2. Diviner 2000 setup. (Sentek Pty Ltd, 1999).	33
Figure 3.3. Calibration setup for 5TE and Diviner 2000 sensors.....	35
Figure 3.4. Geotextiles used in the soil reinforcement a) Mirafi® RS580i b) Mirafi® H2Ri.	37
Figure 3.5. Plan view layout of the access pipe installation (dimensions in meters).	39
Figure 3.6. Cross-section of control site setup: access pipe at subgrade layer (dimensions in meters).	39
Figure 3.7. Cross-section of control section: access pipe at sub-ballast layer (dimensions in meters).....	39
Figure 3.8. Cross-section of remediated section (dimensions in meters).....	39
Figure 3.9. Track Section Excavation on April 23, 2019 (Abdulrazagh 2019 – with permission).....	41
Figure 3.10. Subgrade sensor buried with an electric shield on April 23, 2019 (Abdulrazagh 2019 – with permission).....	42
Figure 3.11. Sub-ballast placement over geotextile on April 23, 2019 (Abdulrazagh 2019 – with permission).....	42
Figure 3.12. Mirafi® RS580i over compacted sub-ballast layer on April 23, 2019 (Abdulrazagh 2019 – with permission).....	43
Figure 3.13. Harsco equipment tamping and lining the track on April 24, 2019 (Clifton Associates, 2019).	43
Figure 3.14. Trench boring for access pipe on April 24, 2019 (Abdulrazagh 2019 – with permission).....	44
Figure 3.15. Installation of access pipes in the track on April 24, 2019 (Abdulrazagh 2019 – with permission).....	44
Figure 3.16. Site after installation of access pipes (Alvarenga et al. 2020).	44

Figure 3.17. 5TE sensors installation using a notched pipe on May 15, 2019 (Abdulrazagh 2019 – with permission).....	45
Figure 3.18. Protection of wires using PVC electrical conduit on May 15, 2019 (Abdulrazagh 2019 – with permission).....	45
Figure 3.19 - Protection of wires by metal electrical conduits where the cables could not be buried beneath the soil on May 15, 2019 (Abdulrazagh 2019 – with permission).	46
Figure 3.20. Datalogger set up on May 15, 2019 (a) before placing sensor wires and (b) after (Abdulrazagh 2019 – with permission).....	46
Figure 3.21. Dataloggers ready for data collection.....	47
Figure 3.22. Insertion and compaction of sub-ballast soil into access pipes on July 23, 2019 (Abdulrazagh 2019 – with permission).....	47
Figure 4.1- Samples of the embankment materials. (a) Clean ballast (b) Clean sub-ballast, (c) Control Ballast and (d) Control Sub-ballast.....	50
Figure 4.2-Subgrade sample in (a) wet and (b) dry conditions.....	51
Figure 4.3. Hydrometer Test Setup.....	52
Figure 4.4. Vacuum procedure in soil mixture for specific gravity test.....	53
Figure 4.5. Wet preparation method of the specimen for liquid and plastic limit tests. (a) Soaked soil (b) Washed soil after drying for a few days.	54
Figure 4.6. Liquid Limit Test.....	54
Figure 4.7. Plastic Limit sample after crumbling.....	55
Figure 4.8. Hanging Column Test.....	56
Figure 4.9. Direct Shear a) Test Setup and b) Subgrade sample after shearing.....	57
Figure 4.10- Field Dry Density Test procedure.	58
Figure 5.1. Grain-size analysis of embankment soils.	60
Figure 5.2. SWCC for clean sub-ballast.	61
Figure 5.3. SWCC for control sub-ballast.....	61
Figure 5.4. SWCC for subgrade.....	61
Figure 5.5. Shear vs. Horizontal displacements plots for Direct Shear test under normal stress of 100 kPa for Control Sub-ballast.....	63
Figure 5.6. Shear vs. Horizontal displacements plots for Direct Shear test under normal stress of 100 kPa for clean sub-ballast.	63
Figure 5.7. Shear vs. Horizontal displacements plots for Direct Shear tests under normal stress of 100 kPa for Subgrade.....	63
Figure 5.8. Shear Stress of Embankment Materials.....	64
Figure 5.9- Volumetric Water Content from a) T1 and TG1 (Sub-ballast shoulder), b) T2 and TG2 (Sub-ballast shoulder), c) T3 and TG3 (Sub-ballast centreline) and d) T4, T5 and TG5 (Subgrade centreline). 66	
Figure 5.10- Temperature readings through time for all sensors at a) T1 and TG1 (Sub-ballast shoulder), b) T2 and TG2 (Sub-ballast shoulder), c) T3 and TG3 (Sub-ballast centreline) and d) T4, T5 and TG5 (Subgrade centreline).	67
Figure 5.11- Diviner 2000 readings performed at Scotford Mile 153.8.	69
Figure 6.1. 10-year average temperature (2008-2018) vs. recorded temperatures (2019-2020) (ECCC, 2020).	70
Figure 6.2. 10-year average precipitation (2008- 2018) vs. recorded precipitation (2019 and 2020) (ECCC, 2020).	71

Figure 6.3. VWC measurements comparison with antecedent precipitation index values found for Sub-ballast shoulder	73
Figure 6.4. VWC measurements comparison with antecedent precipitation index values found for Sub-ballast centreline.	74
Figure 6.5. VWC measurements comparison with antecedent precipitation index values found for a) Sub-ballast shoulder, b) Sub-ballast centreline, and c) Subgrade centreline.....	75
Figure 6.6. Linear regression of daily measured VWC vs. API for the year 2019. a) T1 and TG1 (Sub-ballast shoulder), b) T2 and TG2 (Sub-ballast shoulder), c) T3 and TG3 (Sub-ballast centreline) and d) T4 (Subgrade centreline) and e) T5 and TG5 (Subgrade centreline).	76
Figure 6.7- Linear regression of daily measured VWC vs. API for the year 2020. a) T1 and TG1 (Sub-ballast shoulder), b) T2 and TG2 (Sub-ballast shoulder), c) T3 and TG3 (Sub-ballast centreline) and d) T4 (Subgrade centreline) and e) T5 and TG5 (Subgrade centreline).	78
Figure 6.8. Estimated in-situ suction values for the subgrade centreline at the control section (T5) and remediated section (TG5).	80
Figure 6.9- Variation of in-situ strength values at the subgrade (93 cm depth) through the time of the study for control section (T5) and remediated section (TG5).....	81
Figure II.1. Diviner and 5TE sensor calibration for Clean Sub-ballast.....	123
Figure II.2. Diviner vs. 5TE measurements for Clean Sub-ballast.	123
Figure II.3. Diviner and 5TE sensor calibration for Subgrade.....	124
Figure II.4 Diviner vs. 5TE measurements for Subgrade.	124

TABLE OF CONTENTS

ABSTRACT.....	ii
ACKNOWLEDGEMENTS.....	iv
LIST OF TABLES.....	v
LIST OF FIGURES.....	vi
1. INTRODUCTION.....	1
1.1 Research Objectives	2
1.2 Description of the Study Site	2
1.3 Scope and Methodology	4
1.4 Thesis Outline	5
2. LITERATURE REVIEW.....	7
2.1 Railway Tracks and Embankments	7
2.1.1 Track Superstructure.....	7
2.1.2 Track Substructure.....	7
2.2 Moisture and Drainage Related Issues	8
2.2.1 Factors Affecting Soil Moisture Content.....	9
2.2.2 Bearing Capacity/Cess Heave.....	9
2.2.3 Frost Heave.....	11
2.2.4 Clay Pumping.....	12
2.3 Unsaturated Soil Mechanics in Railroads	13
2.3.1 Shear Strength of Unsaturated Soils.....	13
2.3.2 Soil Water Characteristic Curve and Testing Methods.....	17
2.3.3 Past Studies on Unsaturated Soil Mechanics and Railway Embankments.....	19
2.4 Evaluation of the Relationship Between Soil Moisture and Precipitation	21
2.5 Previous Studies on Wicking Geotextile	22
2.5.1 Wicking Geotextile Incorporation in Highways.....	22
2.5.2 Capillary Barrier Dissipation by New Wicking Geotextile.....	24
2.5.3 Wicking Geotextile Drainage Capabilities in Roadway Systems.....	25
2.5.4 Laboratory Tests to Evaluate the Effectiveness of Wicking Geotextile.....	26
2.5.5 Performance of Wicking Geotextile on Mitigating Water Pumping Issue.....	28
2.5.6 Evaluation of H2Ri wicking fabric for pavement application.....	29
3. DESCRIPTION OF INSTRUMENTATION AND RECONSTRUCTION OF STUDY SITE.....	30

3.1 Instrumentation and Calibration	30
3.1.1 5TE Moisture Sensors	30
3.1.2 Diviner 2000	33
3.1.3 Laboratory Calibration of Field Instruments.....	34
3.2 Description of Remediated Section Reconstruction and Instrumentation	37
3.2.1 Geotextiles	37
3.2.2 Field Instrumentation Design.....	38
3.2.3 Construction of Remediated Section and Installation of Subgrade Sensors	40
3.2.4 Installation of Access Pipes	43
3.2.5 Installation of Sensors and Dataloggers.....	45
3.2.6 Backfilling of Access Pipes	47
4. CHARACTERIZATION OF EMBANKMENT SOILS	48
4.1 Information on Soil Sampling	48
4.2 Laboratory Testing Methodology	49
4.2.1 Moisture Content.....	49
4.2.2 Particle Size Distribution (PSD)	49
4.2.3 Specific Gravity of Soil.....	52
4.2.4 Atterberg Limits.....	53
4.2.5 Soil-Water Characteristic Curve (SWCC)	55
4.2.6 Consolidated Drained Direct Shear Test (CDDST)	56
4.2.7 In-situ Dry Density Test.....	57
5. LABORATORY AND FIELD INSTRUMENTATION RESULTS	59
5.1 Laboratory Tests Results	59
5.1.1 Soil Index Properties	59
5.1.2 Soil-Water Characteristic Curve	60
5.1.3 Consolidated Drained Direct Shear.....	62
5.2 Field Data Collection	64
5.2.1 Field 5TE Sensors Data.....	64
5.2.2 Diviner 2000 Data.....	68
6. ANALYSIS AND DISCUSSION OF RESULTS	70
6.1 Field Climate Information	70
6.2 Antecedent Precipitation Model	71
6.3 Soil Shear Strength Analysis	79

6.4 Comparison of In-situ VWC Levels and their Variation with Precipitation.....	81
6.5 Contribution of VWC on Subgrade Strength.....	83
6.6 Comparison of Reconstruction Effect with Previous Studies Using Wicking Geotextile.....	83
7. CONCLUSIONS AND RECOMMENDATIONS	85
7.1 Recommendations for Future Research	87
REFERENCES	90
APPENDIX I – Material Characterization Results.....	96
APPENDIX II – Sensor Calibration Results.....	122

1. INTRODUCTION

Railways are essential for the transportation of goods and people throughout Canada, having an important role in the economy. It is, therefore, crucial to design these structures to maintain suitable conditions while keeping the maintenance work as short as possible. As recognized by several authors (Indraratna et al. 2011; Li et al. 2002; Rushton and Ghataora, 2014), drainage is one of the major aspects of a railway design. Its design must consider both the site conditions regarding the soil profile and local climatic conditions. Clays and silts are the focus of most subgrade improvement work, as these soils require a drainage system that can release water from the track substructure as fast as possible to minimize strength loss (Li et al. 2002).

Water accumulation leads to several issues such as clay pumping, track settlement, cess heave, ballast degradation and frost heave/thaw softening, as well as a decrease in bearing capacity due to strength reduction. These factors reduce the serviceability of a railway embankment and consequently increases the maintenance costs. (Indraratna et al, 2011; Li et al, 2002)

Several methods improve drainage, such as perforated and non-perforated pipes, ditches, trench drains/coarse-aggregate drains, hot mix asphalt, and geosynthetics (Li et al. 2002; Selig and Waters, 1994). In railway track applications, geotextiles are commonly used for separation and retention between layers, but they can also improve track drainage. For example, using a wicking geotextile (Mirafi® H2Ri) may enhance lateral drainage of materials even in unsaturated conditions. This geotextile is able to remove water by capillary action through deeply grooved wicking fibers included in the fabric. These fibers are responsible for drawing moisture from both the embankment and the subgrade's surface towards the shoulders.

As part of the Canadian Pacific Railway's (CP) Grade Stabilization/Remediation Plan, the railway embankment materials were replaced while a reinforcing and a wicking geotextile were installed. The mechanism and effects of this reconstruction are still not very well understood; therefore, this research aimed to evaluate the impact of the reconstruction in terms of the drainage properties and soil strength of the embankment materials.

1.1 Research Objectives

This research project's overall objective is to observe the moisture content of a railway subgrade beneath a segment of embankment reconstructed using a wicking geotextile and compare it to the moisture content in a subgrade beneath an untreated section of the railway. The purpose is to evaluate the impact of an embankment reconstruction using wicking geotextiles on the moisture and strength levels of the subgrade soils beneath railway embankments.

The specific objectives were set as follows:

- 1) Measure the temporal changes of volumetric water content (VWC) within the embankment and subgrade of both a reconstructed and an adjacent untreated track segment.
- 2) Evaluate the temporal changes in measured VWC beneath the railway embankment with respect to precipitation events to investigate whether the remediation including geotextiles contributes to enhanced lateral drainage.
- 3) Characterize and test soils from the site to determine the effect of moisture changes on soil strength by performing SWCC tests to understand the moisture-suction relationship and Direct Shear tests to determine the embankment materials' effective strength parameters.
- 4) Use the SWCC, Strength parameters, and measured VWC to evaluate the unsaturated strength of the subgrade soil and the change in resistance to plastic deformation and cess heave.

1.2 Description of the Study Site

The research site is located at CP's Scotford subdivision (Figure 1.1, highlighted in green), which goes from Scotford Mile 136.8 to Gainer Mile 173.6, with the instrumented section located at Scotford Mile 153.6, close to Fort Saskatchewan, AB. The railway subgrade soil is identified as clay till and is composed of approximately 31% clay, 20% silt, 29% of sand, and 20% of gravel. Figure 1.2 displays the site location pinned in red.

The selected site was provided by CP based on the history of issues found at the site, such as settlement, frost heave, and clay pumping/ballast fouling (Figure 1.3). These issues were attributed to poor drainage and retention of moisture within both the embankment and subgrade.

The site was remediated by excavating the track down to the subgrade and replacing the ballast and sub-ballast materials while laying one reinforcing geotextile (Mirafi® RS580i) between the

ballast/sub-ballast and one wicking geotextile (Mirafi® H2Ri) at the sub-ballast/subgrade interface to mitigate these issues. This section's subgrade material presents low permeability and greater moisture retention due to the presence of fines, turning the site into an ideal area to evaluate the effectiveness of the remediation method chosen to improve the embankment drainage.

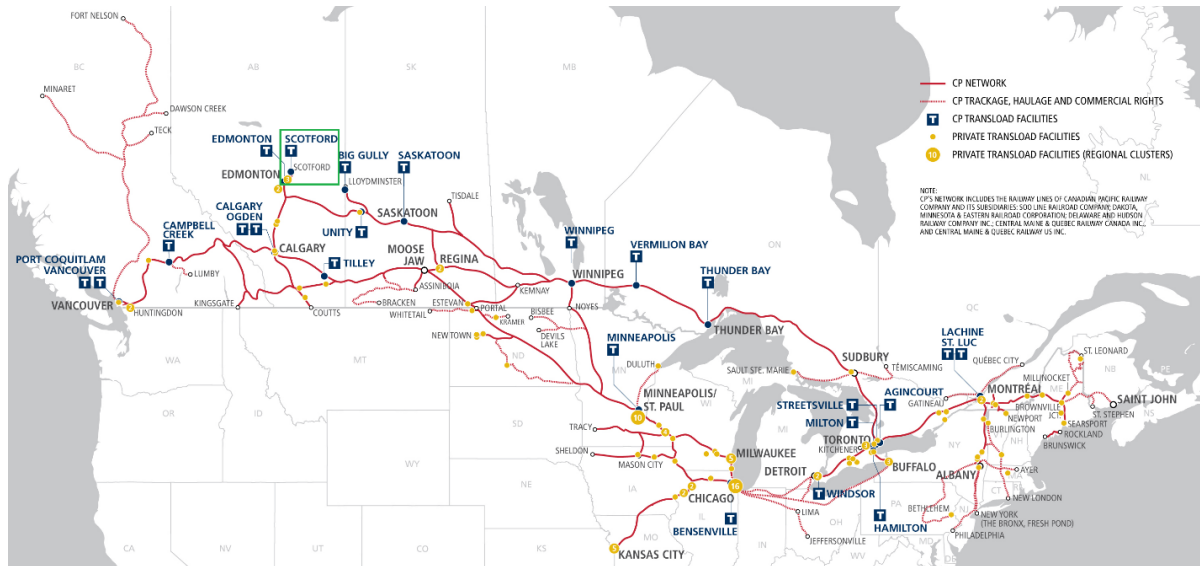


Figure 1.1-Scotford subdivision location on CP network. (Canadian Pacific Railway, 2020).

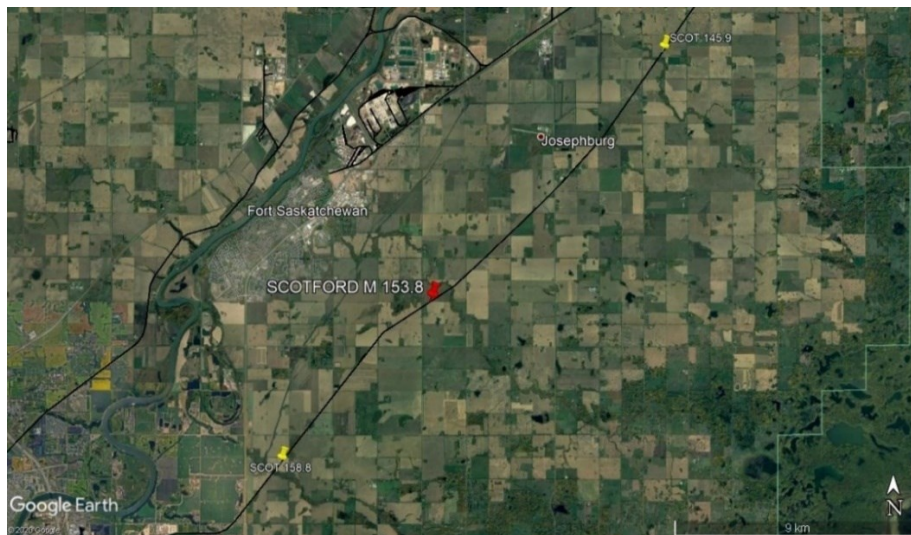


Figure 1.2- Satellite Images of Instrumented Site at Scotford Mile 153.8. (Google Earth, 2020).

The evaluation was undertaken by monitoring the seasonal changes of moisture content within the track along a remediated and a control section. Moisture sensors were installed through the centreline and shoulders of the track substructure at both sections so as to analyze the effects of the reconstruction on soil strength and moisture management.

There are three different weather stations within 25 km of the site (Figure 1.4). The Fort Saskatchewan weather station is located 6.06 km away from the site and provided daily air temperature, rainfall, snowfall and total precipitation (Alvarenga, 2020). The Oliver AGDM station was 13.53 km away and provided temperature data. The UNCAS station, located 21.57 km away from the site, provided temperature data as well as precipitation data in days that it was not available for the first station.



Figure 1.3. Track conditions at the research site before renovation (Abdulrazagh 2019 – with permission).

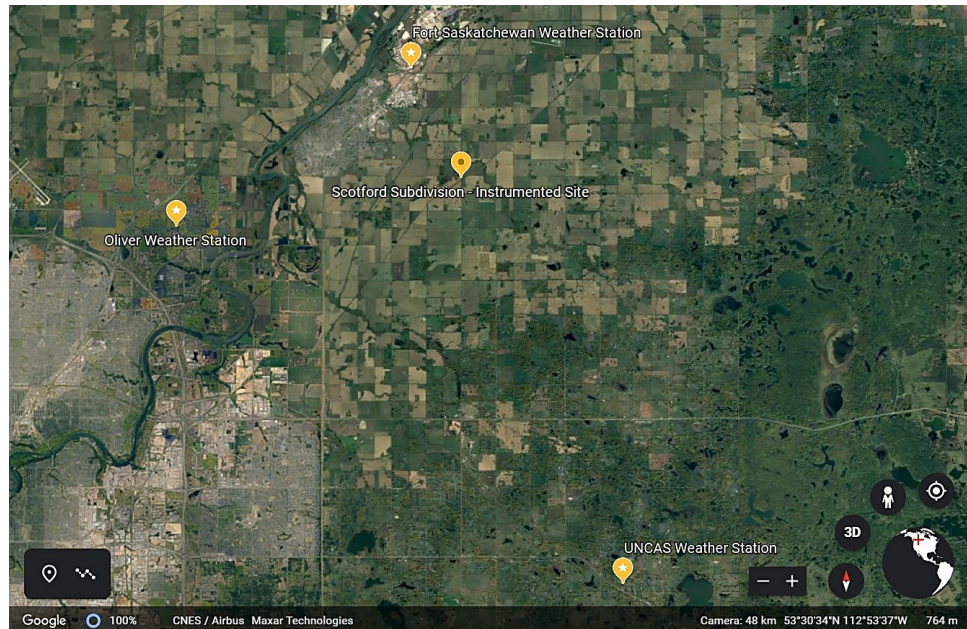


Figure 1.4. Location of weather stations for weather data on-site. (Google Earth, 2020)

1.3 Scope and Methodology

In pursuance of measuring the temporal changes of VWC within both the embankment and subgrade, our site was divided into two sections of track, one remediated and one control section.

This division provided the opportunity for direct comparison between adjacent locations. Both sections were instrumented with a total of 10 5TE sensors, which determined the VWC, bulk electrical conductivity, and temperature from the soil at a determined time interval. In this study, the interval of readings was 12 hours.

The characterization of the materials at the field, including ballast, sub-ballast, and subgrade, was performed to analyze the soil properties and strength behaviour when there was a change in moisture content. Direct shear (DS) and soil-water characteristic curve (SWCC) tests were performed in the sub-ballast and subgrade materials to quantify the effect of moisture on the soil strength.

In order to evaluate the temporal changes in measured VWC with respect to precipitation events, daily meteorological data were acquired from weather stations near the study site along with the VWC data from the 5TE sensors. A known method that relates the VWC and precipitation data from a certain amount of days, called the antecedent precipitation index (API), was used to facilitate the understanding of precipitation events' influence in the moisture content of the embankment at both sections.

The unsaturated strength of the subgrade was estimated by using the results from both DS and SWCC tests based on the unsaturated soil mechanics concepts. Then, the remediated and control section's strength levels were directly compared to verify which section presented a more significant decrease in strength when precipitation events occurred.

1.4 Thesis Outline

This thesis consists of 6 chapters and 2 appendices:

Chapter one comprises the introduction, including the problem description, research objectives, site description, scope of work and methodology.

Chapter two presents the literature review, inclusive of railway track components, moisture effect on soils, unsaturated soil mechanics principles, precipitation models, and studies regarding the use of wicking geotextiles.

Chapter three comprises the field and instrumentation details, method of embankment construction, and data collection.

Chapter four presents the laboratory characterization and testing methods performed in the soil samples from the studied site.

Chapter five presents the field and laboratory results along with observed trends.

Chapter six presents the moisture and strength data analysis using the antecedent precipitation index (API) model and the soil strength estimative, including a discussion of these results.

Chapter seven presents the conclusions and recommendations from this project.

Appendix I includes the material characterization results.

Appendix II comprises the results of the calibration of the moisture sensors used in the site instrumentation.

2. LITERATURE REVIEW

2.1 Railway Tracks and Embankments

The railway track structure is divided into superstructure and substructure components (Figure 2.1). The superstructure is composed of rails, ties, and a fastening system. Below the superstructure, three different soil layers comprise the substructure: ballast, sub-ballast, and subgrade. (Indraratna and Salim, 2005)

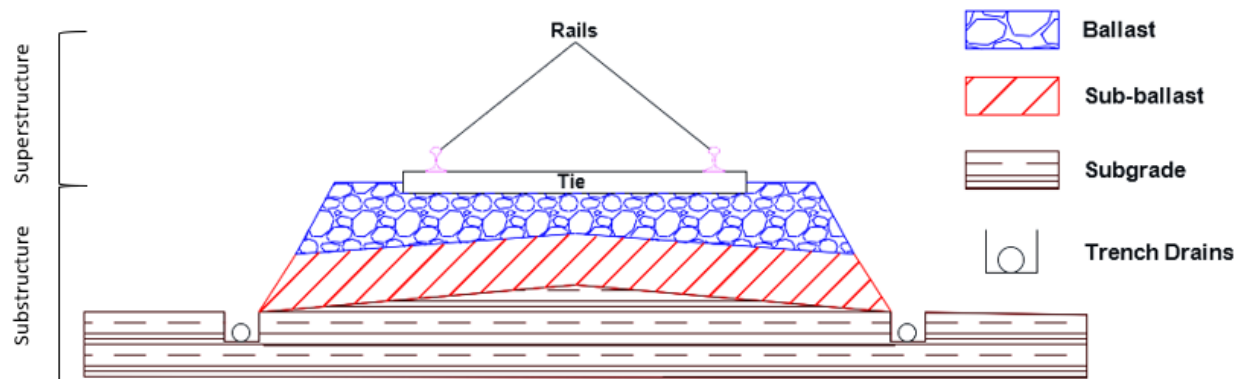


Figure 2.1. Cross-section of a ballasted track.

2.1.1 Track Superstructure

The track superstructure components reduce the large stresses at the wheel-rail interface to tolerable levels for the substructure layers (Li et al. 2002). Rails support the traffic load directly and are responsible for transferring the traffic loading to the supporting ties (Indraratna and Salim, 2005). The fastening system is composed of rail clips and rail anchors that secure the rail-tie connection, avoiding lateral, longitudinal and vertical movement of the rails. The ties are responsible for distributing the traffic loading at the tie-ballast interface and resisting lateral and vertical forces resulting from that load (Indraratna et al. 2011).

2.1.2 Track Substructure

2.1.2.1 Ballast

The upper layer of a ballasted track is defined as ballast, and it is typically composed of coarse aggregates. Indraratna et al. (2011) mention that the ballast should facilitate track drainage, transmit high imposed stress to the subgrade layer at a reduced and acceptable stress level, and

provide good stability against vertical, longitudinal, and lateral forces generated by typical train speeds.

2.1.2.2 Sub-ballast

Sub-ballast is a layer of soil that is not present in all railways. It works as an extension of the ballast, facilitating the subgrade drainage while at the same time protecting the ballast from fouling (Trani and Indraratna, 2010).

This layer becomes necessary when the subgrade is composed of low permeability or soft soils. It is responsible for providing separation between ballast and subgrade, minimizing clay pumping and enhancing drainage of water entering the track either from precipitation, surface runoff, or capillary rise (Li et al. 2002 and Indraratna et al. 2011).

2.1.2.3 Subgrade

The subgrade is the most variable layer of the track substructure, and it can be composed of either the natural soil available at the site or fill material. Li et al. (2002) define that a subgrade layer must stay stable under train loading and self-weight and it should not deteriorate through consolidation settlement or massive track instability.

The subgrade needs to avoid some failure modes such as excessive progressive settlement from traffic loading, significant volume change from moisture change, frost heave, and thaw softening to serve as a stable platform. (Selig and Waters, 1994)

2.2 Moisture and Drainage Related Issues

Water accumulation is one of the leading causes of track substructure problems (Li et al. 2002). Despite the drainage of the track usually not receiving proper attention, it is one of the most critical aspects of the track design. It plays a significant role in maintenance costs and track stability. When the drainage is inappropriate, many issues may occur, such as a decrease in ballast shear strength, stiffness, and load-bearing capacity, track settlement, subgrade soil softening, clay pumping, and damage to the structure due to water jetting (Indraratna et al. 2012; Indraratna et al. 2011; Rushton and Ghataora, 2014). Other consequences of water accumulation in the track include erosion and a consequent track deflection. (Li et al. 2002).

2.2.1 Factors Affecting Soil Moisture Content

We may identify four water sources in the railway: precipitation (rain and snowmelt), surface runoff, upward seepage from subgrade, and high groundwater table where the railway is in low-lying coastal regions (Indraratna et al. 2011). Other factors that impact soil moisture include air temperature, soil temperature, and vegetation growth. However, soil moisture is influenced by many complex factors. As depth increases, each of these water sources influences either less or more the soil's moisture content.

2.2.2 Bearing Capacity/Cess Heave

Water in the subgrade can considerably reduce soil strength and stiffness. A subgrade may become wet or saturated by the infiltration of water from either the surface or groundwater. If the water table is deeper than 6.1 m, the subgrade surface's moisture content is mainly determined by seasonal variation caused by rainfall, drying conditions, and soil suction. Changes in water content highly impact a subgrade covered by ballast and sub-ballast. The ballast and sub-ballast allow water to penetrate; nonetheless, they also impede its evaporation. As a result, a subgrade that is not free draining can get saturated and present strength-related issues (Li and Selig, 1995).

The behaviour of unsaturated materials is more complex as a negative pore-pressure is encountered. With an increase in moisture, there is a decrease in the matric suction, and the bearing capacity of the soil decreases drastically. An increase in moisture content can also result in larger resilient and plastic strains, as well as accelerate the rate of distresses in the substructure (Sahlour, 2015; Fredlund et al. 2012)

According to Hosseini et al. (2017), traffic loading decreases matric suction and net mean stress to magnitudes that do not trigger shearing failure; however, a reduction in strength and deformation modulus is pronounced.

When high moisture content is present at a fine-grained subgrade, a phenomenon called progressive shear failure (or cess heave) develops. In contrast, the soil is gradually sheared and remolded due to repeated overstressing. The surface soil gradually squeezes to the sides of the track and upward, following the path of least resistance. This heave on the sides of the track traps water entering from the embankment (Figure 2.2). A solution commonly used is the addition of more ballast above the subgrade squeeze zone. Nonetheless, while this addition results in an

increase in ballast depth and a reduction in stress at the subgrade level, the depression in the subgrade surface will still trap water that can further soften the subgrade (Figure 2.3). This problem is more present in fine-grained soils, particularly those with high clay content, than in coarse-grained soils. (Li and Selig, 2015; Li et al. 2002)

One case of progressive shear failure in Edgewood, Maryland, was described by Li et al. (2002). The tracks at this location experienced differential settlement constantly, and ballast tamping and surfacing were necessary at least twice a year. Remediation methods had been applied but were not successful. The primary cause of the differential track settlement was the variation in subgrade soil strength caused by water trapped along the track. The progressive failure caused significant excess heave of the subgrade soils across the track, and deep ballast pockets were also observed. The problem was attributed to overstressing and poor track drainage due to the fouled ballast. The rainfall water could not quickly drain out of the track, causing the softening of the subgrade soils.

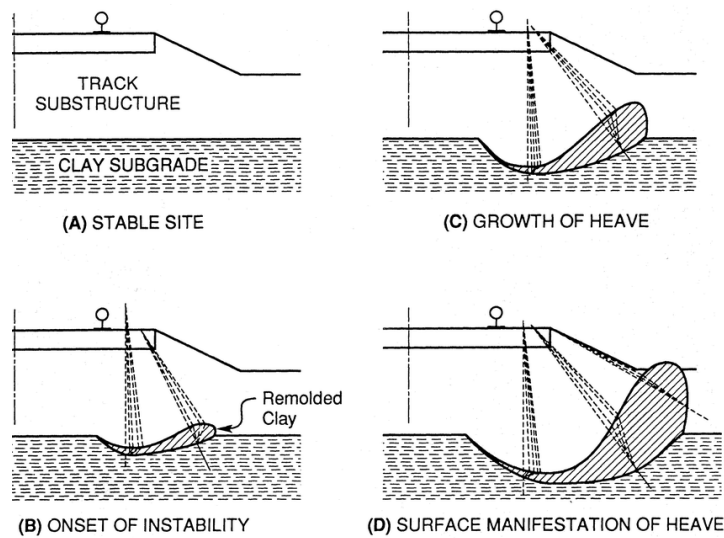


Figure 2.2. Progressive shear failure mechanism (Li et al. 1996)

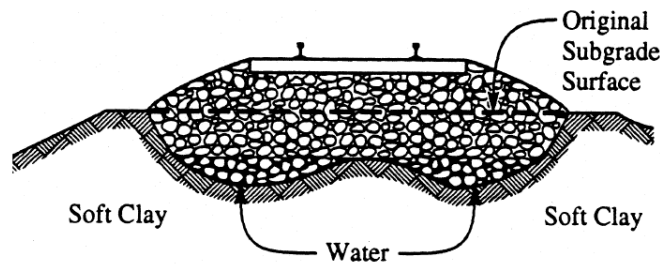


Figure 2.3. Formation of subgrade squeeze zones beneath track substructure filled with ballast (Li et al. 1996)

Another common subgrade failure due to repeated loading of fine-grained soil subgrades and high water content is the formation of ballast pockets. These pockets start to be formed with load-induced depressions under the track caused by either excessive plastic deformation or progressive shear failure of the embankment soil. Once they are formed, the soil can further soften due to the trapped water (Li and Selig, 1995).

One of the root causes for these failure types is an inadequate drainage system or poorly maintained railway track drainage. The best solutions to the problems mentioned above are to reconstruct the substructure with an adequate granular layer depth and suitable subgrade properties or include the use of geotextiles. Geotextiles have been frequently used in track substructure, especially in localised mud problem areas such as locations with the soft subgrade. (Indraratna et al. 2012; Selig and Waters, 1994).

2.2.3 Frost Heave

Frost heave is a common issue in Canada and can result in track geometry that may be hazardous to passing trains if present locally. Frost-heave mechanics can be identified as a problem of impeded drainage in a layered medium to an ice-water interface present in the frozen soil at the segregation-freezing front. The occurrence of frost heave requires frost-susceptible soil, a water supply, and subfreezing temperatures (Roustaei et al. 2019; Konrad, 1999).

Frost heave occurs from both the expansion of freezing water and the growth of ice lenses. Ice lenses begin to form as the ground freezes from the top downward and water flow upward due to capillary action. Even though much of the pore water is frozen, water transport still occurs in the frozen soil in response to temperature-induced unfrozen water content gradients and suction gradients in the water films. Capillary water continues to feed the ice lens growth until the ground freezes below the ice lens. Frost damage depends on the water availability within the track, causing drainage to be of utmost importance to potentially minimise the risk of frost damage. (Roustaei et al. 2019; Li et al. 2002; Indraratna et al. 2012)

a)

b)

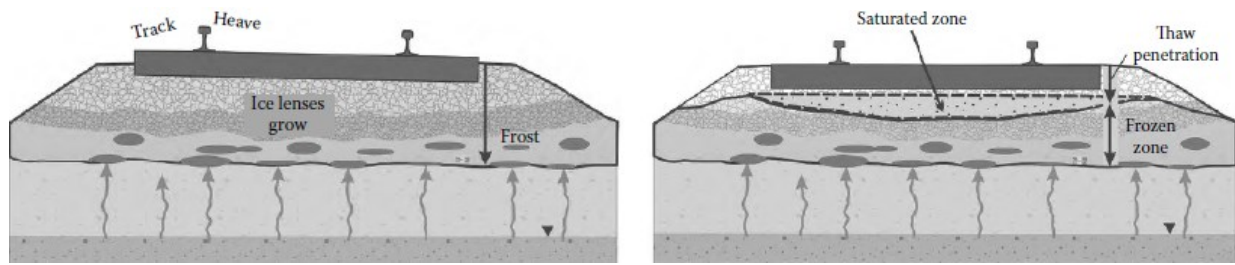


Figure 2.4. Illustration of the development of a) frost heave and b) thawing of the track (Li et al. 2002).

Damage due to frost action is caused by either the presence of segregated ice lenses in soils and consequent soil expansion as they are formed or strength weakening following melting (Konrad, 1999). The rise in temperature during Spring causes the melting of subsurface ice layers causing thaw softening. Thaw softening is associated with increase in pore pressures and internal seepage, causing a reduction in the effective bearing capacity and the stiffness of the subgrade (Indraratna et al. 2012).

Indraratna et al. (2012) mention that frost also contributes to ballast breakage, leading to an increase in the fine content and adding to the fouling of ballast. Hendry et al. (2016) performed one-dimensional frost heave testing on fines generated due to aggregate abrasion of ballast. It was found out that ballast fines are highly susceptible to frost heave.

The study by Jong et al. (1998) exemplifies how thaw softening affects the stiffness of a pavement substructure. The authors observed that when the subsurface was frozen, the modulus typically increased by 12x for the base course and 4x for the subgrade compared to the pre-freezing values. When thawing was complete, the base and subgrade modulus typically were about 35 percent and 65 percent of their pre-freezing values, respectively. The soils only recovered to their original modulus about 4 months after the end of thaw.

2.2.4 Clay Pumping

Higher moisture contents within the track embankment may contribute to the occurrence of formation of slurry and clay pumping under cyclic loading, tie degradation by water jetting, and ballast attrition by jetting action. When the railway embankment does not include a sub-ballast layer or presents a poorly designed sub-ballast, saturated subgrade clay and silt-size particles can become slurried and pump upwards under high cyclic loading. This phenomenon is known as

clay/mud pumping. In low-lying coastal areas where soft soil foundations are present, ballast fouling by clay pumping is commonly observed during and after heavy rainfall. The use of geosynthetics within the track substructure may minimise ballast fouling (Indraratna et al. 2011).

In saturated tracks, poor drainage may lead to excess pore water pressure build-up under train loading. If the permeability of the substructure elements becomes excessively low, the excess pore water pressure developed under an axle loading may not dissipate entirely before the next load is imposed. As the excess pore pressure did not dissipate, residual pore pressures accumulate with increasing load cycles. After a few load cycles, the total excess pore water pressure becomes very high and often causes clay pumping (Li et al. 2002).

This type of distress is a combined result of repetitive dynamic load applications, free water, and the presence of fines at the subgrade surface. In the presence of water, the products of attrition and water combine to form mud. This process causes track settlement and a decrease in the ballast and sub-ballast drainage capacity, which decreases the shear resistance and the resilience performance of these layers. In this case, subgrade strength is not a basis for determining whether this problem may occur. The mud pumping issue can be reduced by providing adequate drainage to ensure that water does not accumulate in the embankment and subgrade surface (Li and Selig, 1995).

2.3 Unsaturated Soil Mechanics in Railroads

Numerous soil materials found in engineering practice do not follow the behaviour found in saturated soil mechanics. Unsaturated soils have both water and air in the voids, and the pore-water pressure is negative relative to the pore-air pressure. Any soil with a water table below the ground surface will be subjected to negative pore-water pressures and a gradual reduction in the degree of saturation (Fredlund et al. 2012).

Considering that the soils present at railways usually are in unsaturated conditions, it is vital to understand the behavior of unsaturated soils and their application in engineering practice. This section focuses on the theory associated with the soil strength of an unsaturated material along with its implications in railway embankments.

2.3.1 Shear Strength of Unsaturated Soils

The Mohr-Coulomb failure envelope for a saturated soil is found by determining the tangent of at least three Mohr circles representing the stress state at failure. Two independent stress state

variables are required to define the stress state and consequently the shear strength of a saturated soil: shear stress and effective normal stress (Fredlund et al. 2012). The Mohr-Coulomb failure envelope (Figure 2.5(a)) assumes the form:

$$\tau_{ff} = c' + (\sigma_f - u_w)_f \tan \phi' \quad (2.1)$$

Where τ_{ff} is shear stress at failure; c' is effective cohesion; $(\sigma_f - u_w)_f$ is the effective normal stress at failure; σ_{ff} is the total normal stress at failure; u_{wf} is pore-water pressure at failure, and ϕ' is the effective angle of internal friction.

In contrast, the stress circle corresponding to the failure conditions of an unsaturated soil must be plot on a three-dimensional diagram (Figure 2.5(b)), where the ordinate is the shear strength and the axes in the horizontal plane are the soil suction and net normal stress. Therefore, when the soil suction is equal to zero, the graph would correspond to the case where the soil is saturated (Fredlund et al. 1978).

In order to allow the use of this concept to unsaturated soils, Ho and Fredlund (1982) defined that the increase in the shear strength caused by the matric suction can be expressed as an increase in cohesion. In this case, the soil at an unsaturated state can be visualized as having cohesion consisting of two components: the effective cohesion and the cohesion associated with matric suction (Equation 2.2) (Fredlund et al. 2012).

$$c = c' + (u_a - u_w) \tan \phi^b \quad (2.2)$$

where c is the total apparent soil cohesion. If the matric suction is zero, the apparent cohesion is the same as the effective cohesion. The extended Mohr-Coulomb failure envelope can be presented as a horizontal projection onto the shear strength τ versus $\sigma - u_a$ and consider the increase in strength using Equation 2.3 (Fredlund et al. 1978):

$$\tau' = c' + (\sigma_n - u_a) \tan \phi' + (u_a - u_w) \tan \phi^b \quad (2.3)$$

Where c' is cohesion intercept when the two stress variables are zero; $(\sigma - u_a)$ is the net normal stress; $(u_a - u_w)$ is the matric suction, ϕ' is the friction angle concerning changes in $(\sigma - u_a)$ when

$(u_a - u_w)$ is held constant; and ϕ^b = friction angle concerning changes in $(u_a - u_w)$ when $(\sigma - u_a)$ is held constant.

Fredlund et al. (2012) state that the shear strength vs. matric suction relationship can be nonlinear and matric suction increases from an initially saturated condition (Figure 2.6). At the first steps, low matric suctions occur while the soil specimen remains saturated. The friction angle ϕ' characterizes the effect of pore-water pressure and total normal stresses on the shear strength. The shear stress vs. matric suction envelope has a slope angle ϕ^b equal to ϕ' . This condition is maintained until the matric suction in the soil is increased, and desaturation occurs. A further increase in matric suction does not increase the shear strength as an increase in net normal stress would, leading to a reduction of ϕ^b when matric suction is increased beyond the AEV of the soil. Conventional triaxial and direct shear equipment require modifications that consider factors related to the nature of unsaturated soils before attempting to test such material. The procedure in these cases is costly and takes a long time to be performed (Fredlund et al. 2012). For this reason, prediction models of shear strength have been widely studied and the shear strength results.

The basic information required for formulating a shear strength function is the saturated shear strength parameters, which can be obtained by triaxial or direct shear tests and the SWCC (Fredlund et al. 2012). Vanapalli et al. (1996) suggested a non-linear model defined by Equation 2.4:

$$\tau = c' + (\sigma_n - u_a)\tan\phi' + (u_a - u_w)[(\Theta^\kappa)(\tan\phi')] \quad (2.4)$$

Where Θ_d is the normalized water content, and κ is a fitting parameter dependent on the soil type. In order to eliminate the need for a fitting parameter, Vanapalli et al. (1996) proposed another shear strength by including the normalization of the SWCC. The resulting equation is:

$$\tau = c' + (\sigma_n - u_a)\tan\phi' + (u_a - u_w) \left[\left(\frac{\theta - \theta_r}{\theta_s - \theta_r} \right) (\tan\phi') \right] \quad (2.5)$$

Where θ is the VWC of the soil, and θ_s and θ_r are the saturated and residual VWC values found in the SWCC curve, respectively. Generally, residual values are within 0-1500 KPa, except for highly plastic and some intermediate clays. The shear strength drops to zero at the residual suction value. Nonetheless, both equations returned a good prediction compared to experimental values between 0-500 kPa, which is the range that engineers are usually concerned with (Vanapalli et al. 1996).

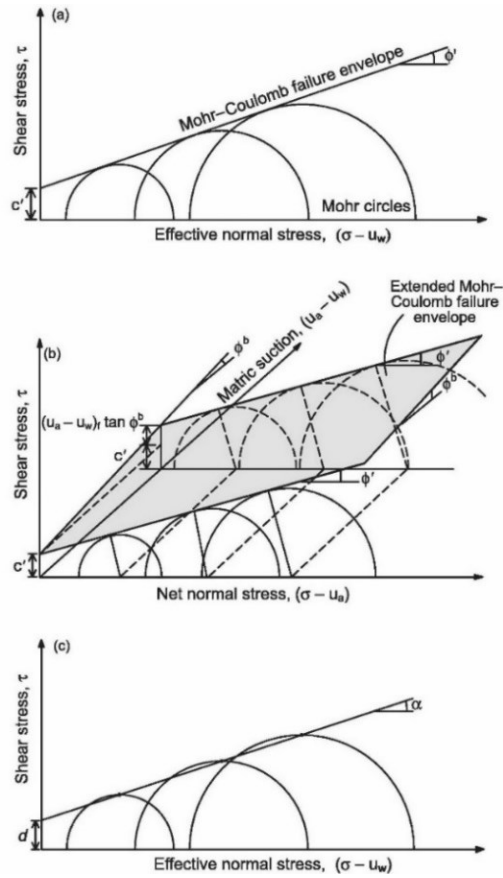


Figure 2.5. Failure envelopes for a) Saturated soils, b) Unsaturated soils, and c) Stress point envelope (Gui & Yu, 2008).

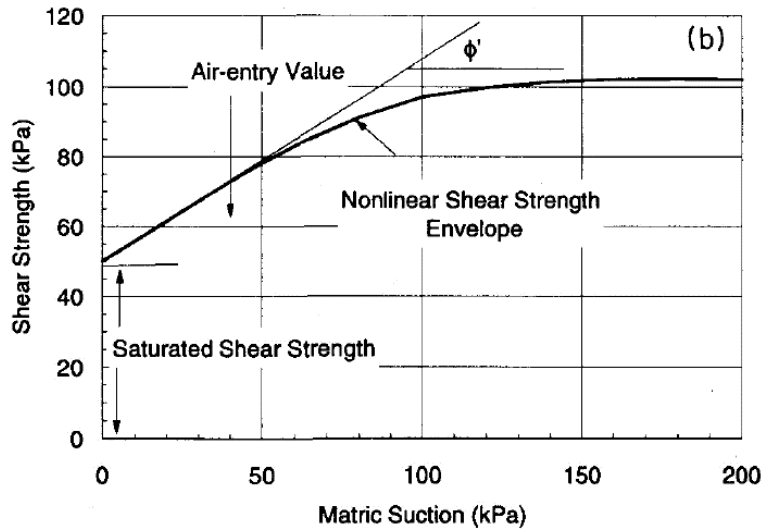


Figure 2.6. Non-linearity of Shear Strength Envelope (Vanapalli et al. 1996).

2.3.2 Soil Water Characteristic Curve and Testing Methods

The soil water content and soil suction relationship is defined by the Soil-Water Characteristic Curve (SWCC), which has an essential role in unsaturated soil mechanics. The SWCC is widely used to estimate the unsaturated soil property functions related to permeability and strength parameters. This curve is divided into three zones: boundary effect, transition, and residual (Fredlund et al., 2012).

The points delineating these zones are the air-entry value (AEV) and the residual value, which are of the utmost importance for the definition of the SWCC. The air-entry value defines the matric suction at which air starts to enter the largest opening between particles within the soil mass, being strongly dependent on the grain size distribution. The residual value represents the water content at which the applied suction must be considerably high in order to be able to remove more water from the soil (Fredlund and Xing, 1994).

The zone within the AEV and residual points shows a non-linear relationship between the water content and suction values. This section of the curve is called the transition zone and is greatly influenced by the particle size distribution. Sandy soils show a steep transition zone, typically within 1 kPa- 10kPa, while soils with finer particles display wider and smoother transition zones, with the residual values reaching considerably high values.

The examples shown in Figure 2.7 reveal that the saturated water content and the AEV generally increase as the particle size decreases. Other factors such as stress history and secondary soil structure also affect the shape of the SWCCs (Fredlund et al. 2012).

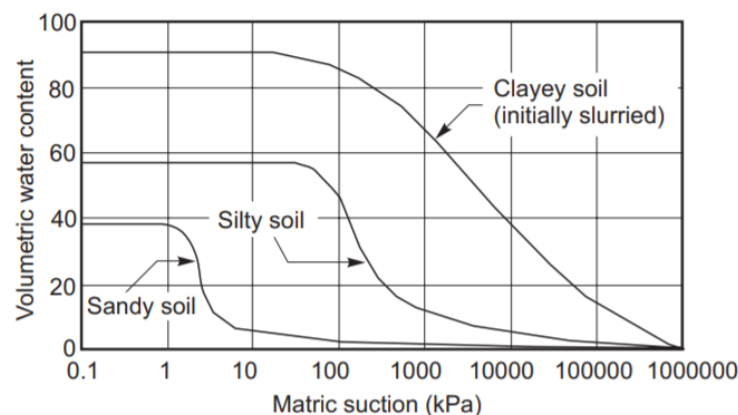


Figure 2.7. Comparison of SWCCs for different soil types (Fredlund and Xing, 1994).

Many mathematical relationships have been proposed to best-fit laboratory data for SWCCs using least-squares regression analysis (Fredlund and Xing, 1994). At high soil suction values beyond the residual, the results of empirical SWCC equations usually become asymptotic to a horizontal line as soil suction goes to infinity. However, Fredlund and Xing (1994) developed an equation that overcomes this problem (Fredlund et al., 2012). This SWCC equation has one variable related to the soil's air-entry value, a second variable that considers the soil desaturation rate, and a third variable associated with the residual water content.

The Fredlund and Xing (1994) equation is defined by Equation 2.6:

$$w(\psi) = C(\psi) \frac{w_s}{\ln \left[e + (\psi/a_f)^{n_f} \right]^{m_f}} \quad (2.6)$$

$$C(\psi) = 1 - \frac{\ln(1 + \psi/\psi_r)}{\ln[1 + (10^6/\psi_r)]} \quad (2.7)$$

$$\theta_d = \frac{w(\psi)}{w_s} \quad (2.8)$$

Where $w(\psi)$ is the water content at any soil suction, ψ ; $C(\psi)$ is the correction factor; e is an irrational constant used when taking the natural logarithm and is equal to 2.71828; a_f is a fitting parameter indicating the inflection point that bears a relationship to and is greater than the air-entry value; n_f is a fitting parameter related to the rate of desaturation; and m_f is a fitting parameter related to the curvature near residual conditions (Fredlund and Xing, 1994).

Several types of test equipment and test procedures have been used for measuring the SWCC. The early measurement of the SWCC involved a large pressure chamber, which can test a set of soil specimens concurrently. In these tests, matric suctions of up to 1500 kPa are applied to a soil specimen using a high-air-entry disk. Air pressure is applied to the specimen chamber using a pressure valve. Then, water drains against atmospheric pressure conditions, leading to matric suction being applied to the specimen (Fredlund et al. 2012).

At matric suctions less than about 5 kPa, air pressure valves may not be the best alternative to apply pressure to the specimens. The hanging column method can be used to apply small negative pressures to the water below the base of the high-air-entry disk. This negative pressure is applied by lowering the discharge tubing 10 mm to represent the application of 0.1 kPa of matric suction. The applied suction induces water discharge through a capillary needle placed in the tube; then, drained water is collected in a container until the specimen reaches equilibrium. After equilibrium, the discharge tubing is lowered incrementally, applying additional suction pressures as required (Fredlund et al. 2012; Abdalnabi, 2018).

In a Tempe Cell test, air pressure is supplied through the top plate while an outlet tube located at the base plate underneath the high-air-entry disk allows moisture removal from the specimen. A test is started by saturating the soil specimen and the high-air-entry disk. Water starts draining from the specimen through the high air-entry disk once the air pressure is applied. Changes in water content are measured by weighing the specimen and the cell until equilibrium is reached between the soil matric suction and the applied air pressure. Then, the air pressure is increased until enough points are collected for SWCC curve-fitting techniques (Fredlund et al. 2012).

Other types of SWCC tests worth mentioning include volumetric pressure plate extractor, column tests, chilled mirror hygrometer (for suction ranges of 500 kPa – 100MPa), centrifuge method and Hyprop system.

2.3.3 Past Studies on Unsaturated Soil Mechanics and Railway Embankments

Matric suction plays a major role in the performance of the railway structure. Its presence generally leads to a significant increase in bearing capacity and to an improved factor of safety of slopes due to the increase in shear strength. Strength values have been shown to decrease in the springtime due to snowmelt and wet periods of the year (Fredlund, 2006). Therefore, a good design of the drainage system is essential to avoid water accumulation within the embankment and consequent decrease in the soil shear strength.

Despite being designed to remain as drained as possible, the railway is often in a partially saturated state. In periods where excessive water is found, such as the spring thawing and heavy rainfall events, even railways with an excellent drainage design may undergo times where excessive moisture is found (Indraratna et al. 2011).

The cyclic loading of the railway is considered undrained due to its fast occurrence. Unfortunately, there are few studies related to the interpretation of the undrained shear strength of unsaturated soils. When dealing with unsaturated materials, volume change under undrained loading is mainly due to air compression. Soil specimens undergo changes in pore-air and pore-water pressures when subjected to increasing undrained loading, resulting in changes to the matric suction of the soil. Simultaneously, an increase in the confining pressure leads to a more significant increase in shear strength than the reduction seen due to decreased matric suction. (Vanapalli and Fredlund, 1999)

Sattler et al. (1990) developed a procedure that allowed incorporating soil suction into the bearing capacity design for railways. The procedure was used to analyze a railway embankment near Winnipeg, Manitoba, where the rail track was relocated in 1966/1967. Maintenance was required within a year of construction, and inclinometers presented movement recordings of around 22 mm/yr in the track during four years as a result of subgrade issues. As the previously existing conditions were analyzed, it was seen that with zero matric suction, the factor of safety of the track embankment was computed at 0.684 with the train load applied and 0.884 without the train load. When a matric suction of 55 kPa was included, the safety factor was computed at 0.926 with the train load and 1.205 without the train load. Therefore, the matric suction inclusion brings significant differences when estimating the bearing capacity (and factor of safety) of a track embankment.

Fredlund et al. (2010) presented the results of an investigation associated with a train derailment that occurred after an extended period of rainfall at a site in Alberta, Canada. The cause of the derailment was related to the net infiltration of water at the ground surface. The weather conditions leading up to the derailment were analysed, and a comparison to the climatic normal indicated above-average rainfall and snowfall in April. In the end, it was found out that prolonged and heavy precipitation was the critical condition leading to decreased matric suction, reduced shear strength, and consequent instability of the track structure. Differential rail settlement contributed to uneven the track as the subgrade further softened due to the trapped water, producing large deformation of the track system. The deformations resulted in a high impact factor under dynamic train loading, which contributed to the occurrence of the derailment.

2.4 Evaluation of the Relationship Between Soil Moisture and Precipitation

Many hydrological models have been developed to understand the moisture variations within soil materials aiming to define the relationship between soil moisture and precipitation events. These models usually incorporate remotely sensed soil moisture measurements and meteorological observations. One exception is the Antecedent Precipitation Index Model (API).

According to Xie and Yang (2013), the API can convey key soil water content characteristics caused by meteorological elements. This model considers the continuing impact of precipitation on soil moisture with time. The simplicity of this model and the required inputs make it a great alternative to relate rainfall events directly to moisture changes when a limited amount of information is available.

The concept of antecedent precipitation index (API) was first introduced by Kohler and Linsley (1951). Since then, many API applications have been widely studied to predict soil behaviour, such as the prediction of runoff, precipitation-runoff relationship, and the estimation of soil moisture content. API is used either as a supplement for limited moisture measurements or in addition to other inputs for the determination of the moisture content of large areas.

API is one of the most straightforward examples of hydrological models used to estimate soil moisture. Several studies have been made to link precipitation to soil moisture by using API because of the lack of field data (Bulut et al. 2019). This model's development facilitates understanding the correlation between the precipitation data available from weather stations and the VWC measurements obtained from moisture sensors. API can be computed from daily precipitation at different weather stations using the following equation:

$$API_t = \sum_{t=0}^d P_t k^t \quad (2.9)$$

Where P_t is the precipitation on day t , k is the attenuation coefficient ($0 < k < 1$) and d refers to the final time in days. The choice of k requires computations; however, its estimation is probably not justified as experience has shown that the determination of k is not critical for the model. The attenuation could be assumed to vary as a function of evaporation, air temperature, dewpoint, or vapor pressure deficiency (Kohler and Linsley, 1951).

2.5 Previous Studies on Wicking Geotextile

Indraratna et al. (2012) state that when appropriately designed and installed, geotextiles are a cost-effective alternative when compared to more traditional techniques. Guo et al. (2017) mention that geotextiles that require soil saturation are commonly used in roadways for drainage purposes; however, a new type of geotextile known for its wicking properties, Mirafi® H2Ri, is capable of reducing water accumulation in the soil even in unsaturated conditions. The wicking fibers made of unique hydrophilic and hygroscopic yarns woven into the geotextile can provide great potential for maximizing water transport in an unsaturated environment. This section brings a summary of studies about the effects of the incorporation of a wicking geotextile into the drainage performance.

2.5.1 Wicking Geotextile Incorporation in Highways

Bradley et al. (2017) performed an in-situ study incorporating the wicking geotextile into a low-volume highway near Watson Lake, Yukon, to verify the wicking and draining properties of the geotextile. The study also aimed to analyze whether its inclusion would minimize edge cracking. The site setup consisted of installing Mirafi® H2Ri above the subgrade in two sites, denominated 4 and 6. The geosynthetic was rolled out on the subgrade, starting at the roadside slope. A 22-m-long drainpipe made from slit 5.1 cm (2") Acrylonitrile Butadiene Styrene (ABS) pipe was attached along the outside edge of the geosynthetic in some of the quadrants of the test sections. The construction methods used at both sites are described in Figure 2.8.

Decagon GS-1 moisture sensors were installed in both sites below and above the geosynthetic and control site. Epoxy 44007 NTC Thermistors were used to identify the thawing period during the spring and monitor temperature changes in the shoulder of the road compared to the centreline.

The results from site 4 are shown in Figure 2.9. Bradley et al. (2017) mentioned that moisture contents reached 7.8% on the road centreline at 0.3 m depth and 8.2% on the treated shoulder at 0.4m depth due to the snow melting. On the untreated shoulder, the moisture content at 0.4 m depth increased to 8.2% after thawing. Therefore, the moisture content after thawing was similar for the treated and untreated areas. Days later, a percentage of the moisture dissipated, and moisture contents were down to 6.8% at the road centreline and treated shoulder. In contrast, the moisture measurements for the untreated area remained at a high level throughout the spring period.

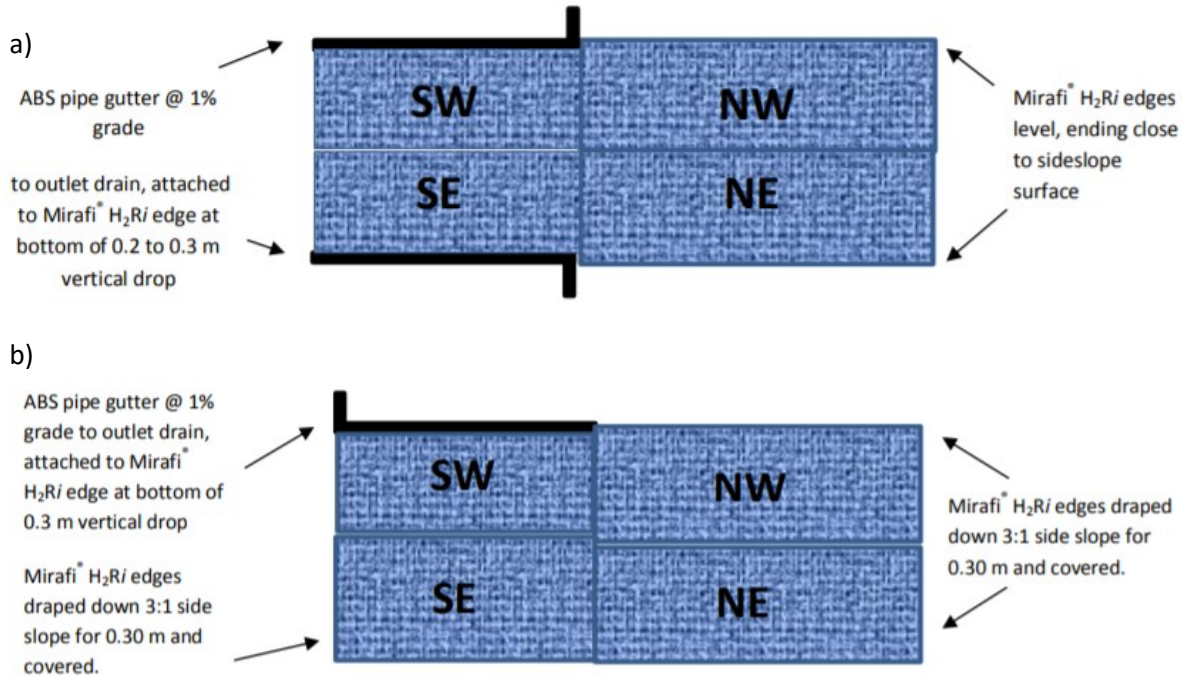


Figure 2.8. Edge treatments by quadrant for Mirafi® H₂Ri geosynthetic at a) test site 4 and b) test site 6 (Bradley et al. 2017).

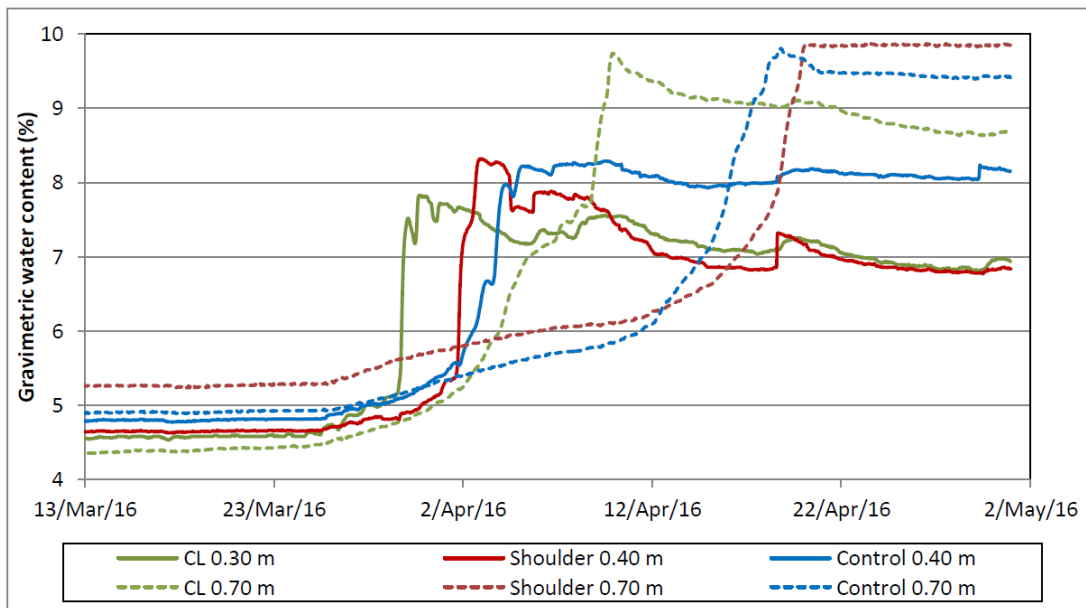


Figure 2.9. Moisture data for site 4. (Bradley et al. 2017).

This behaviour indicates that Mirafi® H₂Ri increases the drainage of excess water accumulated at the thawing front during spring top-down thawing. Moreover, the treated shoulder drained water more quickly after rapid increases in moisture. The geosynthetic also appears to drain water from the underlying roadbed materials.

Although more severe edge cracking was found in nearby untreated road sections, the study was inconclusive whether Mirafi® H2Ri could eliminate or reduce edge cracking since it may take as long as five years for it to appear after road construction.

2.5.2 Capillary Barrier Dissipation by New Wicking Geotextile

Azevedo & Zornberg (2013) alleged that the drainage improvement brought by the wicking geotextile properties might reduce capillary barrier events. The research investigated the unsaturated properties of five different versions of wicking geotextiles to test this hypothesis (Table 2.1).

Table 2.1. List of geotextiles for the testing program. From (Azevedo & Zornberg, 2013).

Name	Geotextile Description
GT1	Non-woven PP (Mirafi 180 N)
GT2	Woven wicking (Mirafi H2Ri)
GT3	Non-woven 50/50 4DG wicking/PP Non-woven 50/50 4DG
GT4	wicking/Hydrophilic
GT5	Non-woven 100% 4DG wicking

The first part of the study consisted of the development of the water retention curves of the geotextiles. In the test, the geosynthetic was subjected to suction by a number of methods and the corresponding water content was measured. Azevedo & Zornberg (2013) reported that the nonwoven geotextiles behaved as expected, presenting a sharp decrease in water content over a very narrow suction range. The critical difference in the curves of GT1 and GT2 is the water entry suction on the wetting curve. GT1 has a lower water entry value than GT2 (Mirafi® H2Ri); thus, GT2 starts absorbing water faster than GT1. Therefore, GT2 could be a good alternative to minimize the moisture buildup from a capillary barrier; however, this hypothesis needed to be confirmed (Azevedo & Zornberg, 2013).

The second part of the research consisted of capillary soil column testing, which is recommended to simulate capillary barriers and understand capillary barrier performance (Pickles and Zornberg, 2012).

Azevedo & Zornberg (2013) mentioned that a base plate with holes drilled into it was installed underneath the gravel to allow water to drain. A tipping bucket connected to the bottom of the column indicated when the water penetrated the bottom layer. Three TDR were included in the clay layer to monitor the moisture migration throughout the column.

The test's goal was to see which geotextile performed the best in terms of lateral drainage and minimization of the capillary barrier. Azevedo & Zornberg (2013) discussed that despite all geotextiles were unable to avoid the occurrence of a capillary barrier, the lateral drainage function provided by the wicking fibers was able to dissipate the capillary barrier after it formed. The moisture dissipation was associated with the wicking fiber's lateral drainage capabilities, showing that it fulfilled its purpose to improve lateral drainage.

2.5.3 Wicking Geotextile Drainage Capabilities in Roadway Systems

A 6 mile (10 km) stretch of Texas State Highway 21 founded on an expansive clay subgrade was rehabilitated by the Texas Department of Transportation in 2013. The rehabilitation plan involved milling the top 3 in. (762 mm) of the pavement, followed by partial excavation of the outside line and additional expansion of the shoulder. Before rehabilitation, the road required continued maintenance operations.

The University of Texas at Austin constructed eight 500 ft. (152 m) long test sections aiming to evaluate the impact of different geotextiles on the performance of pavements founded over expansive clays. Four geotextiles were evaluated: a standard non-woven geotextile used for separation; two types of woven geotextiles used for base stabilization and separation; and a wicking geotextile (Mirafi® H2Ri) used for lateral drainage, base stabilization and separation. Moisture sensors were installed along the road shoulder at the center of each test section, as shown in Figure 2.10. This setup allowed the monitoring of changes in moisture content in the subgrade along the road shoulder.

Zornberg et al. (2017) concluded that the moisture content at the section remediated with the wicking geotextile remained relatively uniform over time and across the entire width of the road shoulder. Even though there were points with less moisture at other sections (Figure 2.11), the wicking geotextile section showed a more uniform distribution. The authors stated that the moisture content values across the width of the shoulder indicated that the wicking geotextile was capable of controlling the development of differential settlements. The tests also demonstrated that the enhanced lateral drainage effectively homogenized the moisture content distribution across the pavement section in an expansive clay subgrade.

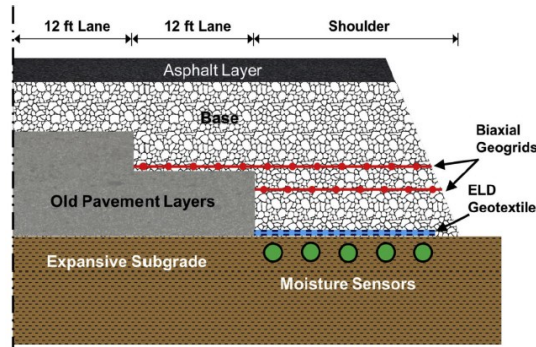


Figure 2.10. Position of moisture sensors at SH 21 (Zornberg et al. 2017).

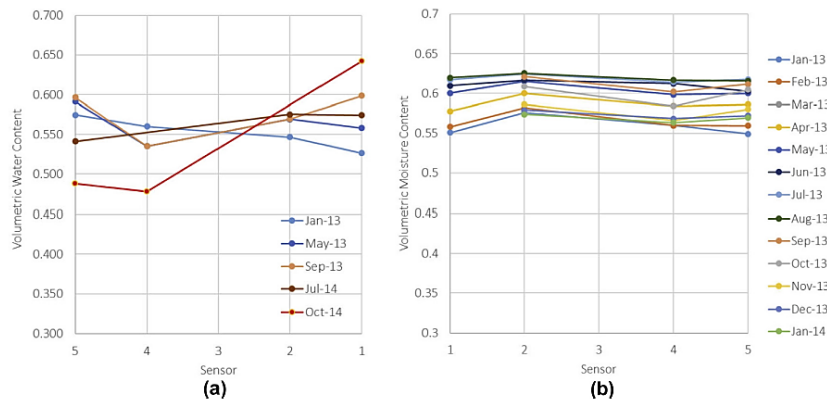


Figure 2.11. Moisture content distribution along the shoulder of SH 21: (a) In the section with conventional geotextile, (b) In the section with wicking geotextile (Zornberg et al. 2017).

2.5.4 Laboratory Tests to Evaluate the Effectiveness of Wicking Geotextile

Wang et al. (2017) developed a physical model test that evaluated the effectiveness of the wicking geotextile for roadway applications. A test box with 1041 mm in length, 686 mm in width, and 584 mm in height was used with two HDPE plastic panels separating the box into two sections. One section contained a dehumidifier, responsible for collecting the water wicking out of the geosynthetic that evaporated. The other section of the box was backfilled with subgrade soil at optimum moisture content before placing the geotextile above it. Aggregate Base Class 3 (AB3) was adopted for the base course laid out above the geotextile, while the subgrade was composed of Kansas River sand and kaolinite with a ratio of 3:1.

The test was carried out according to the following steps: after the construction of the road section, the dehumidifier was used to collect the water wicked from the soil by the geotextile; then, water was sprayed on the surface of the road section to simulate rainfall. At this point, the dehumidifier was removed while the water removed from the soil by the wicking geotextile was collected. The dehumidifier was then set up again inside the box and kept running until a minimum amount of

water came out from the soil. The road section was exhumed after the test, and the moisture contents of the materials were measured. These contents were compared to the initial values and the values calculated under saturated conditions to demonstrate the effectiveness of the wicking geotextile (Wang et al. 2017).

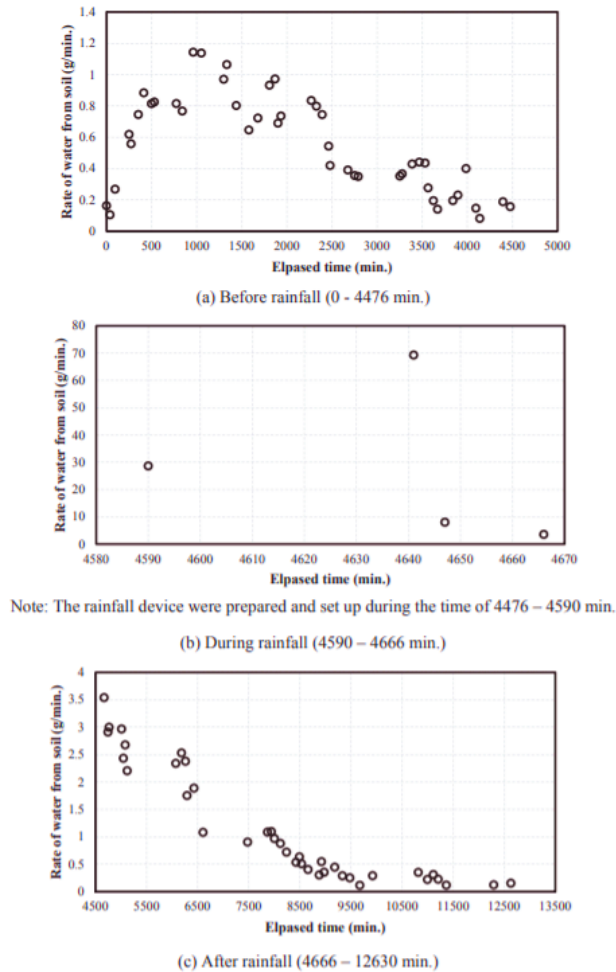


Figure 2.12. Water removal rate at different test stages (Wang et al. 2017).

Wang et al. (2017) compared the rate of water for each phase of the test in order to verify the wicking geotextile effectiveness. Figure 2.12(a) shows water removal rates right after the section construction and before rainfall. The starting water removal rate was low, but it increased after 1000 minutes, indicating that the wicking geotextile may need some time to suck water from the surroundings and transport it out of the soil. It also demonstrates that the wicking geotextile could drain water even when the soil was prepared at the moisture content close to the optimum. Figure 2.12(b) presents the water removal rate during rainfall and for 36 min after inundation. This testing stage was stopped when no additional free water came out. Figure 2.12(c) shows the rate of water

removal from the soil after rainfall. Since the dehumidifier calibration was not changed, the water removed from the air may be overestimated, and the water removed from the soil may be underestimated.

According to Wang et al. (2017), the test results lead to the following conclusions: the base course kept the same initial moisture after the rainfall due to the action of the wicking geotextile, and this is proven by the lower moisture content of the base where it is closer to the geosynthetic. It was also concluded that the geotextile drains the moisture until a limited distance from its installation.

2.5.5 Performance of Wicking Geotextile on Mitigating Water Pumping Issue

This study was performed by Zhang and Galinmoghadam (2020) at pavements in Missouri to compare the effectiveness of different placements of the geotextile Mirafi® H2Ri within a highway in promoting moisture release and pumping mitigation. The test site included three sections, one control section without changes, a section with an L-shaped wicking geotextile, and a third section with the wicking geotextile installed horizontally. All test sections were instrumented with moisture sensors and monitored for one year.

The relative VWC in the section with L-shaped wicking geotextile was occasionally higher than the VWC in the control section. It was identified that the end of the geotextile was buried. After exposing the geotextile edge, the section started to perform better in terms of draining moisture out of the pavement.

Rainfall infiltration was identified as the major reason for moisture content increase. Water back flowed into the pavement from the exposed end of the wicking geotextile for a short period during rainfall. Then, the wicking geotextile drained the water out of the soil right after rainfall stopped.

The results demonstrated that the wicking geotextile acted to significantly reduce the moisture content in the pavement structure and was beneficial to the mitigation of the pumping issue. When comparing the construction methods applied, the wicking geotextile horizontal installation performed better than the L-shaped installation. The authors also concluded that exposing one end of the wicking geotextile to the atmosphere may significantly improve the drainage performance of the pavement.

2.5.6 Evaluation of H2Ri wicking fabric for pavement application

Zhang and Connor (2015) performed a series of laboratory tests to determine whether the Mirafi® H2Ri may be ineffective in different soil types and if it continues to work when length requirements exceed the fabric width. Three test flumes were constructed on a level grade. One of them was filled with sand, another flume was filled with organic silt (which was expected to represent how the geotextile behaves in low permeability materials), and a third flume was filled with Brown's Hill E-1.

Three layers of sensors were located at three different depths, and the wicking fabric was located at 1 in. from the bottom of the testing flume. The left side of the fabric was exposed to the open air. A 3 ft. long overlap of the wicking fabric started at 5 ft. from the left side of the testing flume. The fabric was immediately blinded and ceased to perform in the flume containing the organic silt. The exposed fabric at the outlet remained dry throughout the test. Photomicrographs showed the wicking fibers were coated with the organic clay contained in the silt.

Based on the tests, the geotextile is expected to work well in free-draining soil such as sands, sandy gravels and silts but should not be used in organic silts. No firm conclusions about soils containing clay were drawn since organic clays behave differently from other clays.

The authors implied that Mirafi® H2Ri might not be effective in impermeable soils since water cannot readily get to the fabric. Another essential factor that might influence drainage efficiency is clogging. Soils with a particle size smaller than 5–12 μm may cause a clogging issue in the deep grooves of the wicking yarns. The study also showed that using the simple overlap of the H2Ri as a splice, while effective, was not as efficient at moving water as the fabric itself. Consequently, moisture tended to build up around the splice.

3. DESCRIPTION OF INSTRUMENTATION AND RECONSTRUCTION OF STUDY SITE

The research site is located at CP’s Scotford subdivision near Fort Saskatchewan, AB. Previously, the track has presented settlement and clay pumping issues attributed to poor drainage and retention of moisture within both the embankment and subgrade. The embankment materials of a track section were replaced while a 4.6 m wide reinforcing geotextile (Mirafi® RS580i) and a 7.3 m wide wicking geotextile (Mirafi® H2Ri) were installed in the ballast and sub-ballast interface and between the subgrade and sub-ballast, respectively, as part of CP’s track renewal plan (Alvarenga et al. 2020). This section is named “remediated section” in the entire document.

3.1 Instrumentation and Calibration

3.1.1 5TE Moisture Sensors

During and after the reconstruction, 5TE moisture sensors (Figure 3.1) were also placed at the site for the investigation. These sensors can measure bulk electrical conductivity, volumetric water content, and soil temperature using an oscillator running at 70 MHz to measure the soil dielectric permittivity. The details on the sensor physical specifications are presented in Table 3.1.

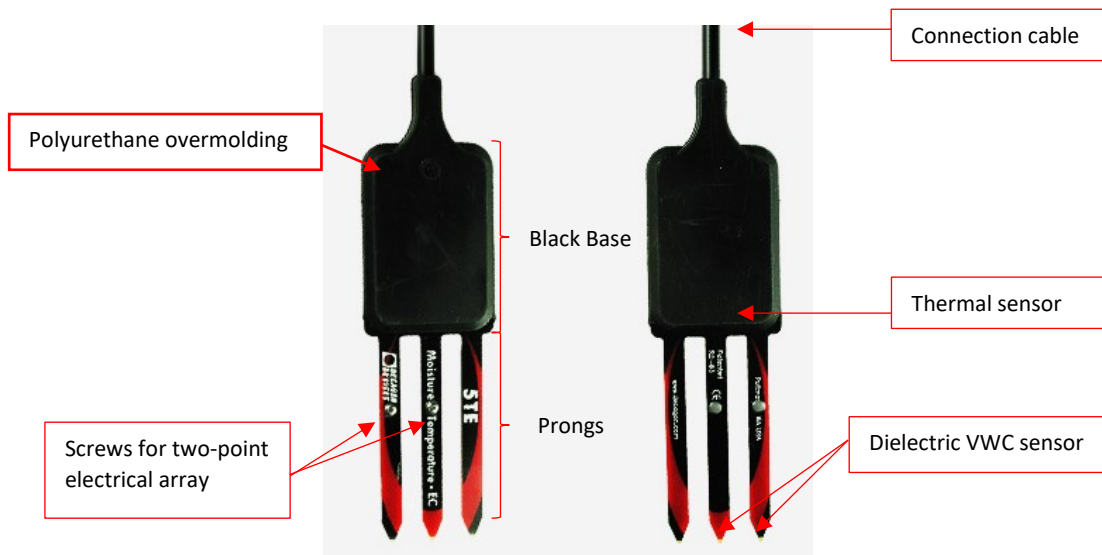


Figure 3.1. 5TE Moisture Sensors (Hoskin Scientific Ltd, n.d.).

The installation followed the directions for vertical placement, with a 10 cm (4 inch) hole being drilled down to the depth required and protected by a PVC pipe. The sensor was pushed into the soil at the bottom of the hole using a notched pipe. All the access pipes were backfilled with a clean sub-ballast material afterward.

The raw dielectric value (ϵ_{Raw}) read by the sensor is converted to dielectric permittivity (ϵ_a) by using Equation 3.1.

$$\epsilon_a = \frac{\epsilon_{Raw}}{50} \quad (3.1)$$

The results of this equation range from 1 to 80 and these extremes correspond to the dielectric permittivity of air and water, respectively.

Table 3.1. Physical Specifications of 5TE Sensors (Meter Environment, 2019).

Dimensions	
Length	10.9 cm (4.3 in)
Width	3.4 cm (1.3 in)
Height	1.0 cm (0.4 in)
Prong Length	
5.0 cm (1.9 in)	
Operating Temperature Range	
Minimum	-40° C
Typical	NA
Maximum	+60° C
Cable Length	
5 m (standard)	
75 m (maximum cable length)	
Connector Types	
3.5-mm stereo plug connector or stripped and tinned wires	

The volumetric water content is converted using the calibration provided by the Topp equation (Meter Environment, 2019).

$$VWC = 4.3 \times 10^{-6} \epsilon_a^3 - 5.5 \times 10^{-4} \epsilon_a^2 + 2.92 \times 10^{-2} \epsilon_a - 5.3 \times 10^{-2} \quad (3.2)$$

The use of this equation results in measurements within $\pm 3\%$ of the actual soil VWC. However, the general calibration may not be applicable for all soil types. Therefore, soil-specific calibrations are necessary to improve the sensor's accuracy to 1%-2%, as shown in Table 3.2.

In order to perform the soil-specific sensor calibration (Method A), it is first necessary to determine the gravimetric moisture content of the sample by using Equation 3.3.

$$w = \frac{m_{soil,air\ dry} - m_{soil,oven\ dry}}{m_{soil,oven\ dry}} \quad (3.3)$$

Table 3.2- Measurement Specifications of 5TE Sensors (Meter Environment, 2019).

Volumetric Water Content (VWC)	
Range	
Mineral Soil Calibration	0.0-1.0 m ³ /m ³
Soil less media calibration	0.0-1.0 m ³ /m ³
Apparent dielectric permittivity (ϵ_a)	1 (air) to 80 (water)
Resolution	0.0008 m ³ /m ³ from 0%-50% VWC
Accuracy	
Generic Calibration	± 0.03 m ³ /m ³ typical
Medium-specific calibration	± 0.02 m ³ /m ³
Apparent dielectric permittivity (ϵ_a)	1-40 (soil range), $\pm 1\epsilon_a$ (unitless) 40-80, 15% measurement
Temperature	
Range	
Resolution	-40° to +60° C
Accuracy	0.1° C
Accuracy	
$\pm 1^\circ$ C	
Bulk Electrical Conductivity (EC)	
Range	
Resolution	0-23 dS/m (bulk)
Accuracy	0.01 dS/m from 0-7dS/m 0.05 dS/m from 7-23 dS/m
Accuracy	
$\pm 10\%$ from 0-7 dS/m User calibration required from 7-23 dS/m	

The volume of water is found by converting the mass of water using the following equations:

$$m_{moist\ soil} = m_{total} - m_{soil,oven\ dry} \quad (3.4)$$

$$m_w = m_{moist\ soil} - m_{soil,oven\ dry} \quad (3.5)$$

$$V_w = m_w / \rho_w \quad (3.6)$$

Where m_w is the mass of water, $m_{moist\ soil}$ is the mass of moist soil (g), $m_{soil, oven-dry}$ is the mass of the oven-dry soil, and ρ_w is the density of water (1 g/cm³). Using the found V_w , it is possible to estimate the volumetric water content according to Equation 3.7:

$$\theta = V_w/V_t \quad (3.7)$$

Where θ is volumetric water content (cm^3/cm^3), V_w is the volume of water (cm^3), and V_t is the total volume of the sample container (cm^3) (Meter Environment, 2019). The soil bulk density can be calculated according to Equation 3.8:

$$\rho_b = m_{dry}/V_{soil} \quad (3.8)$$

The determination of the bulk density of the soil is vital to determine whether the laboratory calibration can be applied to the field. If the packed soil has a difference in its bulk density of more than 20% of the field bulk density, the calibration should be repeated to apply to the field.

In order to find a calibration equation, a regression function (that can be either linear or quadratic) should be used to construct a mathematical model of the relationship (Meter Environment, 2019).

3.1.2 Diviner 2000

Diviner 2000 comprises a data display unit and a portable probe, as shown in Figure 3.2. It measures the volumetric water content along the soil profile using frequency domain reflectometry (FDR) at regular intervals of 10 cm (4 inches). The readings are taken through the wall of 5 cm diameter PVC access pipes installed at the site. In order to generate absolute data, a gravimetric sampling is necessary to calibrate the Diviner 2000 for the soil present at the site.

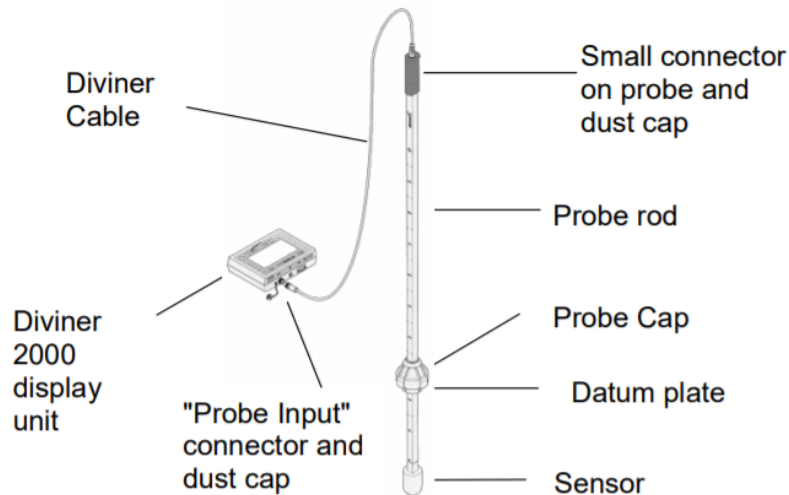


Figure 3.2. Diviner 2000 setup. (Sentek Pty Ltd, 1999).

The probe records data at 10 cm intervals of depth in the soil. Each reading is a snapshot of the soil moisture content at a determined depth. The readings can be collected in the field using the display unit. The data was then compared to the VWC readings collected at the same date by 5TE moisture sensors.

According to Sentek Pty Ltd (1999), the probe has a default calibration based on combined data gathered from sampling on sand, sandy loam, and organic potting soil; however, this calibration does not generate accurate data for all types of soils. In order to provide absolute VWC measurements for the studied soil profile, customized calibration equations should be obtained.

The calibration must be performed to define the mathematical function that describes the relationship between scaled frequency and VWC. The raw resonant frequency detected by the sensor in the soil is scaled to a value of SF ranging between 0 and 1 according to Equation 3.9:

$$SF = \frac{F_a - F_s}{F_a - F_w} \quad (3.9)$$

Where F_s , F_a , and F_w are the resonant frequencies detected by the sensor in the soil, air, and water, respectively. The values of scaled frequency for water and air are found at the Diviner display by pressing the button SETUP. The volumetric soil water content, θ ($\text{cm}^3 \cdot \text{cm}^{-3}$), can then be evaluated by curve-fitting the scaled frequency with the VWC estimated from the gravimetric sample:

$$SF = a\theta^b + c \quad (3.10)$$

Where a , b , and c are fitting parameters. The calibration equations should be estimated for each soil layer for better accuracy, as the probe can process data using a different calibration equation for each 10 cm depth increment.

3.1.3 Laboratory Calibration of Field Instruments

The two sensors used for moisture determination use different principles to determine the field volumetric water content. This difference has caused a difference in the results found by each. Therefore, it was essential to determine the relationship between these sensor readings to perform a better analysis. In order to provide a better direct comparison between the readings of both

sensors, the developed laboratory setup was designed to be suitable for the calibration of the 5TE moisture sensor and the Diviner moisture profiler at the same time. The requirements for both sensors were considered in this design.

The soil container was composed of a bucket with an internal diameter of 29 cm and a 7.2 cm PVC tube inserted in the center to allow readings with the Diviner 2000 probe (Figure 3.3). For the proper installation of the ECH₂O 5TE sensors, one hole was cut 10 cm from the bottom of the bucket. The placement of this hole ensured the sensor moisture measurements would coincide with the ones from the Diviner probe for a direct comparison.

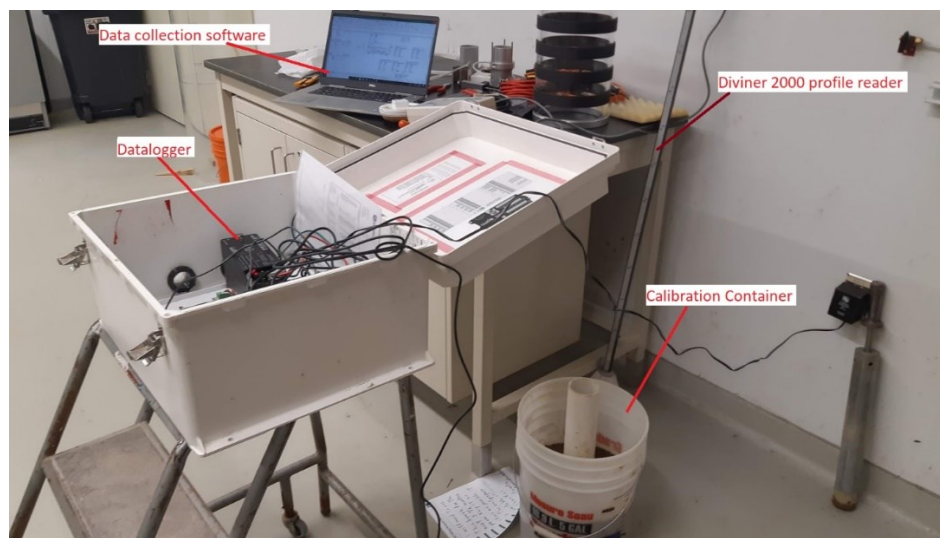


Figure 3.3. Calibration setup for 5TE and Diviner 2000 sensors.

For the calibration, it is recommended that the bulk density of the soil matches the field conditions. The method chosen to assure the bulk density necessary was to obtain soil from the sub-ballast and subgrade layers then let them air-dry, mixing thoroughly on a plastic sheet. Before placing soil into the setup, a PVC access pipe was put in an erect, central position inside the container. The known volumes of both the container and PVC tube were used to determine the weight of soil required to fill a height of 2 cm/0.79” in the specified density. Then, the soil was compacted until reaching the desired height. Before repeating the step of pouring soil over the compacted layer, the topsoil was scarified. This process was repeated until reaching a height of 16 cm of soil within the bucket.

The test was repeated for four to five water content levels: air-dried, maximum moisture seen at the field, and intermediate moisture contents. The dry bulk density and the volume of the container can then be used to determine the amount of water to be added to the soil by using Equation 3.11(3.11):

$$\theta = \frac{V_w}{V_t} \quad (3.11)$$

Where θ is the VWC (cm^3/cm^3), V_w is the volume of water (cm^3), and V_t is the total volume of the sample (cm^3), found using the area of the container multiplied by 2 cm (for each compacted layer). Since the water density is around $1 \text{ g}/\text{cm}^3$, V_w can be considered as the mass of water in grams to be mixed into the soil.

After the compaction, the 5TE sensor was inserted into the soil in the designated hole. Meter Environment (2019) recommends the insertion of the entire black base of the sensor into the sample and, if this is not possible, at least the prongs should be entirely covered. After its placement, the sensor was connected to a datalogger associated with a software to collect the calibration data (Figure 3.3).

In order to verify the moisture content of each calibration point, the soil was removed from the setup, and two samples were collected for each test using thin-walled metal rings. The gravimetric and volumetric moisture content of the materials could then be determined by oven-drying the samples and using the following equations:

$$w = \frac{m_{\text{wet soil}} - m_{\text{oven-dried soil}}}{m_{\text{oven-dried soil}}} \quad (3.12)$$

The dry bulk density can be verified using:

$$\rho_d = \frac{\rho}{(1 + w)} \quad (3.13)$$

And the determination of the dry bulk density enables the determination of the VWC.

$$\theta = w \times \rho_d \quad (3.14)$$

The 5TE sensor was only placed after the compaction to avoid damages to it. At least three readings from both 5TE sensors and Diviner 2000 were taken for each moisture level.

3.2 Description of Remediated Section Reconstruction and Instrumentation

3.2.1 Geotextiles

Figure 3.4 shows the two geotextiles that were installed at the remediated site. Used between the ballast and sub-ballast layers, Mirafi® RS580i is designed to be a solution for base course reinforcement, subgrade stabilization for road, runway, railway construction, and embankment stabilization on soft foundations. Mirafi® RS580i properties are described in Table 3.3.

The geotextile represented in green in Figure 3.8 is Mirafi® H2Ri, a woven geotextile that provides continuous moisture management of the materials and the functions of reinforcement, confinement, separation, and filtration. The wicking yarns sewed within this geotextile are believed to provide enhanced lateral drainage along the geosynthetic plane during its lifetime (Wang et al. 2017). This geotextile lifetime is defined by the other functions performed, ranging from 5 to 100 years depending on its primary function (Geosynthetic Institute, 2019; Tencate, n.d.). Mirafi® H2Ri properties are listed in Table 3.4.

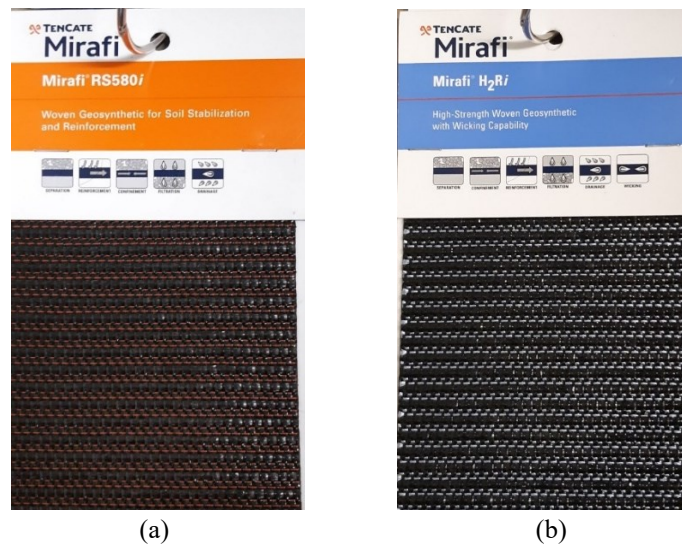


Figure 3.4. Geotextiles used in the soil reinforcement a) Mirafi® RS580i b) Mirafi® H2Ri.

Table 3.3. Characteristics of Mirafi® RS580i. From Tencate (2018).

Roadway Design and Performance Properties	Unit	Design/ Calibration Value	
		MD	CD
Base Course Improvement Factor	-	1.4	
Subgrade Improvement/Increase	lb/in ²	9000 (62.0)	
Cyclic Tensile Modulus: J _{cyclic}	kip/ft	60 (876)	160 (2336)
Resilient Interface Shear Stiffness: G _i	kip/in ²	329(2268)	
Traffic Benefit Ratio: TBR	-	9/13.1/39	
Interaction Coefficient C _i	-	0.9	
Pore Pressure Dissipation Ratio	-	2	
Typical Dynamic Filtration Pore Size 0 ₅₀ , 0 ₉₅	microns	337/192	
Maximum Percent Open Area: MPOA	Percent	7.3	
Tensile Strength at 5% strain	lb/ft (kN/m)	1440 (210)	4380 (63.9)
Tensile Strength at 2% strain	lb/ft (kN/m)	480 (7.0)	1880 (26.3)
Index Properties			
Apparent Opening Size, AOS	U.S.Sieve	40 (0.425)	
Permittivity	sec ⁻¹	1	
Flow Rate	gal/min/ft ² (l/min/m ²)	75(3056)	
UV Resistance	% strength retained	90	
MD: Machine Direction; CD: Cross Direction			

Table 3.4. Characteristics of Mirafi® H2Ri. From Tencate (2015).

Mechanical Properties	Unit	Minimum Average Roll Value	
		MD	CD
Wide Width Tensile Strength	lbs/ft (kN/m)	5280 (77.0)	5280 (77.0)
Wide Width Tensile Strength @ 2% Strain	lbs/ft (kN/m)	480 (7.0)	1080 (15.8)
Maximum Opening Size			
Apparent Opening Size	U.S. Sieve (mm)	40 (0.425)	
Minimum Roll Value			
Permittivity	sec-1	0.4	
Flow Rate	gal/min/ft ² (l/min/m ²)	30 (1222)	
Minimum Test Value			
Pore Size 0 ₅₀	microns	85	
Pore Size 0 ₉₅	microns	195	
Wet Front Movement 1 (24 minutes)	inches	6.0 Vertical	
Wet Front Movement 1 (983 minutes) Zero Gradient	inches	73.3 Horizontal	
STP: Standard Temperature and Pressure; MD: Machine Direction; CD: Cross Direction			

3.2.2 Field Instrumentation Design

The instrumentation design was finalized after multiple idea exchanges and discussions with CP and the contractor (Edmonton Railway Contracting Ltd.). The installation occurred while the track reconstruction was performed at the farther milepost since it was necessary to minimize the period

that traffic had to be stopped. Figure 3.5 shows the access pipes' placement plan view, while Figure 3.6 to 3.8 show the location of the access pipes within the embankment and their depth.

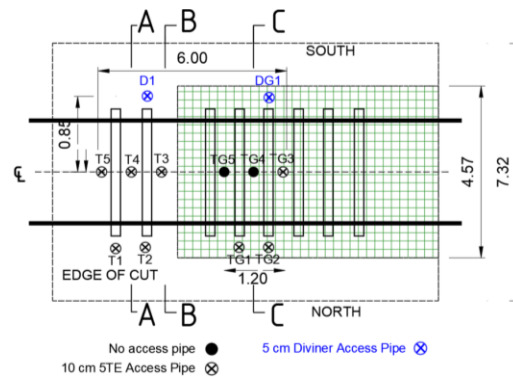


Figure 3.5. Plan view layout of the access pipe installation (dimensions in meters).

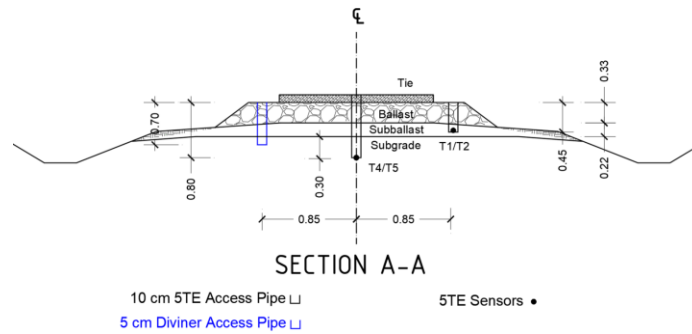


Figure 3.6. Cross-section of control site setup: access pipe at subgrade layer (dimensions in meters).

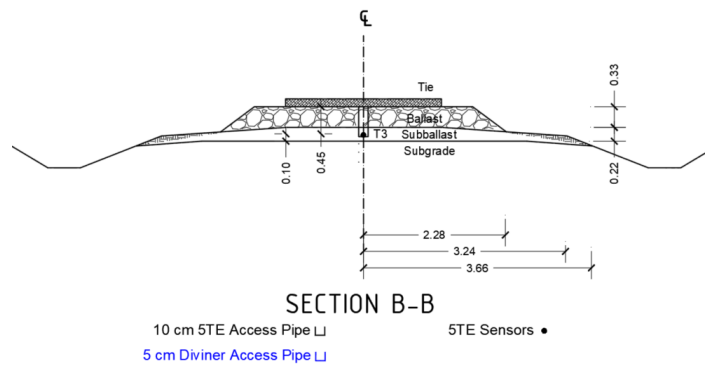


Figure 3.7. Cross-section of control section: access pipe at sub-ballast layer (dimensions in meters).

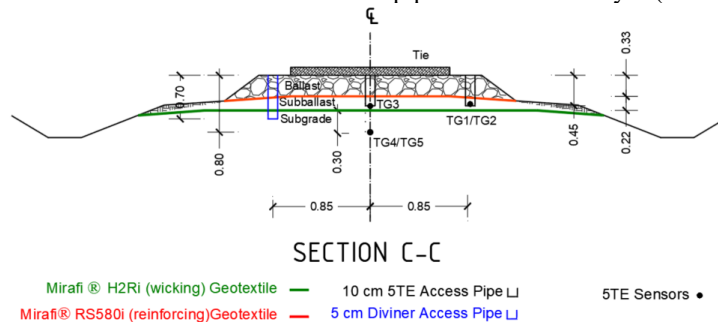


Figure 3.8. Cross-section of remediated section (dimensions in meters).

The instrumented track length is approximately 6 m consisting of a control (untreated) section and an adjacent remediated section in a single track (Figure 3.5). The black circles in Figure 3.5 and the black rectangles in Figures 3.6 to 3.8 represent the access pipes for the 5TE moisture sensors. Access pipes T1, T2, TG1, and TG2 were placed at the shoulder of the sub-ballast layer, and access pipes T3 and TG3 were installed in the centerline of the sub-ballast layer. Access pipes T4 and T5 were placed at the subgrade centreline of the control section. No access pipes were installed for sensors TG4 and TG5, represented by the solid black circles in Figure 3.5. Blue circles in Figure 3.5 and blue rectangles in Figures 3.6 to 3.8 depict the location of access pipes for Diviner 2000, a portable moisture profiler.

A total of 6 access pipes were installed in the control section, and 4 access pipes were placed in the remediated section. Information concerning the access pipes is summarized in Tables 3.5 and 3.6.

Table 3.5. Summary of access pipes at control section.

Sensor ID	Depth (m)	Diameter (cm)	Soil Layer	Position at Track	Section	Access Pipe Function
T1/T2	0.45	10	Sub-ballast	Shoulder	Control	Install 5TE Sensor
T3	0.45	10	Sub-ballast	Centreline	Control	Install 5TE Sensor
T4	0.65	10	Subgrade	Centreline	Control	Install 5TE Sensor
T5	0.80	10	Subgrade	Centreline	Control	Install 5TE Sensor
D1	0.60	5	Subgrade	Shoulder	Control	Read moisture profile using Diviner 2000

Table 3.6. Summary of access pipes at remediated section.

Sensor ID	Depth (m)	Diameter (cm)	Soil Layer	Position at Track	Section	Borehole Function
TG1/TG2	0.45	10	Sub-ballast	Shoulder	Remediated	Install 5TE Sensor
TG3	0.45	10	Sub-ballast	Centreline	Remediated	Install 5TE Sensor
TG4 ¹	0.91	10	Subgrade	Centreline	Remediated	Install 5TE Sensor
TG5	1.07	10	Subgrade	Centreline	Remediated	Install 5TE Sensor
DG1	0.70	5	Subgrade	Shoulder	Remediated	Read moisture profile using Diviner 2000

¹Sensor not functional.

3.2.3 Construction of Remediated Section and Installation of Subgrade Sensors

On April 23, 2019, the removal of a 22 m (72 ft) long track panel was performed to proceed to the excavation of 0.56 m (22 in.) of soil from the track, i.e., the ballast and sub-ballast layers. With the help of an excavator, two trenches with 0.7 m and 0.8 m of depth were excavated approximately 0.6 m apart in the subgrade to place the 5TE sensors (Figure 3.9). Due to time constraints, only two TG sensors were inserted in the subgrade. These sensors' installation depths were defined as 0.91

m (36 in.) and 1.07 m (42 in) below the tie bottom surface at the track centerline (Clifton, 2019). In order to avoid cutting through the wicking geotextile and possibly damaging its wicking capacities, the installation of sensors at the subgrade was done before placing the geotextile (Figure 3.10). No access pipes were installed for these sensors for the same reason.



Figure 3.9. Track Section Excavation on April 23, 2019 (Abdulrazagh 2019 – with permission).

The excavated trenches were covered by the subgrade material after the installation of the 5TE sensors. The placement of the subgrade material was followed by the installation of Mirafi® H2Ri geotextile with dimensions of 7.3 m x 0.61 m (23.62 ft x 24 in.) over the subgrade, with its ends coinciding with the ends of the shoulders of the sub-ballast layer. In order to cover the entire track width, two sheets were placed with a 0.15 m (6 in.) overlap at the centre (Figure 3.11). Sub-ballast was placed above Mirafi® H2Ri then graded and compacted. The compaction was followed by the installation of Mirafi® RS580i with dimensions of 4.6 m x 0.61 m (15.1 ft x 24 in.) (Figure 3.12). The repaired track panel was reinstalled, and the embankment was filled with clean ballast material. The track was then regulated, surfaced, and lined (Figure 3.13). The access pipes for the sub-ballast sensors could not be installed during this process because they would hinder the placement of the reinforcing geotextile while also being prone to damage due to the compaction of the railway embankment layers and construction works. Therefore, their installation occurred on the second day, after this section of the track was completely rebuilt.

On the second day, another track panel section in a length of 78 ft (23 m) was removed and repaired. The ballast and sub-ballast layers were removed to install Mirafi® H2Ri with a 0.15 m (6 in.) overlap at the track centreline. The track was backfilled using sub-ballast material on top of

Mirafi® H2Ri. The material was graded and compacted after its placement. The procedure was followed by the installation of Mirafi® RS580i above the sub-ballast and the track panel placement. The track was then filled with clean ballast that was shaped, distributed, and tamped, leaving the repaired track with a total length of 150 ft (46 m).

Table 3.7. Repair Dimensions.

As-built dimensions (m)	
Repaired length	45.7
Installed Width of Mirafi® H ₂ Ri	7.3
Width of Mirafi® RS580i	4.6
Thickness of ballast	0.38
Thickness of sub-ballast	0.18



Figure 3.10. Subgrade sensor buried with an electric shield on April 23, 2019 (Abdulrazagh 2019 – with permission).



Figure 3.11. Sub-ballast placement over geotextile on April 23, 2019 (Abdulrazagh 2019 – with permission).



Figure 3.12. Mirafi® RS580i over compacted sub-ballast layer on April 23, 2019 (Abdulrazagh 2019 – with permission).



Figure 3.13. Harsco equipment tamping and lining the track on April 24, 2019 (Clifton Associates, 2019).

3.2.4 Installation of Access Pipes

On the first day of construction, only sensors TG4 and TG5 were placed in the subgrade. On the second day, while the reconstruction of another part of the track was in progress, 10 access pipes were placed in both control and remediated sections for the installation of 5TE sensors and Diviner access pipes.

On April 24, 2019, a trench was dug for each access pipe in the ballast (Figure 3.14). At the remediated section, the trenches were dug before dumping the final layer of ballast for leveling the track panel. The sub-ballast and subgrade materials were dug through the trenches by a gas-powered earth auger (Figure 3.15) while using a sledgehammer and local excavator to push down the PVC pipes into the soil. A total of ten access pipes were installed. Eight of these pipes were used for 5TE sensors, and the remaining two allowed the use of the Diviner 2000 portable probe for moisture profile readings.



Figure 3.14. Trench boring for access pipe on April 24, 2019 (Abdulrazagh 2019 – with permission).



Figure 3.15. Installation of access pipes in the track on April 24, 2019 (Abdulrazagh 2019 – with permission).

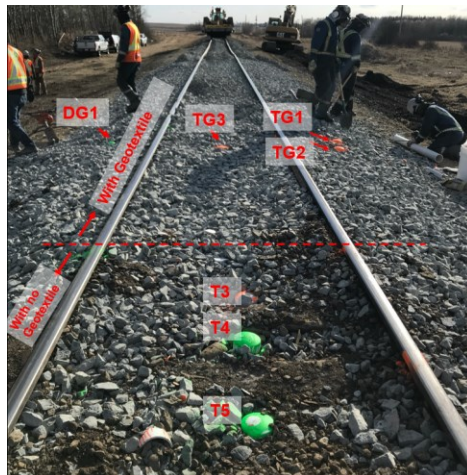


Figure 3.16. Site after installation of access pipes (Alvarenga et al. 2020).

After the placement of pipes, the final layer of ballast was placed, shaped, distributed, and compacted. Figure 3.16 shows the final access pipe setup. The pipes' caps were painted with

different colors to identify the layers in which they are installed. Orange caps represent the pipes installed at the sub-ballast, while the pipes with green caps go down to the subgrade layer.

3.2.5 Installation of Sensors and Dataloggers

Eight 5TE sensors were placed in the base of the access pipes on May 15, 2019. It was possible to place the sensors manually at the sub-ballast, while a notched pipe had to be used to push the sensors into the subgrade soil (Figure 3.17).

The sensors' wires were protected by electric conduits at their ends to avoid damage from upcoming tamping activities, train cyclic loading, as well as water damage near both the track and dataloggers. The protection consisted of plastic shields in the track (Figure 3.18) and metal conduits around the dataloggers (Figure 3.19).



Figure 3.17. 5TE sensors installation using a notched pipe on May 15, 2019 (Abdulrazagh 2019 – with permission).



Figure 3.18. Protection of wires using PVC electrical conduit on May 15, 2019 (Abdulrazagh 2019 – with permission).



Figure 3.19 - Protection of wires by metal electrical conduits where the cables could not be buried beneath the soil on May 15, 2019 (Abdulrazagh 2019 – with permission).

On July 9, 2019, two data loggers were set up at the site. For this study, two custom-made data loggers built by Kelvin Sattler at the University of Saskatchewan were used. The microcontrollers used for dataloggers are Arduino, with a Lithium-Ion Polymer battery (3.7V 6000mAh) and a solar panel connected for power (Figure 3.20(a)) (Sattler et al. 2021). More details on the datalogger operation and programming can be found in Sattler et al. (2020a) and Sattler et al. (2020b).



(a)



(b)

Figure 3.20. Datalogger set up on May 15, 2019 (a) before placing sensor wires and (b) after (Abdulrazagh 2019 – with permission).



Figure 3.21. Dataloggers ready for data collection.

3.2.6 Backfilling of Access Pipes

On July 23, 2019, all the 5TE sensors were covered with clean sub-ballast soil. The material was poured in layers that were gradually compacted to hold the sensors in place (Figure 3.22).

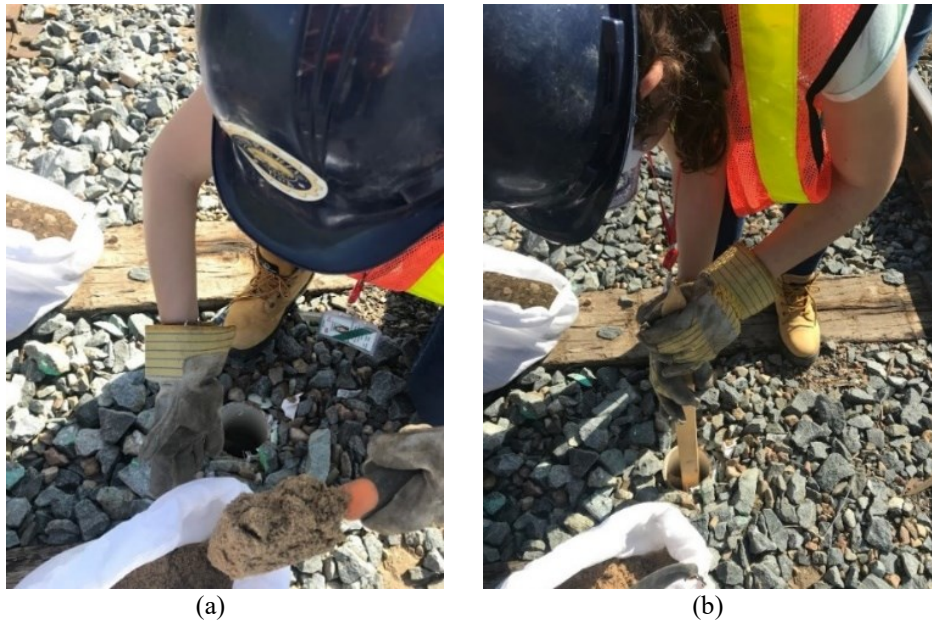


Figure 3.22. Insertion and compaction of sub-ballast soil into access pipes on July 23, 2019 (Abdulrazagh 2019 – with permission).

4. CHARACTERIZATION OF EMBANKMENT SOILS

When dealing with unsaturated soils, the classification tests acquire extra significance and meaning (Fredlund, 2006). These results were necessary to understand the soil behaviour and to verify the applicability of the method presented. This chapter presents the methodology behind each performed test, the results, and a final discussion regarding each soil tested.

4.1 Information on Soil Sampling

Scotford Ballast, Sub-ballast, and Subgrade were tested for different properties, briefly described in the following subsections. The sub-ballast of the remediated and control sections is denominated “clean sub-ballast” and “control sub-ballast”, respectively. The same applies to the ballast materials of both sections.

The samples from the control ballast, control sub-ballast, and subgrade were collected once the embankment was excavated down to each layer. The soil samples were collected using a shovel and then stored into plastic bags, and the depth from which the materials were collected is approximate. The control ballast top was sampled from the surface of the track between 0-13 cm of depth, while the control ballast bottom was collected at 13-33 cm of depth. The control sub-ballast was collected between around 33-55 cm of depth. All samples were taken from near the centreline of the track. The subgrade samples were obtained from the trenches excavated for the moisture sensors at a depth of around 80 cm. The clean ballast and sub-ballast placed in the reconstruction were sampled from the contractor's dump truck beside the track.

All samples were sealed in double plastic bags, identified, tightened with zip ties and transferred to a cold room 14 hours after completing the construction procedure. Table 4.1 shows the final weight of each soil collected at the site.

Table 4.1. Soil Sample Details.

Section	Soil Description	Final sample weight (kg)
Control	Ballast Top	25.1
	Ballast Bottom	17.2
	Sub-ballast	18.4
Remediated	Clean Ballast	45
	Clean Sub-ballast	87.5
Remediated and Control	Subgrade	104.6

4.2 Laboratory Testing Methodology

The relationship between moisture content and soil suction is used to estimate properties such as strength and permeability of unsaturated soils. Tests such as moisture content, particle size distribution, specific gravity, Atterberg limits, SWCC, and DST were performed to analyze the influence of the soil moisture on its strength.

4.2.1 Moisture Content

All moisture content tests were performed following the standard method specified in ASTM D2216-19: Standard Test Methods for Laboratory Determination of Water (Moisture) Content of Soil and Rock by Mass.

According to ASTM D2216, the minimum weight to characterize a representative sample depends on the maximum particle size. The minimum specimen mass determination for each soil layer was determined by performing visual and sieve analyses.

The test was performed two days after collecting samples at the site to ensure minimum moisture loss before the test. The soil was mixed thoroughly and transferred to weighed containers to determine the initial weight. Then, the specimens were put into an oven at the temperature of 110°C and weighed periodically until their mass was constant.

4.2.2 Particle Size Distribution (PSD)

The grain-size distribution curve bears a relationship to the distribution of pore sizes or void spaces. Consequently, the grain-size distribution becomes of increased value for understanding the unsaturated soil behavior. The following standard methods were used for the analysis:

- ASTM D6913/D6913M - Standard Test Methods for Particle-Size Distribution (Gradation) of Soils Using Sieve Analysis
- ASTM D7928 - Standard Test Method for Particle-Size Distribution (Gradation) of Fine-Grained Soils Using the Sedimentation (Hydrometer) Analysis

ASTM D7928 was only used to determine the particle-size distribution of the subgrade since the ballast and sub-ballast did not present a significant percentage of fine-grained material.

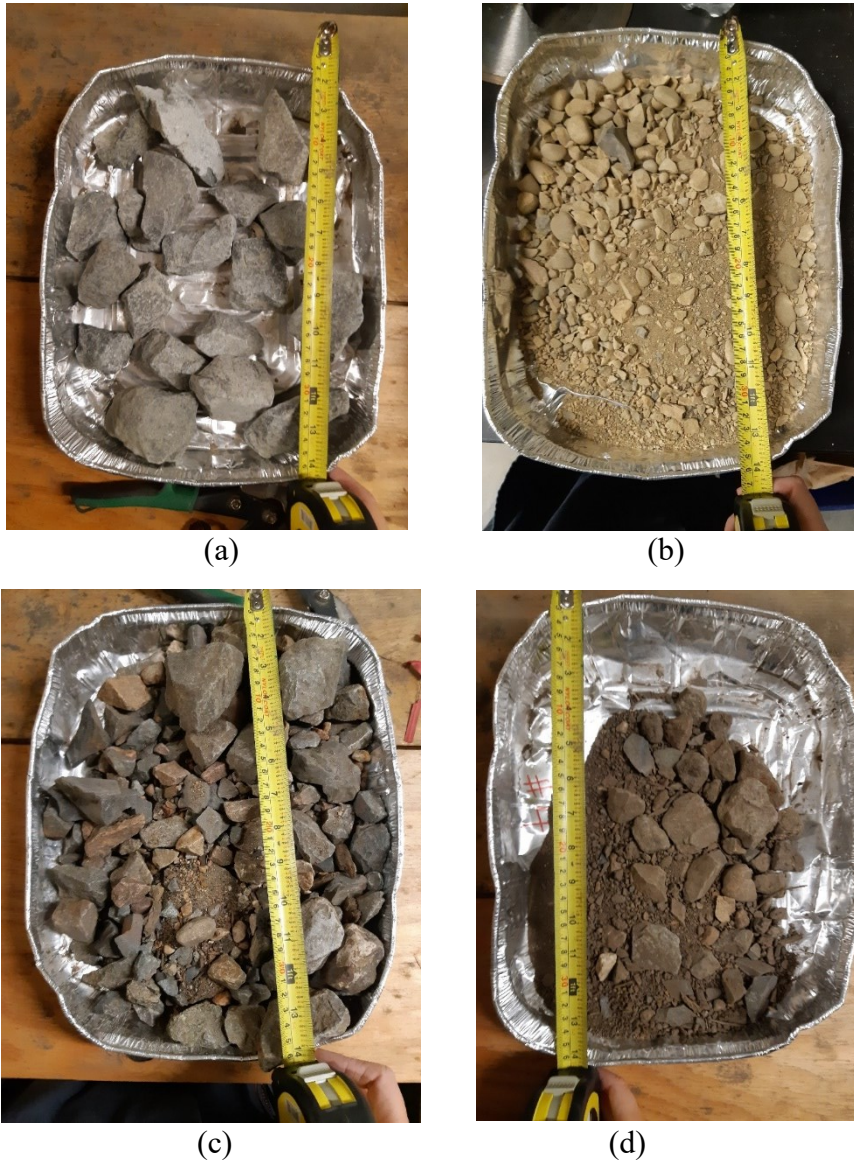


Figure 4.1- Samples of the embankment materials. (a) Clean ballast (b) Clean sub-ballast, (c) Control Ballast and (d) Control Sub-ballast.

For the sieve analysis, specimen preparation was conducted according to the oven-dried procedure in ASTM D6913. All the specimens were then washed on sieve #200 to remove fine particles, oven-dried, and sieved.

The stack of sieves was arranged depending on the soil tested. When the stack of sieves required did not fit into the shaker, the stack was divided into two portions. The first part consisted of the sieves that retain the larger particles. Then, the material passing this stack was poured onto the top of the other stack of sieves. The stack of sieves was placed in the mechanical shaker for 10 minutes for all tests.

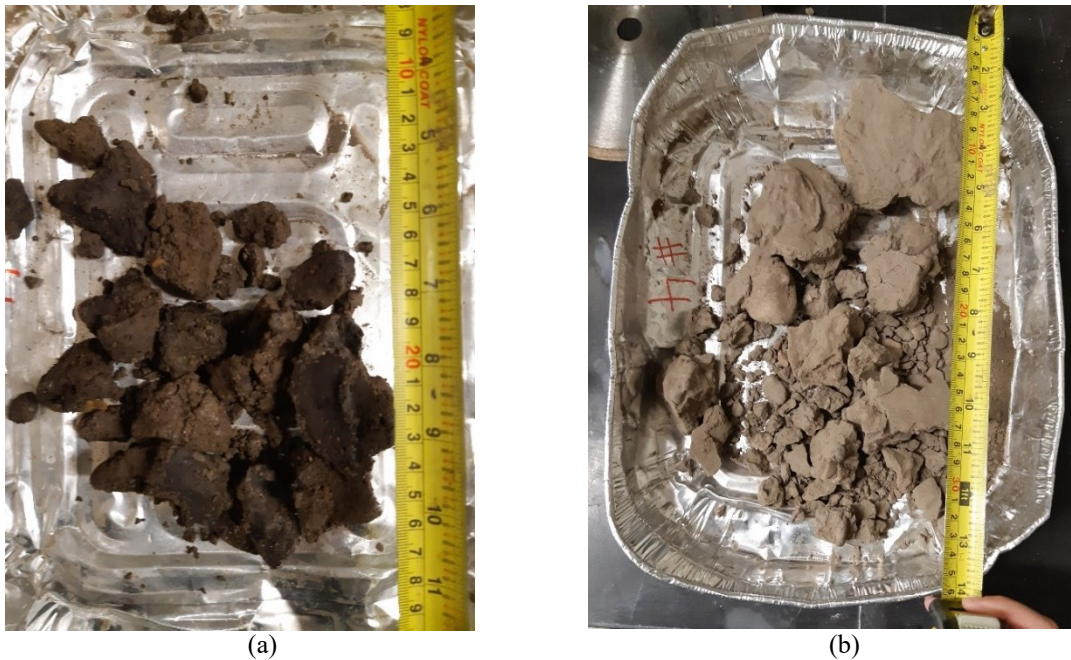


Figure 4.2-Subgrade sample in (a) wet and (b) dry conditions.

The weight of soil retained on each sieve was measured and recorded. The total weight from all sieves was compared to the original weight taken at the start of the test to ensure the soil loss was not more than 2% for each test. After recording the weight and assuring the quality of the test, the percent retained on each sieve was calculated by dividing the weight retained on the sieve by the original sample weight.

The hydrometer analysis was required only for the subgrade soil, which presented a high percentage of material passing sieve No. 200 ($<75 \mu\text{m}$). The sample for this material was obtained by oven-drying and grinding the material using a soil crusher. After sieving the material using sieve No. 200, 50 g of the passing material was collected for the test.

For calibration, two 1000 ml graduated cylinders were used. The first was filled with distilled water, and the second with sodium hexametaphosphate solution. The soil sample was poured into a 250 ml beaker along with 200 ml of sodium hexametaphosphate solution and mixed thoroughly. Then, the solution was transferred to a 1000 ml graduated cylinder, and the soil was washed directly into the cylinder using distilled water at room temperature. The cylinder was filled up to the 1000 ml marking, closed with a rubber lid and shaken for 1 minute.

After shaking the cylinder, the time was recorded, and the hydrometer was inserted into the solution 1, 2, 4, 8, 15, and 30 minutes after the start of the test. Afterward, the interval increased hourly, and measurements were made at 1, 2, 4, 8, 16 and 24 hours after the cylinder was put on the table. The hydrometer was inserted about 30 seconds before each reading, so it had time to settle appropriately until the result was recorded.

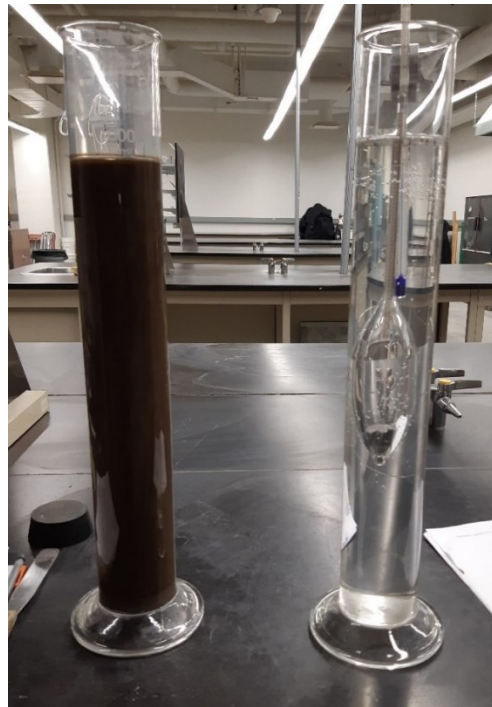


Figure 4.3. Hydrometer Test Setup.

4.2.3 Specific Gravity of Soil

This test was performed for the sub-ballast and subgrade soils following the standards specified in ASTM D854-06: Standard Test Method for Specific Gravity of Soil Solids by Water Pycnometer. Since the subgrade material would cement after being oven-dried, Method A (wet preparation) was chosen was used to facilitate the handling of the soil.

The pycnometer was filled with de-aired water above the calibration mark after its mass was measured to the nearest 0.01 g. The flask was submitted to a vacuum to take the air out of the water, leaving no bubbles. The excess de-aired water (above the mark) was taken out of the flask for the calibration measurements.

The soil passing the 4.75-mm sieve was separated into portions of approximately 100 g of soil. With the soil poured into a bowl, 100 mL of water was added to the sample. The solution was blended and poured into the pycnometer, avoiding any loss of soil. Entrapped air in the soil slurry was removed by vacuum, and the pycnometer was continually agitated under vacuum for at least 2 h. After air removal, the pycnometer mass and temperature were measured to the nearest 0.01 g using the balance used for the pycnometer calibration.



Figure 4.4. Vacuum procedure in soil mixture for specific gravity test.

4.2.4 Atterberg Limits

The presence of cohesive particles in soils causes them to have four states: solid, semi-solid, plastic, and liquid. Its state depends on its moisture content and how much water it has absorbed. The divisions between these four states are defined as the Atterberg Limits (Braja, 2009).

The determination of these limits for the subgrade is essential to understand how the soil behaves at a specific moisture content. The tests presented in this section were performed according to ASTM D4318 – 17: Standard Test Methods for Liquid Limit, Plastic Limit, and Plasticity Index of Soils. The wet preparation method (Method A) was performed according to ASTM D4318 – 17.

First, the specimen preparation required to soak the soil (Figure 4.5) to dissolve the lumps; then, the soil was washed through sieve No. 40. With the washing process, the soil ended up with a

significant amount of water. Thus, the sample was left air-drying until its consistency required 25 drops of the Casagrande cup to close the groove.

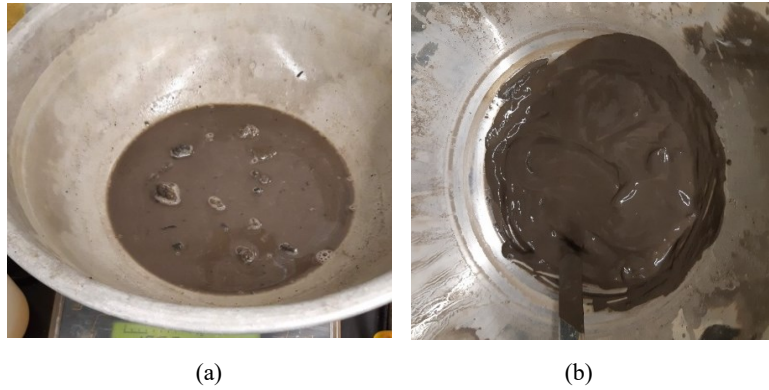


Figure 4.5. Wet preparation method of the specimen for liquid and plastic limit tests. (a) Soaked soil (b) Washed soil after drying for a few days.

A portion of the soil was then placed and spread into the cup, forming a horizontal surface. A groove was made in the soil in one stroke, maintaining the grooving tool perpendicular to the cup surface. Then, the crank that lifts the Casagrande cup was turned 2 times per second until the two halves of the soil pat came in contact at the bottom of the groove along 13 mm (Figure 4.6). This process was repeated until 4 data points were acquired, allowing some time intervals between tests to let the soil dry and reach different consistencies/moisture content values.

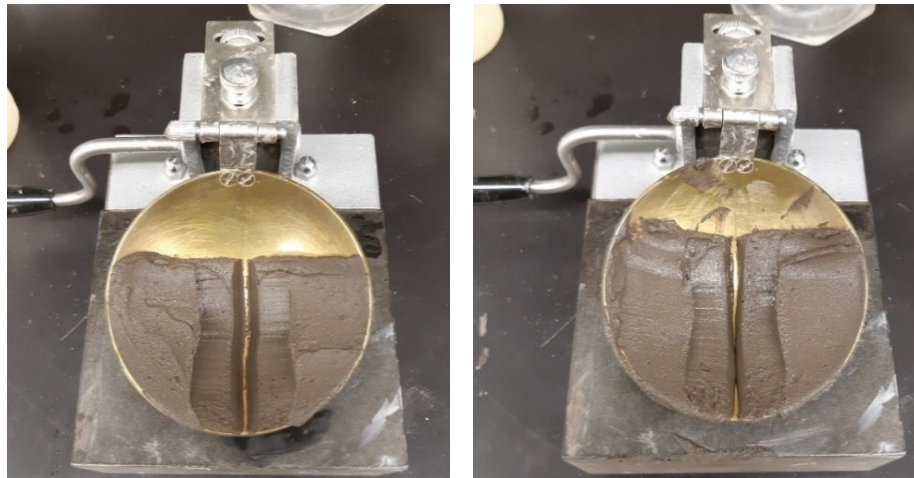


Figure 4.6. Liquid Limit Test.

The plastic limit of the soil is the lower moisture content at which the soil can be molded. According to the ASTM D4318, the test consists of rolling threads of soil until it crumbles when reaching 4.2 mm in diameter.

Initially, about 50 g of the soil prepared for the liquid limit test is separated for the plastic limit test. Therefore, the same soil preparation procedure is valid for both tests. An amount of soil shaped in an ellipse is rolled until it reaches a diameter of 4.2 mm. If the soil did not crumble at this diameter, the sample needs to be rerolled until it crumbles at the determined diameter.

When reaching the situation shown in Figure 4.7, the crumbled thread is placed in pre-weighed cans and their mass is determined. Then, the cans are left in an oven with a temperature of 110°C to measure the corresponding moisture content at which the soil reached the plastic limit. Usually, three to four tests are necessary to determine the plastic limit.



Figure 4.7. Plastic Limit sample after crumbling.

4.2.5 Soil-Water Characteristic Curve (SWCC)

The soil-water characteristic curve is an important relationship to determine whether to apply unsaturated soil mechanics, which is increasingly being used in geotechnical engineering (Fredlund and Houston, 2013). Examples of an application include the empirical prediction of the permeability function and the shear strength properties of unsaturated soils (Fredlund and Xing, 1994).

SWCC tests were performed as specified in ASTM D6836 – 16 for the sub-ballast and subgrade materials from both sections. Tempe Cells with 1-bar and 5-bar ceramic plates were used to test a total of 6 samples. The saturation process was performed with the application of water pressure to the bottom of the Tempe Cell filled with soil using a water outlet for 24 hours. The excess water was then extracted from the sample by applying 0 KPa of suction until equilibrium occurred, i.e., no changes in the total sample mass occurred. The water was collected by a capillary needle placed at the end of the tube.

After reaching equilibrium, the initial sample height was recorded at three different locations along with the initial weight of the sample at a saturated state. For the hanging column test, a stand with measuring tape was used to determine the initial Datum and subsequent drops in the discharge tube. The setup for the hanging column method is displayed in Figure 4.8.

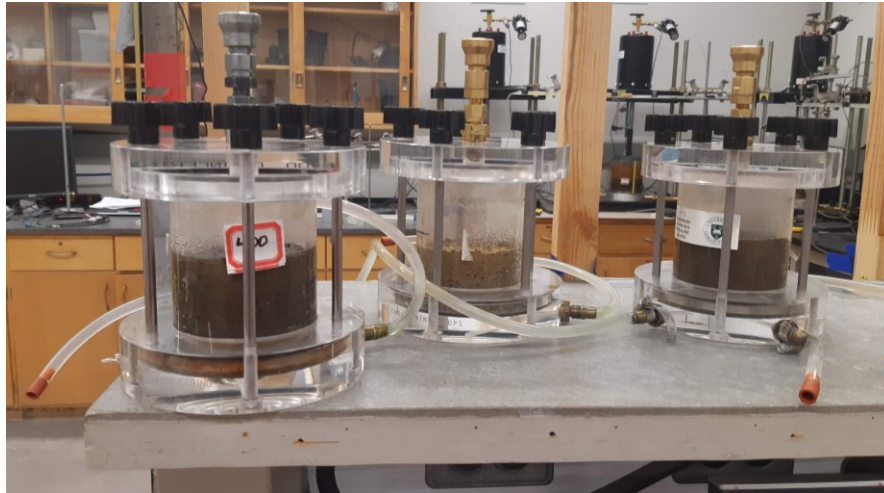


Figure 4.8. Hanging Column Test.

After reaching 1.5 KPa at the hanging column method, the samples were transferred to pressure valves for the application of high pressures. The gravimetric water content was determined for the specimens twice a day to monitor the weight variation related to water loss. When no changes in the sample weight were identified within 24 hours, the process was repeated to apply a higher pressure until finding enough points to perform the curve-fitting.

4.2.6 Consolidated Drained Direct Shear Test (CDDST)

The direct shear test is used for the determination of the consolidated drained strength properties of saturated soils. It consists of applying normal forces in increments to consolidate a soil sample while allowing excess pore pressure to dissipate.

The method applied for testing is specified in ASTM D3080/D3080M. Each sample was compacted within a metal ring matching the size of the shear box. If the soil surpassed the metal ring edges when compacted, the sample was then trimmed to match the ring dimensions. Consolidation was applied in stages to avoid damage to the sample, and the normal force increments did not exceed 2x the last force applied.

After the consolidation, the sample is submitted to deformation at a controlled rate in a specific shear plane. Drained conditions must occur during the entire test. The shearing rate was determined as

defined by ASTM D3080, which uses the soil classification to determine the minimum time of failure necessary to ensure excess pore-pressure has dissipated. The time to failure for the sub-ballast materials was estimated as 60 minutes with a shearing rate of 0.0081 cm/min, while the subgrade was submitted to a minimum time of failure of 18 hours, with a shearing rate of 0.00076 cm/min.

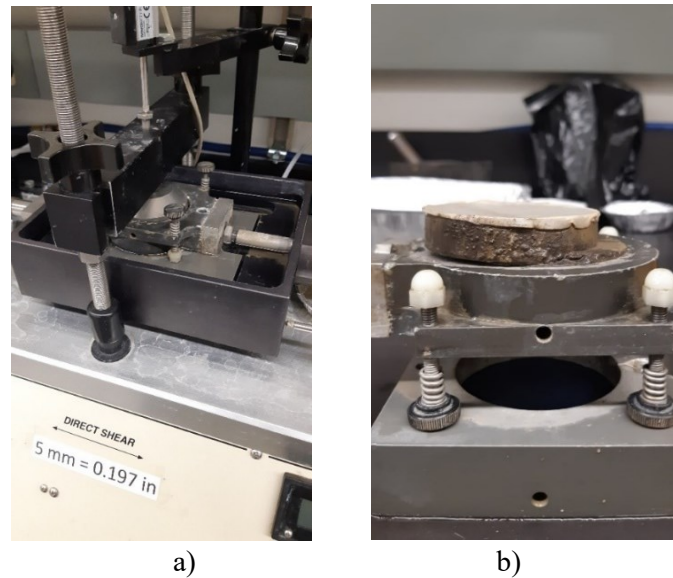


Figure 4.9. Direct Shear a) Test Setup and b) Subgrade sample after shearing.

4.2.7 In-situ Dry Density Test

The in-situ dry density is a fundamental property of the soil. A simple change in the density of a material can affect many of its properties, such as permeability, void ratio, moisture content, air-entry value, strength, and many others. Obtaining *in-situ* density information was very important to ensure that the test conditions were as close as possible to the field conditions.

The testing method applied is found at ASTM D1556/D1556M – 15: Standard Test Method for Density and Unit Weight of Soil in Place by Sand-Cone Method. This method uses a sand cone apparatus to determine the in-situ density and unit weight of soils.

After calibrating the sand container, a 1000 cm³ test hole was dug through the center hole of the secured base plate, and all excavated soil was placed in a moisture-tight container. The sand-cone apparatus was opened, and the mass of the apparatus with the remaining sand was recorded. The mass of sand used, the mass of the moist soil collected from the test hole, and the soil moisture content were then used to determine the dry unit weight of the material.

The test was only done for the subgrade material beside the track since testing was not possible within the embankment.

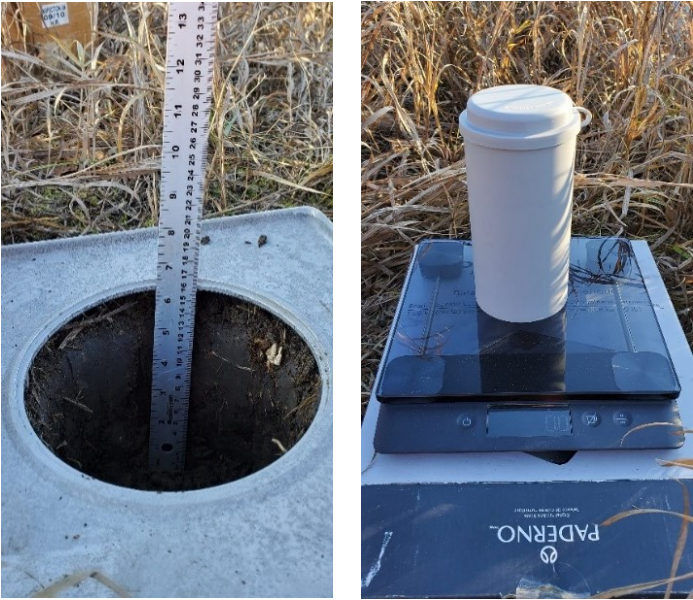


Figure 4.10- Field Dry Density Test procedure.

5. LABORATORY AND FIELD INSTRUMENTATION RESULTS

This section outlines the data collection, as well as the processing procedure for the analysis. Results and observations regarding the advantages, disadvantages and limitations of the method employed are also presented.




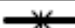


5.1 Laboratory Tests Results

The summary of results found for the performed tests is included in this section. Detailed test reports are available in Appendix I.

5.1.1 Soil Index Properties

The index properties of the embankment soils are summarized in Table 5.1. These properties include the particle size distribution (including D_{10} , D_{30} , and D_{60} from the PSD curve), percentage of fines, water content, specific gravity, field dry density, Atterberg limits, the plasticity index, and the USCS classification for each soil.

Table 5.1. Summary of geotechnical index properties of the embankment materials.

Location	Control (CS)			Remediated (RS)		Remediated and Control
	Ballast (top)	Ballast (bottom)	Sub-ballast	Ballast	Sub-ballast	Subgrade
Symbol						
Depth (m)	0.2	0.3	0.5	0.3	0.5	0.8
D_{10} (mm)	3	0.2	0.3	31.5	0.3	-
D_{30} (mm)	19.7	12.5	4.8	-	0.9	0.017
D_{60} (mm)	31.8	29.4	15.6	-	10	0.165
Passing #200	4.1%	8.1%	9.5%	0%	0.9%	50.8%
Sand	3.9%	9.3%	11.7%	0.0%	35.6%	28.7%
Gravel	92.0%	82.6%	78.8%	100.0%	63.5%	20.5%
w (%)	2.3%	3.7%	4.2%	0.2%	3.5%	20.6%
LL	-	-	-	-	-	40
PL	-	-	-	-	-	19
PI	-	-	-	-	-	21
G_s	-	-	2.71	-	2.68	2.73
ρ_d (g/cm ³)	-	-	-	-	-	1.9
USCS	GP	GP	GW	GP	GP	CL
AASHTO	A-1a	A-1a	A-1a	A-1a	A-1a	A-6

The particle size distribution curves were also defined and are presented in Figure 5.1. The control sub-ballast has shown a well-graded curve, while the clean sub-ballast section presented a gap-graded curve. The presence of gravels, sands and fine particles in the subgrade reinforces that this

material is composed of glacial till since glacial tills present a PSD similar to the one found for this material. Its AASHTO classification shows that this soil is within a fair to poor rating for subgrade material; therefore, this layer is the most important to be improved within the embankment.

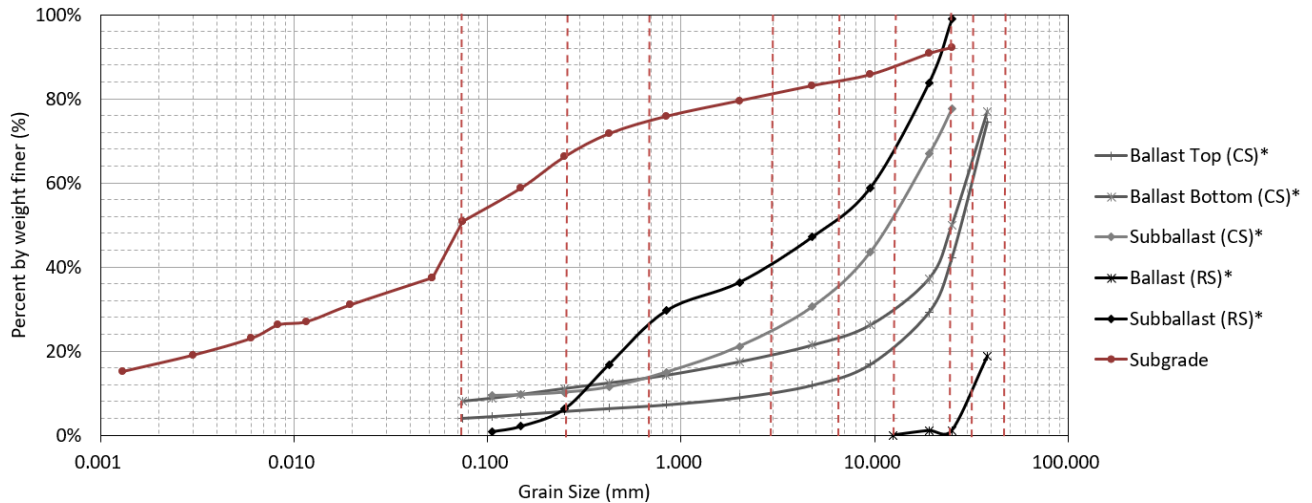


Figure 5.1. Grain-size analysis of embankment soils.

5.1.2 Soil-Water Characteristic Curve

The SWCC tests were defined in terms of matric suction vs. volumetric water content for all the embankment soils, except the ballast. The SWCCs are divided into clean sub-ballast (Figure 5.2), control sub-ballast (Figure 5.3), and subgrade (Figure 5.4). Curve-fitting for VWC vs. matric suction was performed using the Fredlund and Xing (1992) equation in SVOOffice 5. The plots represent the air-entry value (AEV) with a dashed red line. For the sub-ballast materials, the AEV found is between 0.7 to 1 kPa, with the control sub-ballast reaching around 0.8 kPa and the clean sub-ballast reaching almost 1 kPa. For the subgrade, the air-entry value ranges from 30 to 45 kPa for all tests performed. At the end of the test, the subgrade material presented cracks at the top of the sample, attesting to shrinkage occurrence.

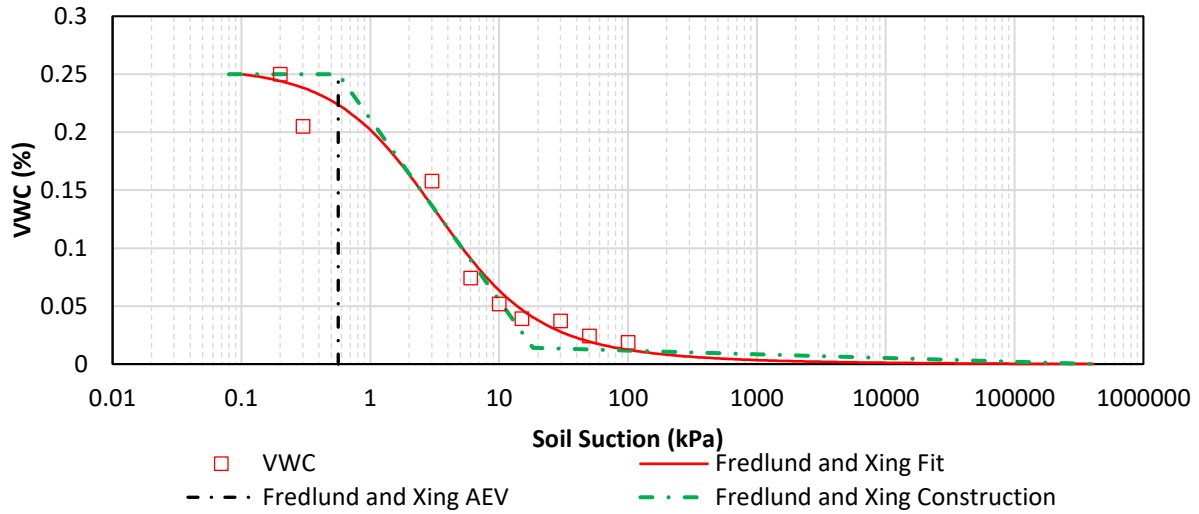


Figure 5.2. SWCC for clean sub-ballast.

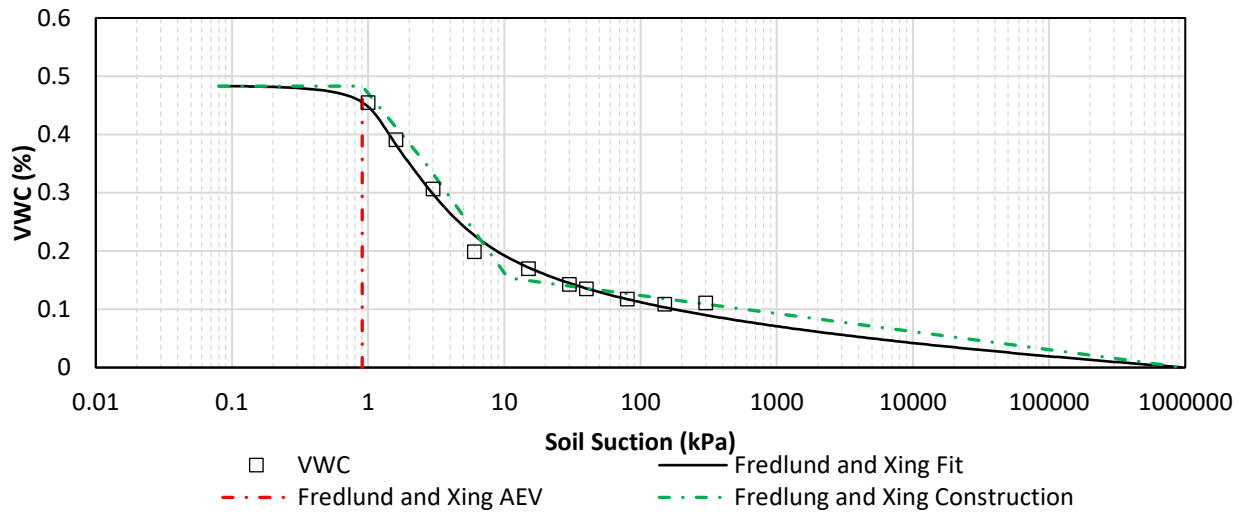


Figure 5.3. SWCC for control sub-ballast.

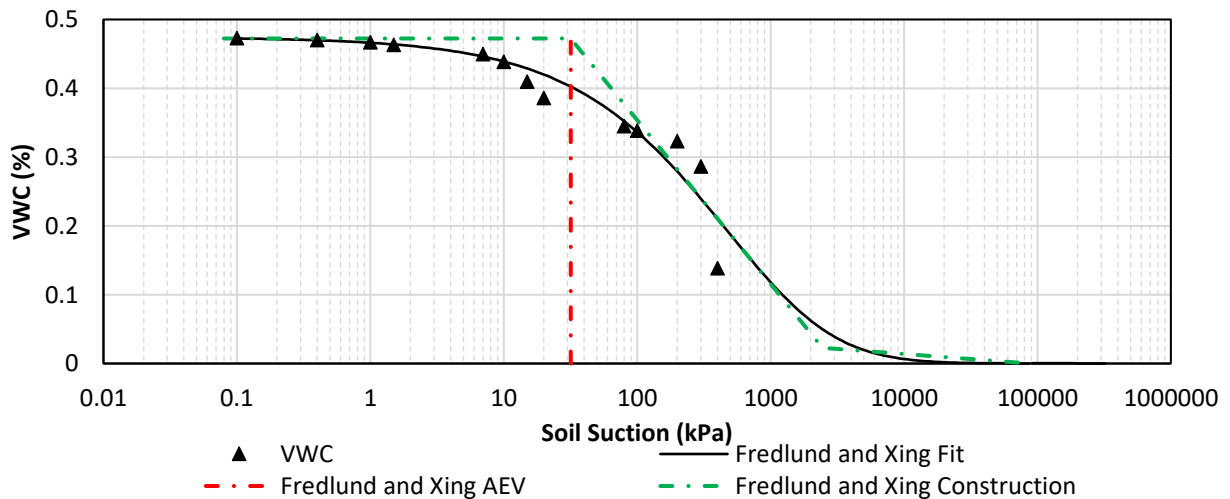


Figure 5.4. SWCC for subgrade.

5.1.3 Consolidated Drained Direct Shear

The direct shear tests performed on the sub-ballast materials and subgrade made it possible to measure the saturated strength parameters of the embankment materials. Remolded samples with a similar dry density as the one seen in the field were used for the tests. At least three tests were performed in these soils, and failure was assumed to occur when the displacement was higher than 10% of the box diameter.

For the control sub-ballast, the peak shear stress was reached after 4 to 6 mm of shear displacement (Figure 5.5). The sample submitted to 200 kPa of normal stress has also shown a second peak after reaching 7.8 mm of displacement. The clean sub-ballast reached its peak strength at around 2 to 4 mm of shear displacement for all samples (Figure 5.6). The subgrade has shown peak strength values at horizontal displacements within 2 to 3.7 mm (Figure 5.7). The sub-ballast soils presented over consolidated behaviour. The subgrade material, however, has shown volume changes associated with normally consolidated soils. Stress-displacement graphs from all the tests are shown in Appendix I.

Peak shear strength results are plot in the shear stress-normal stress space for each soil (Figure 5.8). The linear regression of the three tests performed for each soil type determined the Mohr-Coulomb strength envelope, and the function is divided into the effective strength parameters cohesion c' and friction angle ϕ' according to the following:

$$\tau = c' + \sigma' \times \tan(\phi') \quad (5.1)$$

The Mohr-Coulomb parameters c' and ϕ' for all soils are displayed in Figure 5.8. Within the sub-ballast materials, the clean sub-ballast has a friction angle of 35° while the control sub-ballast has a friction angle of 39° . The clayey subgrade presented an effective cohesion of 27 kPa and $\phi'=17^\circ$.

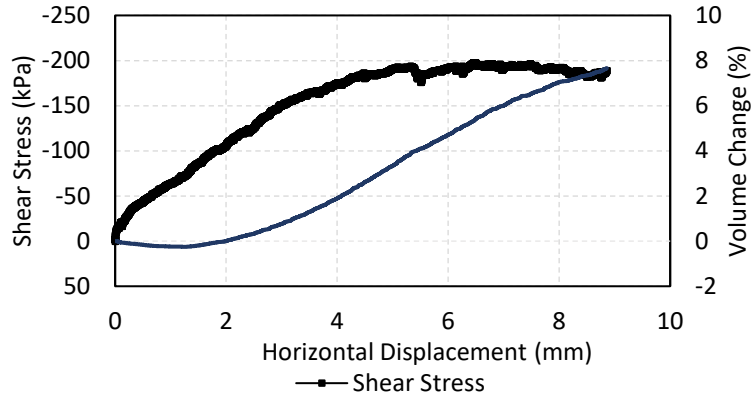


Figure 5.5. Shear vs. Horizontal displacements plots for Direct Shear test under normal stress of 100 kPa for Control Sub-ballast.

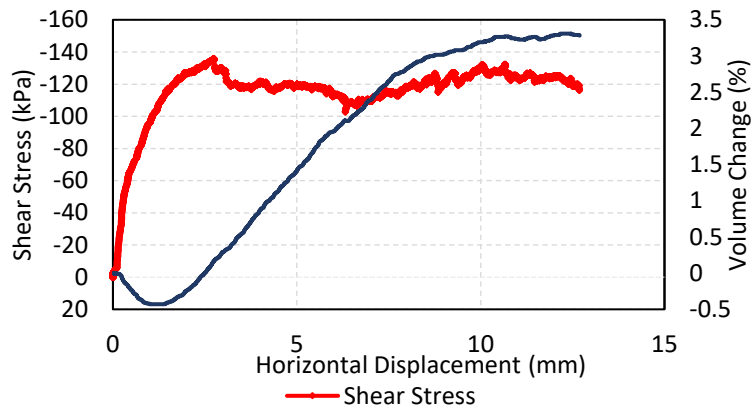


Figure 5.6. Shear vs. Horizontal displacements plots for Direct Shear test under normal stress of 100 kPa for clean sub-ballast.

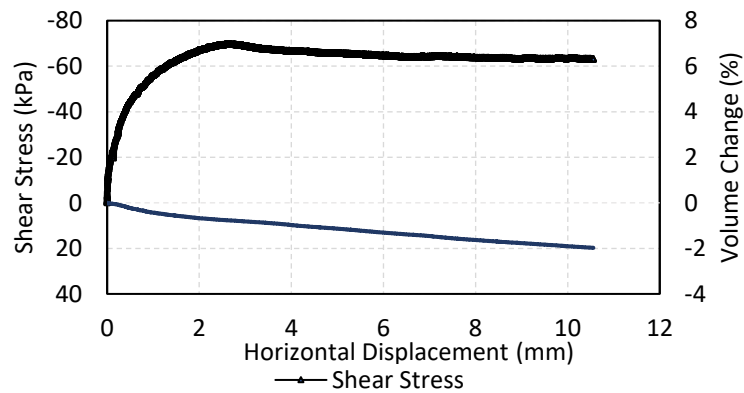


Figure 5.7. Shear vs. Horizontal displacements plots for Direct Shear tests under normal stress of 100 kPa for Subgrade.

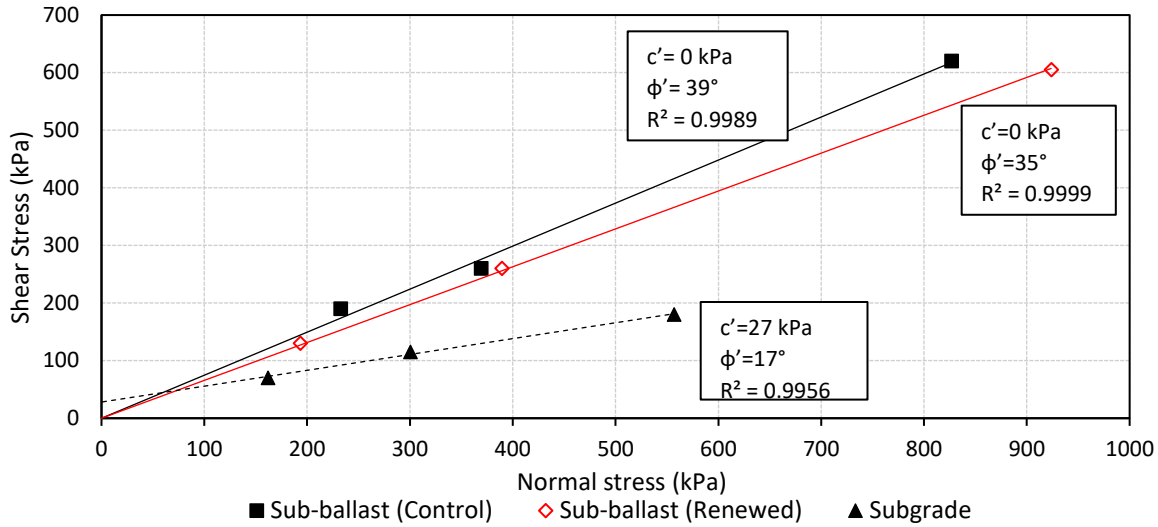


Figure 5.8. Shear Stress of Embankment Materials.

5.2 Field Data Collection

5.2.1 Field 5TE Sensors Data

Volumetric water content, electrical conductivity and temperature were recorded at an interval of 12 hours between July 2019- February 2021. One of the sensors, TG4, was damaged during the reconstruction of the reinforced embankment and did not function. This sensor was installed before the track reconstruction and cannot be replaced.

During winter, measurements performed at both sections had issues due to humidity occurrence in the dataloggers. The data from the mentioned intervals was not stored by the dataloggers. Table 5.2 describes the dates of missing data and the issues associated with them.

Table 5.2. Issues found during data collection.

Date	Section	Description
09/07/2019-18/09/2019	Control	Issues with battery and solar charging system caused the datalogger to read moisture only when computer was connected.
19/04/2020-03/08/2020	Control	Faulty readings only for T1 sensor due to unknown reasons.
08/09/2020-17/09/2020	Control and Remediated	Data storage capacity reached; readings could not be stored.
04/08/2020-04/09/2020	Remediated	Readings from TG5 were not collected for unknown reasons (could be related to the storage capacity being low).

The VWC data from the 5TE sensors were plotted along with precipitation data from the weather stations to determine the trends in both variables and whether they may bear a relationship (Figure 5.9). The daily average of the readings was used. All the data related to the remediated section (TG) and the control section (T) are shown in red and black, respectively.

Figure 5.9 makes it possible to observe that sharp increases in the VWC read by the sensors are related to peaks in the precipitation recorded at the weather stations. This behaviour confirms that precipitation is the primary source of moisture within the embankment (Figures 5.9(a)-5.9(c)) and at the subgrade surface as evidenced by sensor T4 (Figure 5.9(d)).

We can see two conflicting behaviours for the sensors in the sub-ballast shoulder of the remediated track. While showing higher moisture levels throughout the entire study, moisture changes were less or equally prominent at the remediated section compared to the control section (Figures 5.9(a) and 5.9(b)).

The sensors at the sub-ballast centreline (Figure 5.9(c)) have shown similar VWC for both sections, but the remediated section has shown smaller moisture fluctuations and presented lower VWC measurements during moisture/precipitation increases in comparison with the control section. Nonetheless, the remediated section presented slightly higher VWC values when the moisture decreased after a few days with low or no precipitation relative to the control section.

From all the sensors at the subgrade (Figure 5.9(d)), T4 is the one that displayed the best correlation with precipitation. This trend was expected since T4 is the closest to the surface (0.65 m depth). The other sensor at the control section (T5) presented a contrasting behaviour for 2019 and 2020. In 2019, the VWC of this sensor remained around 26% throughout the Summer without any significant changes with precipitation. On the other hand, after the spring thawing of 2020, the sensor presented VWC variations with precipitation events. It is also visible that during a dry period in September/October 2020, the response of T5 presented a considerable decrease in VWC due to the lack of water source (Figure 5.9(d)). Due to this decrease, the VWC levels of T5 eventually converged to the VWC values found at the remediated section and reached lower VWC values afterward. Sensor TG5, the only functioning sensor at the remediated section (represented in red in Figure 5.9(d)), has shown little to no disturbance in its VWC even on days of high precipitation, indicating that the remediation potentially decoupled the VWC of this layer from precipitation events. Besides, TG5 showed only a slight decrease in its VWC levels during the dry period in September/October 2020.

The soil temperature data from the sensors were plotted to aid with the visualization of when the water in the soil could potentially change to a solid state. The temperatures read by the sensors through time are shown in Figure 5.10.

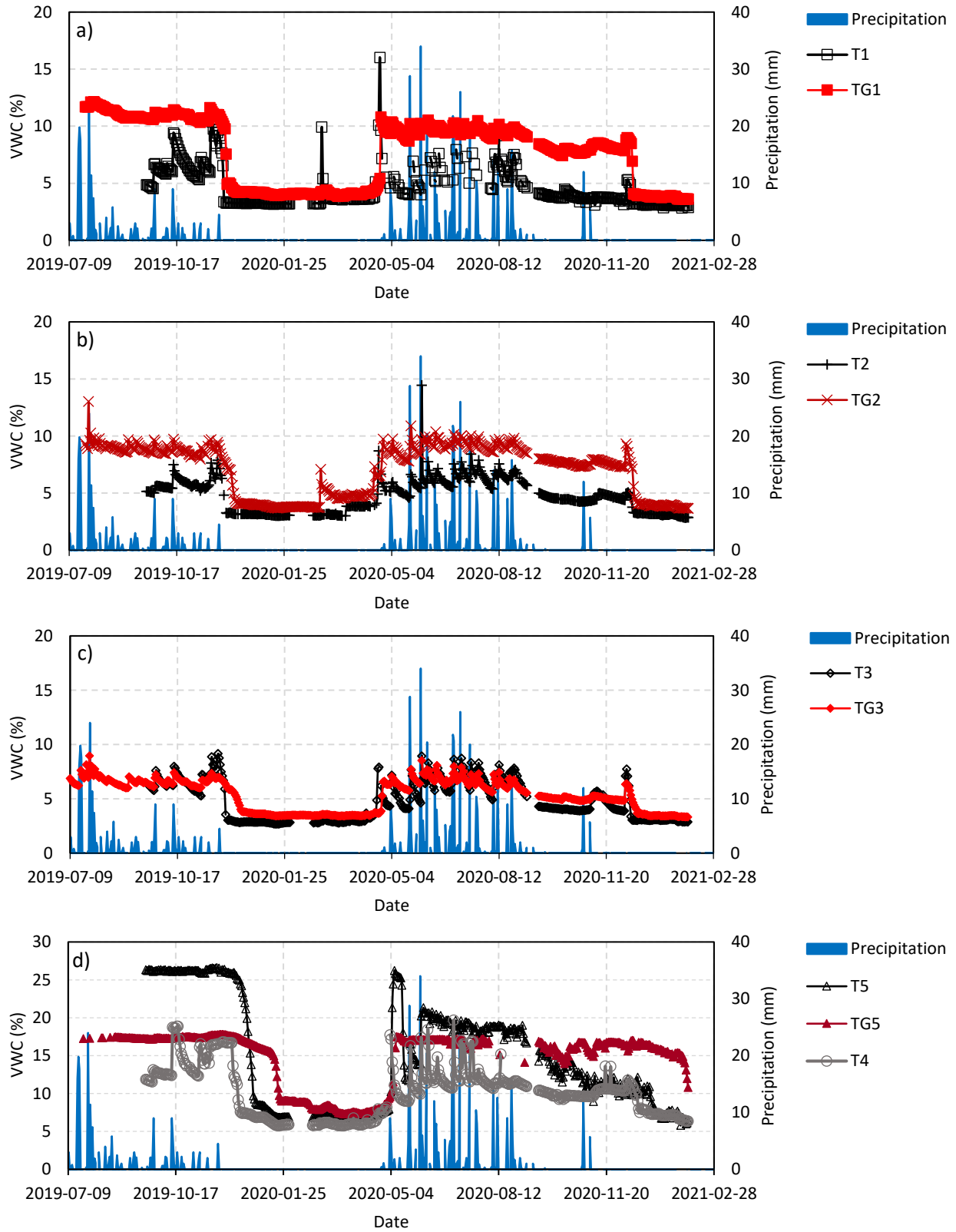


Figure 5.9- Volumetric Water Content from a) T1 and TG1 (Sub-ballast shoulder), b) T2 and TG2 (Sub-ballast shoulder), c) T3 and TG3 (Sub-ballast centreline) and d) T4, T5 and TG5 (Subgrade centreline).

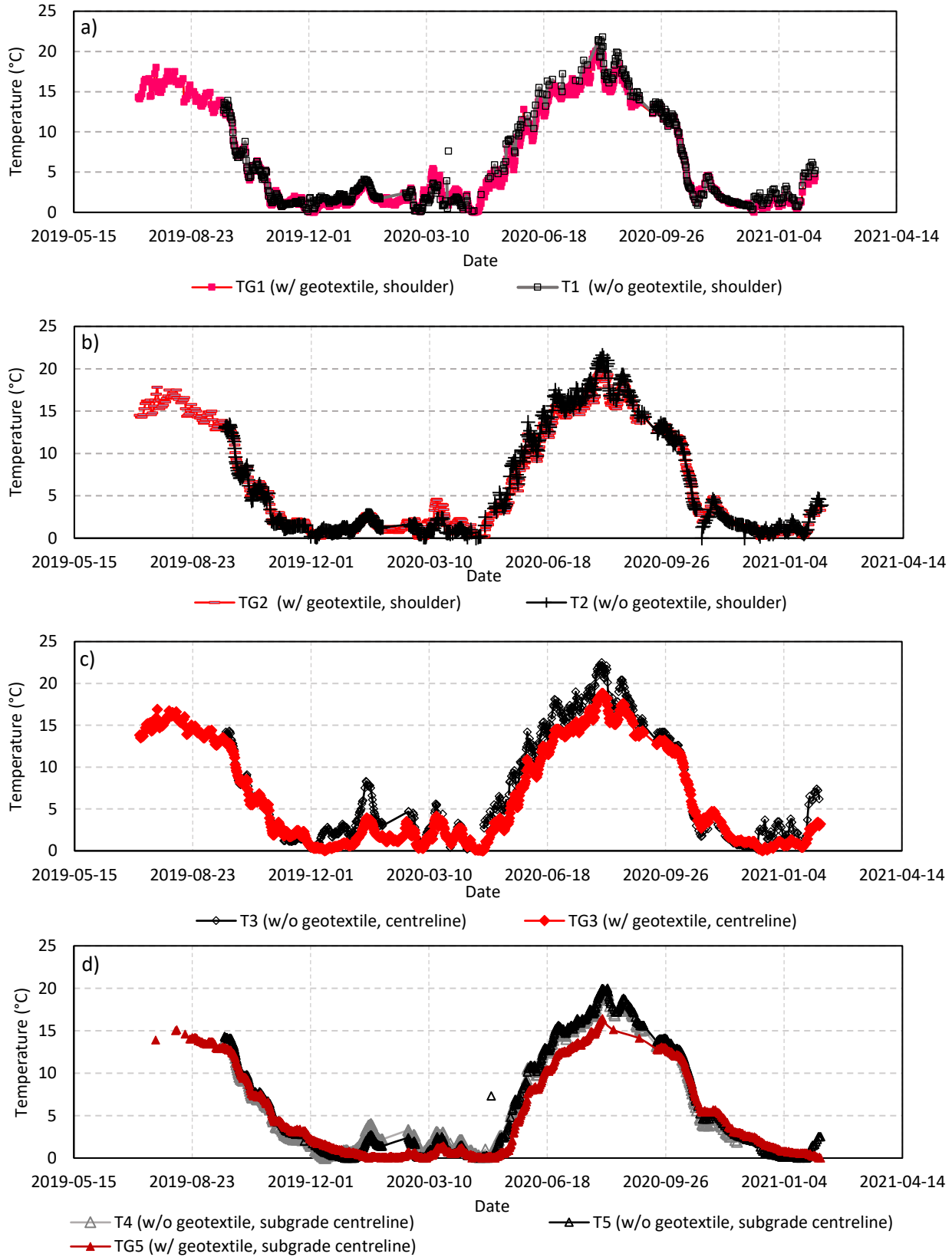


Figure 5.10- Temperature readings through time for all sensors at a) T1 and TG1 (Sub-ballast shoulder), b) T2 and TG2 (Sub-ballast shoulder), c) T3 and TG3 (Sub-ballast centreline) and d) T4, T5 and TG5 (Subgrade centreline).

Meter Environment (2018) mentions that the volumetric water content (VWC) readings from frozen soil are similar to dry soil. Considering that, the period in which the soil displayed temperature readings close to 0° C was removed from the analysis. The intervals chosen for the analysis were July 24, 2019 – November 18, 2019, and February 25- November 25, 2020.

5.2.2 Diviner 2000 Data

Diviner 2000 measurements are manual and thus intermittent, and 10 readings were performed between November 2019- February 2021. Some readings were limited in depth due to ice or water presence within the access tube (Figure 5.11).

While the sub-ballast readings showed results close to what was found by the 5TE sensors, most of the readings collected at the subgrade material showed considerably different values compared to the 5TE sensors readings from the same day. However, the Diviner readings in the subgrade were collected at a different depth and position than the 5TEs, and the results could differ due to this discrepancy.

The data from the 5TE sensors was prioritized in the analysis due to the higher frequency of data collection and the greater repeatability of readings relative to the Diviner 2000 measurements.

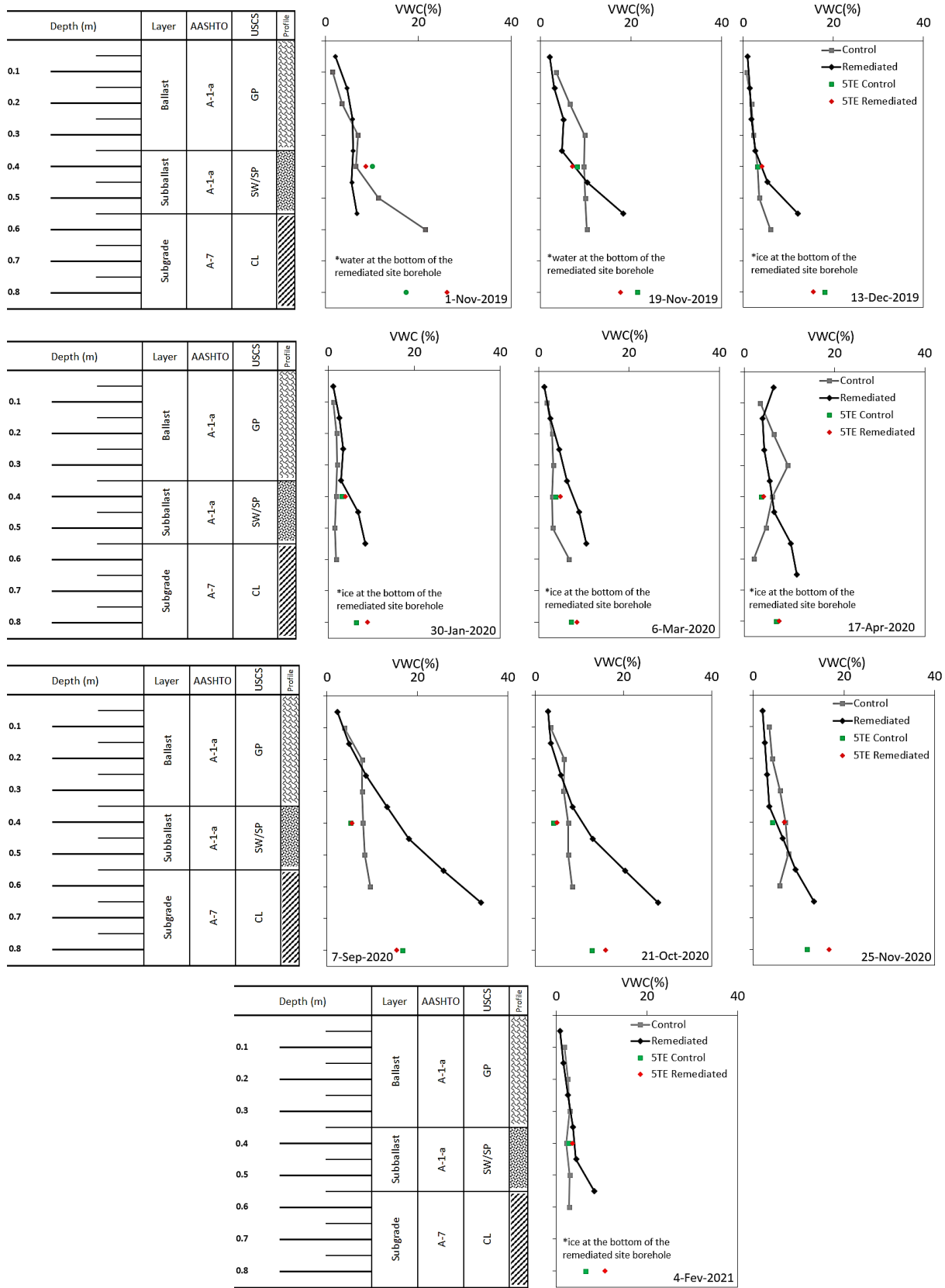


Figure 5.11- Diviner 2000 readings performed at Scotford Mile 153.8.

6. ANALYSIS AND DISCUSSION OF RESULTS

An analysis using VWC, precipitation and laboratory data was performed to investigate the effect of the reconstruction method on the moisture and strength levels of the embankment and subgrade materials. The details on the data processing methodology, results and observations are presented in the following subsections.

6.1 Field Climate Information

Temperature and precipitation data from the years 2008-2018 were used to determine the historical profile of the region and the profile for 2019-2020 (Alvarenga et al. 2020). The average temperatures for 2019 and 2020 were similar to the 10-year average, except for January/2019 and February/2020, which presented a colder temperature than expected. Figure 6.1 presents the average temperature found in historical data and the temperature averages by month for 2019 and 2020.

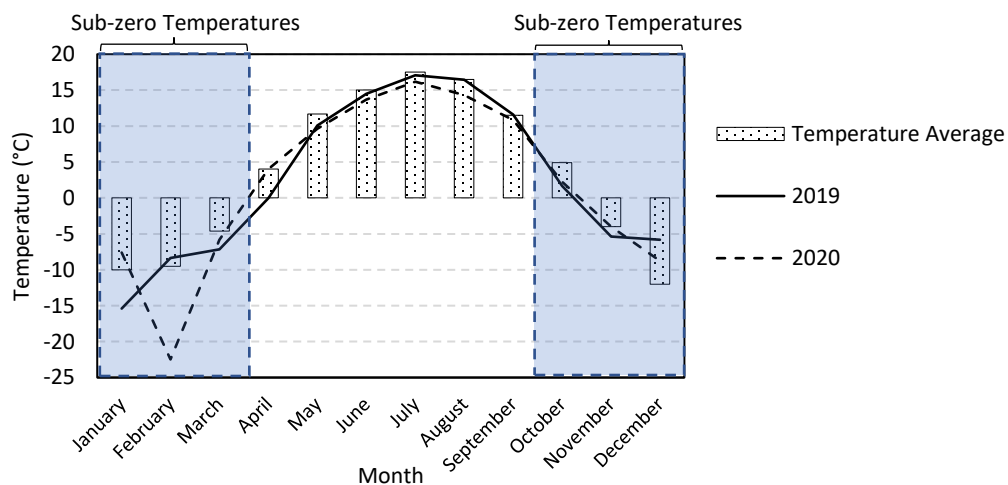


Figure 6.1. 10-year average temperature (2008-2018) vs. recorded temperatures (2019-2020) (ECCC, 2020).

Both years presented atypical precipitation profiles, with the year 2019 presenting a surplus while 2020 presented a deficit in its precipitation levels. One of the most noticeable differences is seen in May, June and August/2019, as these months presented almost 2x the amount of precipitation expected. April, September and October, however, presented less precipitation than expected in both years.

The estimated average yearly precipitation for the historical data was 553 mm. In comparison, 2019 had a total of 663 mm in precipitation. The year 2020, on the other hand, only presented 524 mm of precipitation. These differing trends can potentially change the outcome of VWC for each

year accordingly. The 10-year average of precipitation with the trends from 2019-2020 is shown in Figure 6.2.

Within the historical data, the year 2016 also presented an unusual amount of rainfall. The total precipitation for May was 130 mm, and it was followed by months with amounts between 75 to 94 mm/month.

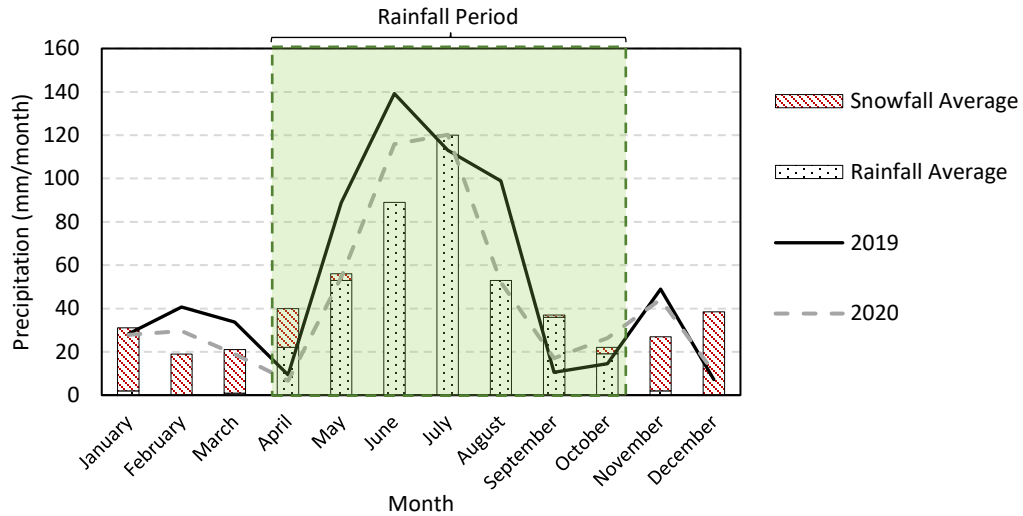


Figure 6.2. 10-year average precipitation (2008- 2018) vs. recorded precipitation (2019 and 2020) (ECCC, 2020).

6.2 Antecedent Precipitation Model

Total precipitation values were processed using the API model shown in Section 2.4.3, aiming to understand the relationship between soil moisture content and precipitation. This analysis worked as a means to verify the effectiveness of the reconstruction on drainage performance.

The first step was to separate the VWC data for each year cycle (Summer 2019- Fall 2019, Spring 2020-Fall 2020) to address the yearly precipitation variability. Then, the attenuation coefficient k and the number of days to be used for the API were estimated. These parameters were simultaneously determined by finding the best-fit values (R^2) for all sensors installed at similar locations. Graphical interpretation of the VWC vs. API was performed for each sensor using the linear regression model shown in Equation 6.1. This process aimed to optimize the quantification of the VWC variation with precipitation.

$$\theta_{v(t)} = \alpha \times (API) + \beta \quad (6.1)$$

Where α and β are fitting parameters, and $\theta_{v(t)}$ is the measured VWC for day t. The number of days considered and the values found for k are found in Table 6.1 and Table 6.2, respectively.

Table 6.1. Number of days considered in the API model for each track location.

Location		# of days
Sub-ballast	Shoulder	16
	Centreline	14
Subgrade	Centreline	17

Table 6.2. Summary of attenuation coefficients used for each track location.

Years \ k	Sub-ballast		Subgrade
	Shoulder	Centreline	Centreline
2019	0.94	0.94	0.95
2020	0.93	0.93	0.96

Figures 6.3, 6.4, and 6.5 show the VWC and API through time for the sensors separated by track location. The correlation between precipitation and VWC variation is evident, with peaks of VWC coinciding with days of steep increases in API. At a certain period of 2020, API became very low and went to zero. This period occurred between October 9 – October 28, 2020, caused by the absence of precipitation from September 25 – October 28, 2020. It was then observed that most the precipitation registered in October displayed in Figure 6.2 took place on the two last days of the month. Whenever this extended period with low APIs occurred, the VWC decreased accordingly. This period affected the regression significantly as the VWC kept decreasing while the API values only decreased slightly or remained at API= 0 mm. For this reason, days with values of API decreasing below 0.3 mm were discarded from the analysis.

The periods highlighted in blue in Figures 6.3 to 6.5 represented the intervals when the soil became frozen, and the sensors could no longer detect the water in the soil. These periods were determined using the soil temperatures measured by the sensors to define when the temperature dropped to zero in each location and water started to freeze.

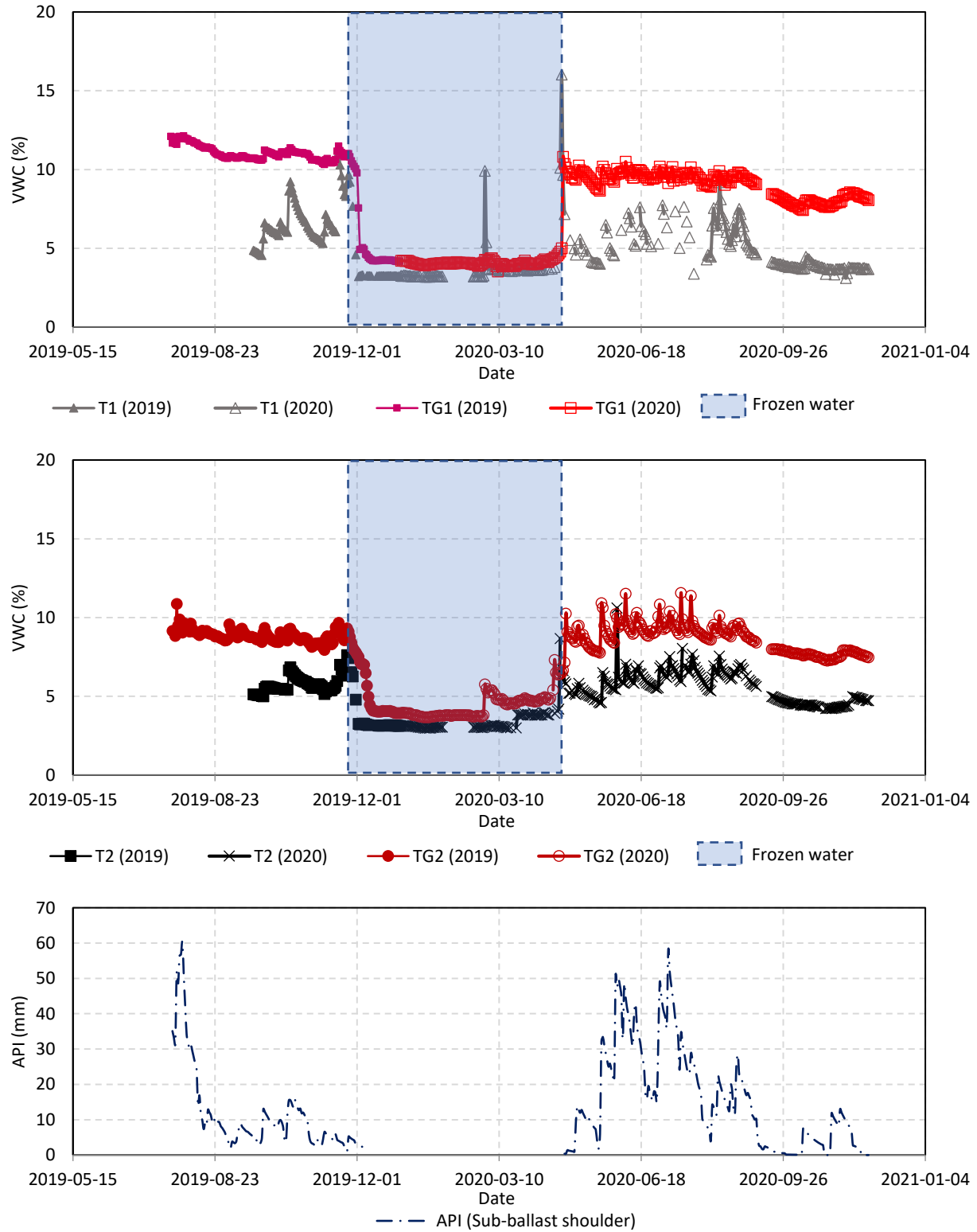


Figure 6.3. VWC measurements comparison with antecedent precipitation index values found for Sub-ballast shoulder.

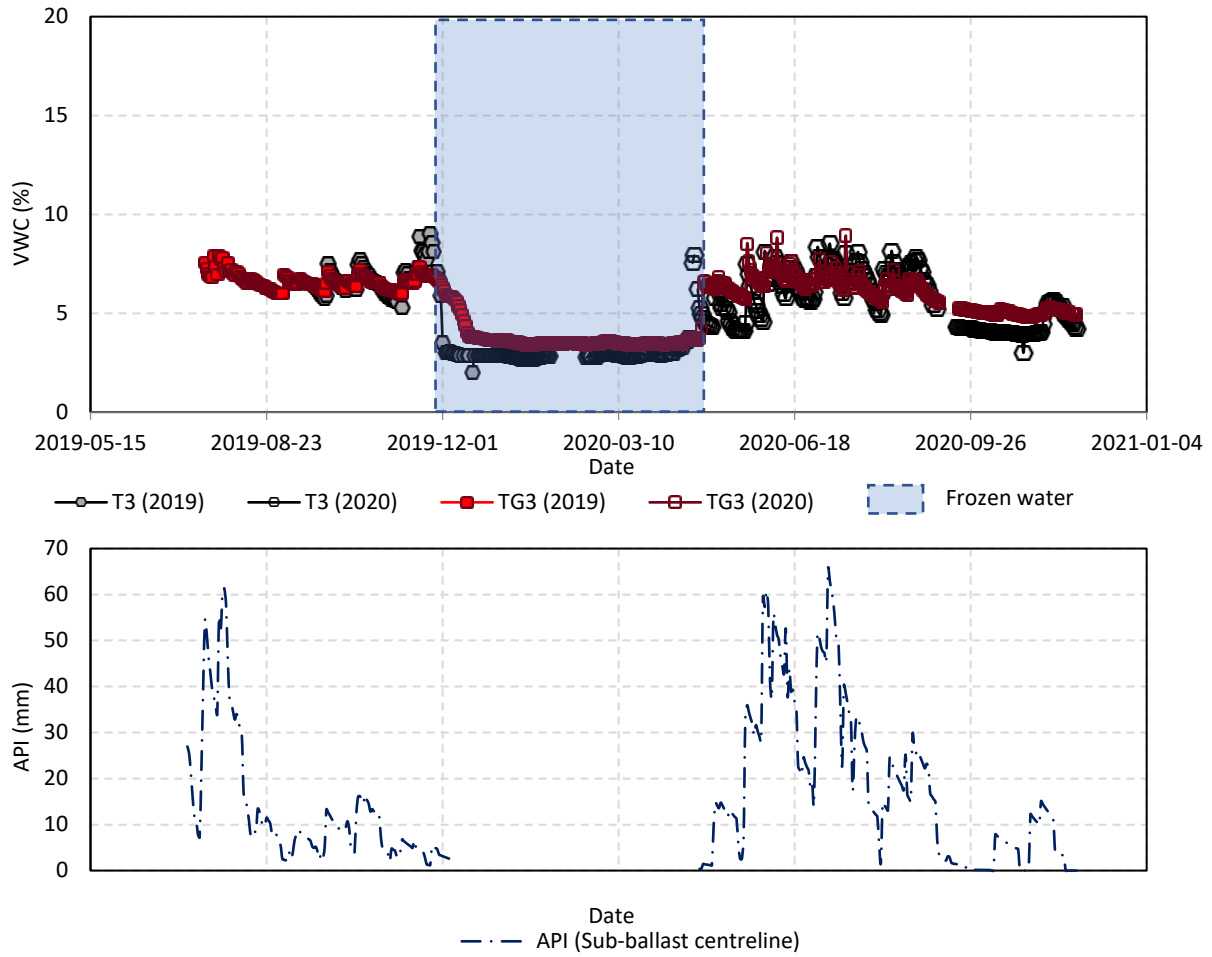


Figure 6.4. VWC measurements comparison with antecedent precipitation index values found for Sub-ballast centreline.

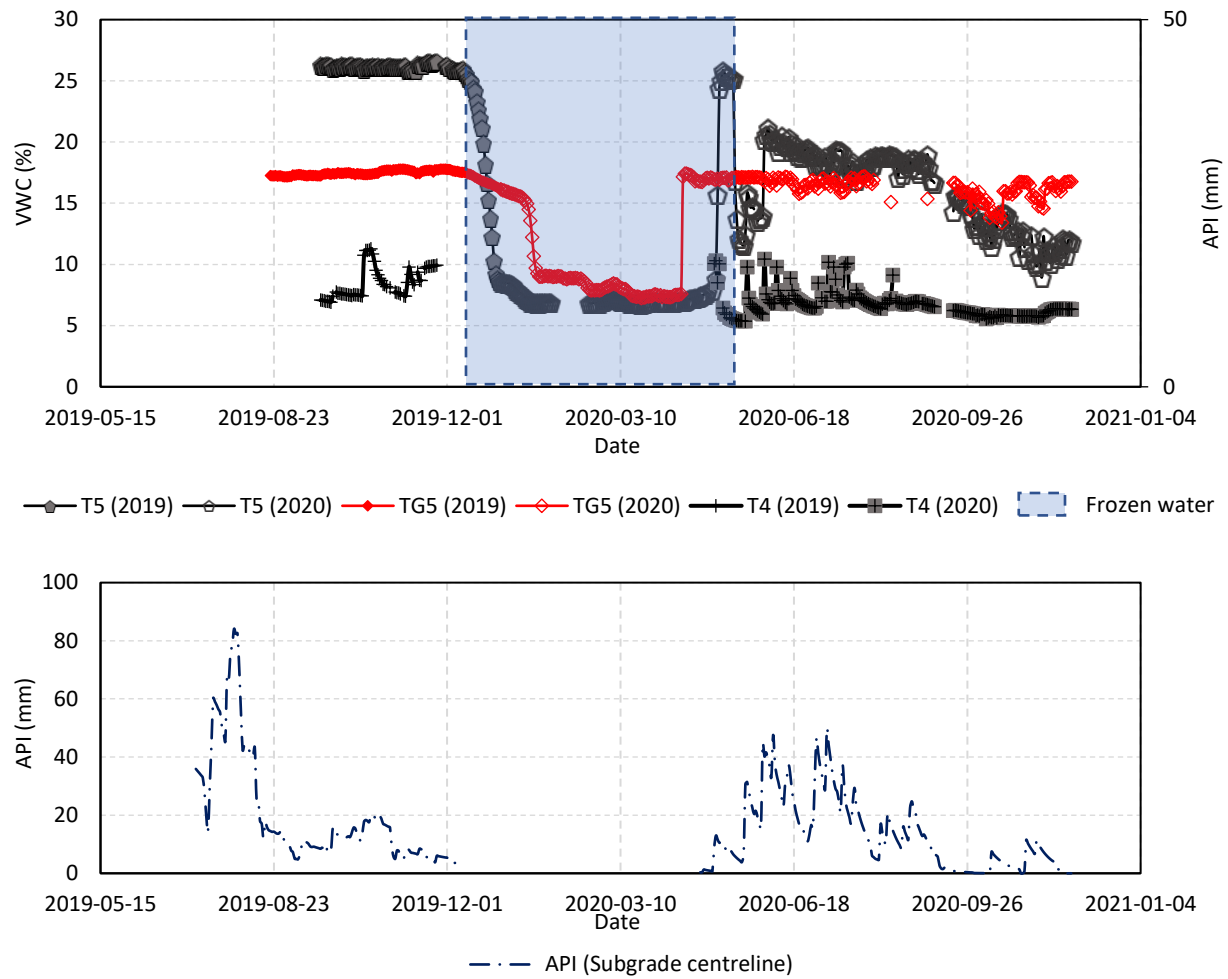


Figure 6.5. VWC measurements comparison with antecedent precipitation index values found for a) Sub-ballast shoulder, b) Sub-ballast centreline, and c) Subgrade centreline.

Figure 6.6 shows the curve-fitting performed for the VWC data from 2019. None of the sections had enough data to bring a high confidence level in the results for 2019. The variability of the data collected in 2019 for the control section potentially causes the low R^2 exhibited by the control section. The control section had data collected only for September-November (42 days), while the remediated section comprised data from July-November (73 days), except for TG5. This sensor only presented data from August-November (59 days) due to issues with the datalogger data collection.

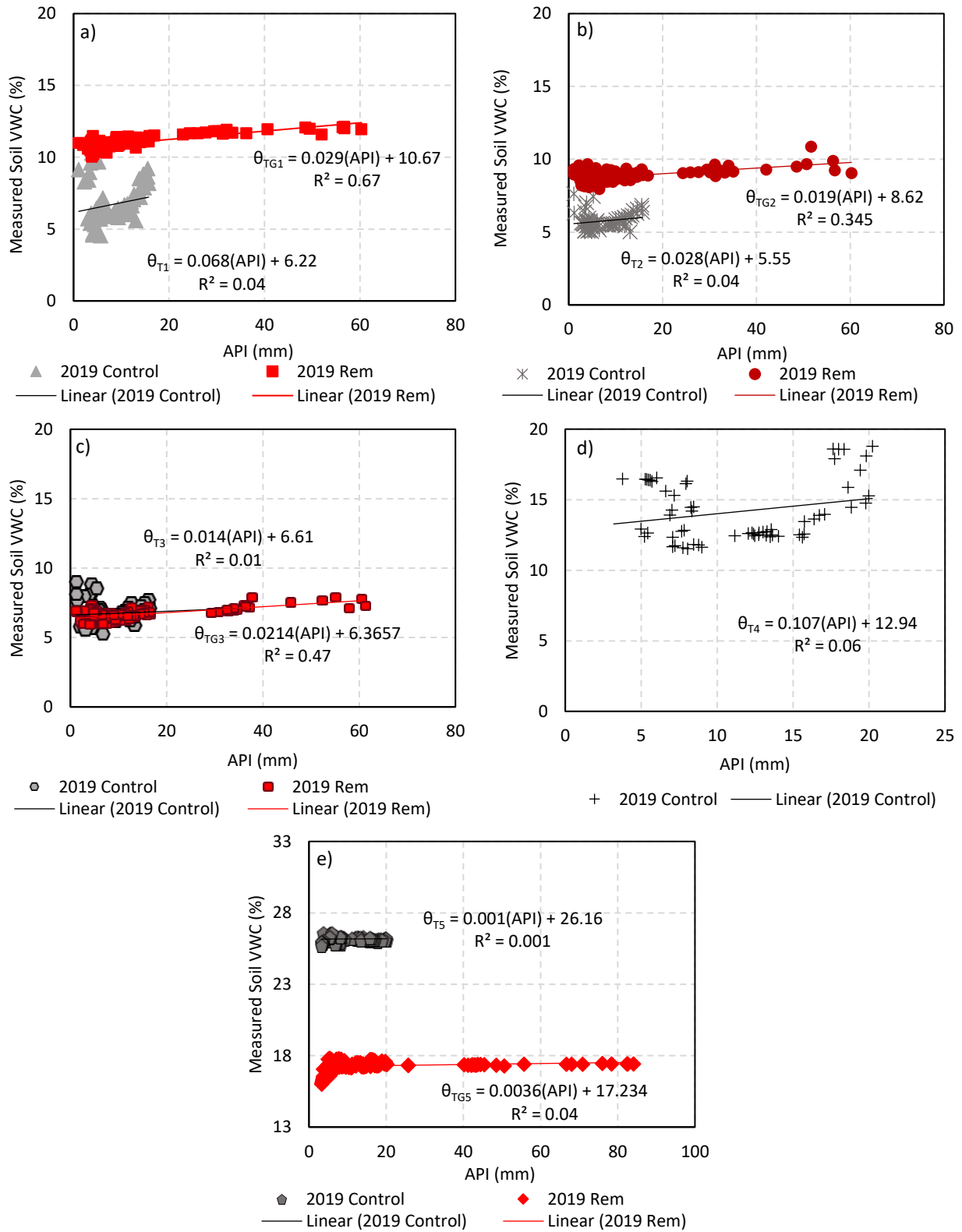


Figure 6.6. Linear regression of daily measured VWC vs. API for the year 2019. a) T1 and TG1 (Sub-ballast shoulder), b) T2 and TG2 (Sub-ballast shoulder), c) T3 and TG3 (Sub-ballast centreline) and d) T4 (Subgrade centreline) and e) T5 and TG5 (Subgrade centreline).

In 2020, a whole year cycle of data was available, making it possible to observe a VWC vs. API relationship pattern for all sensors. The analysis displayed a minimum confidence level of 80% that the VWC value is within $\pm 3\%$ of the measured value.

The data returned moderate to strong correlations for the sub-ballast sensors in 2020, based on the R^2 values found for the regressions (Figure 6.7); therefore, it is confirmed that the precipitation history influences the moisture of the embankment significantly, even though this influence gets lower as larger depths are reached. The subgrade material did not present a strong correlation with precipitation in any section, but this characteristic may be attributed to its low permeability and greater depth than the sub-ballast layer.

In Figures 6.6 and 6.7, the coefficient α of the fitting curve represents the variation of moisture with API. It is visible that the sub-ballast shoulder of the remediated section maintained an overall low change in moisture as precipitation events occurred, even though the VWC found in this section was higher than the control section values throughout the study (Figure 6.7(a) and (b)). The sub-ballast centreline also maintained a slightly lower moisture variation at the remediated section despite presenting the same VWC levels seen at the control section (Figure 6.7(c)).

Figure 6.7(d) and (e) present the data for the subgrade centreline sensors. The control section sensors presented “outlier” clusters of data (indicated by circles in the Figures) attributed to different events. Sensor T4 (Figure 6.7(d)) presented a cluster with VWC levels higher than the usual, and these data points were associated with days with intense precipitation (>10 mm). Additionally, sensor T5 presented a cluster with VWC values lower than usual (Figure 6.7(e)). It was observed that this cluster represents the period after October 28, 2020; therefore, these smaller VWCs are associated with the wetting period that occurred after the interval without precipitations (October 9 – October 28, 2020).

The subgrade centreline has shown a considerably lower variation in VWC at the remediated section, with α presenting a value approximately 10x smaller than what is seen for the control section (Figure 6.7(e)). This piece of evidence confirms that decoupling of moisture and precipitation events could be occurring at this location as only a slight variation appears even with a high amount of precipitation occurring.

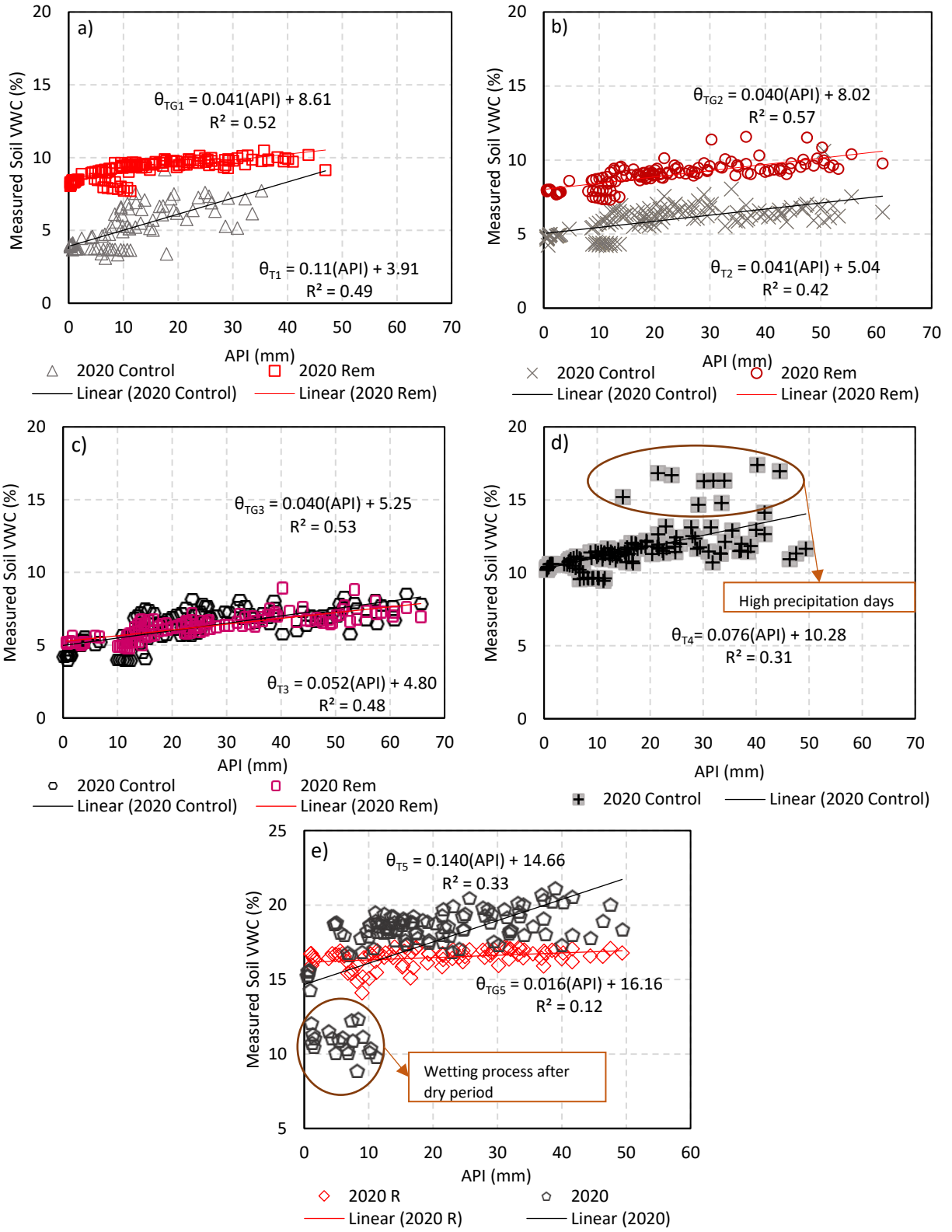


Figure 6.7- Linear regression of daily measured VWC vs. API for the year 2020. a) T1 and TG1 (Sub-ballast shoulder), b) T2 and TG2 (Sub-ballast shoulder), c) T3 and TG3 (Sub-ballast centreline) and d) T4 (Subgrade centreline) and e) T5 and TG5 (Subgrade centreline).

It was observed that during periods with $API < 10$ mm, all the control section sensors presented lower VWC levels than those from the remediated section (Figure 6.7). This observation reveals that the remediation does contribute to moisture release right after precipitation events, but the importance of dry periods on VWC changes was also lowered.

The study did not consider the remediation effects in a 3-D setting but rather 2-D. Given that the sections are adjacent, the convergence of VWC between the control and remediated sections at the end of 2020 might also be due to an internal transfer of moisture from the control to the remediated subgrade caused by a hydraulic gradient within the layer.

6.3 Soil Shear Strength Analysis

In unsaturated conditions, higher suction values lead to an increase in the shear strength and an improvement in the bearing capacity of the material (Alvarenga et al. 2020). Therefore, the drainage improvement brought by the track reconstruction could potentially bring positive effects regarding the strength of the embankment materials.

The sub-ballast material presented very high suctions as the VWC levels seen in-situ for this layer were close to or beyond the residual value found in the SWCC. Therefore, only the subgrade unsaturated strength was analyzed. The in-situ estimated suction for the deepest sensors in the subgrade material of both sections is presented in Figure 6.8.

As a means to understand the impact of the reconstruction on the soil strength, it was required to delineate the relationship between the moisture and the strength of the materials. The information available for estimating the in-situ unsaturated strengths were the VWC measurements and the results from both SWCC and DS tests performed in the laboratory.

The strength prediction method outlined in Section 2.3.1 was used to estimate the in-situ strength of the materials. In order to determine the overburden stress, the in-situ density of the ballast and sub-ballast were defined based on the values presented by Ebrahimi et al. (2012); the in-situ density determined at the field was used for the subgrade.

The average depth between sensors T5 (0.80 m) and TG5 (1.07 m) was used to compare the strength levels of both sections. The estimated overburden stress was then used in conjunction with the daily matric suction values to determine the unsaturated shear strength of the materials at the

average depth (0.93 m). Figure 6.9 presents the estimated in-situ strength values for the subgrade at both remediated and control sections.

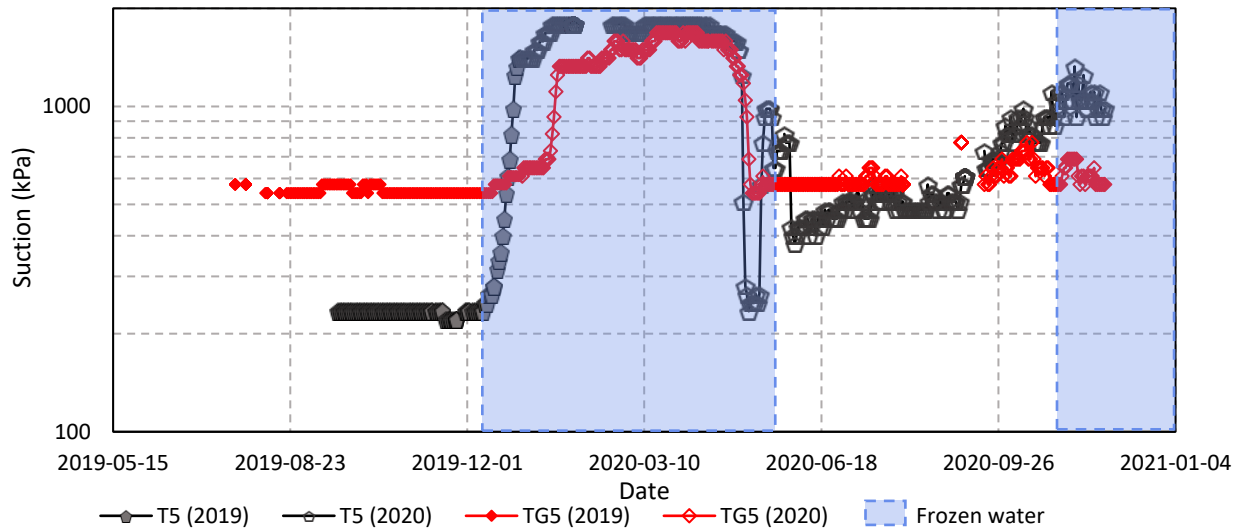


Figure 6.8. Estimated in-situ suction values for the subgrade centreline at the control section (T5) and remediated section (TG5).

In Figure 6.9, it is possible to see that the remediated section had its strength concentrated between 90-97 kPa. This narrow range could be attributed to the VWC maintaining overall constant levels at this section. However, the control section presented an extensive range of strength levels, with its minimum strength being around 71.5 kPa. This section has also presented a slightly larger maximum strength level (101 kPa) as it occasionally reached lower VWCs.

The remediated section presented strength levels higher than the control section before the spring-thaw of 2020 (Figure 6.9). After defrosting, the remediated section maintained higher strength levels than the control section for most of 2020, but the convergence of the VWC levels seen for the remediated and control sections after the dry period promoted a convergence of the estimated soil strength. In the last months of the analysis (October- November 2020), the control section sensors presented high strength values associated with the VWC response to the dry period seen in October. Data analysis from another spring-thaw is desirable to see how these sections behave under a more common precipitation regimen.

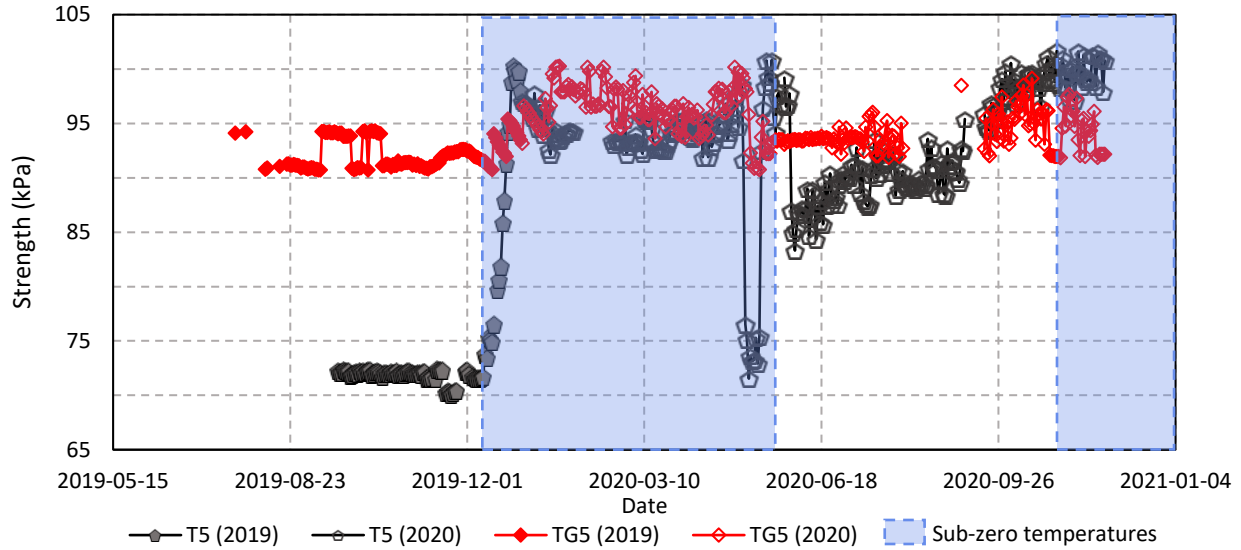


Figure 6.9- Variation of in-situ strength values at the subgrade (93 cm depth) through the time of the study for control section (T5) and remediated section (TG5).

6.4 Comparison of In-situ VWC Levels and their Variation with Precipitation

The remediated sub-ballast shoulder presented higher VWC (9%) than the control section sub-ballast shoulder (6%). Both sections displayed a VWC of around 6% for the sub-ballast centreline. The lower or similar values of VWC at the sub-ballast centreline compared to the shoulder indicate that water pooling did not occur at the sub-ballast centreline.

There were many sharp increases in VWC throughout the study attributed to rainfall events; however, not all VWC increases matched the rainfall data. For example, data from 12/08/2020 showed a slight increase in the VWC for all sensors even though no precipitation events were registered at the weather stations. This behaviour might be caused by local rainfall events occurring in the test site that did not cover the weather station from which precipitation data was collected. The same behaviour was identified by Zhang and Galinmoghadam (2020) as they also used weather station data for their study.

Table 6.3 summarizes the variations of VWC vs. API found for each sensor/location for a direct comparison between sections. The quantification of VWC variation with API was based on values of coefficient α . The remediated section VWC variations were around 0.37-1.02x the variation seen in the control section at the sub-ballast shoulder. For the sub-ballast centreline, the remediated section variation was around 0.8x of the control section.

The period without precipitation greatly affected the coefficient found for T5 (control section, subgrade), as a cluster was formed when rainfall events returned in November/2020 (Figure 6.7(e)). For this reason, the effect of the remediation was divided into two perspectives in Table 6.3: one considering the wetting period after October/2020 and another one excluding this cluster. Even when removing the wetting period cluster, it became evident that the remediation benefited the drainage of the track by decreasing the VWC variation coefficient by at least 49%.

Table 6.3. Summary of variation of VWC within sections for direct comparison.

Sensor Location	Sensor #	Coefficient α		Percentage of relative variation of VWC (Rem./Control Section)
		Control Section	Remediated Section	
Sub-ballast Shoulder	1	0.110	0.041	37%
	2	0.041	0.042	102%
Sub-ballast Centreline	3	0.052	0.040	77%
Subgrade Centreline (*including wetting period cluster)	4	0.076	-	-
	5	0.143	0.016	11%
Subgrade Centreline (*excluding wetting period cluster)	4	0.076	-	-
	5	0.031	0.016	51%

Another important observation is that all sensors of the remediated sub-ballast presented a similar VWC variation with API, therefore indicating that the remediation may have worked towards the homogenization of the moisture variation within this layer.

The sensors installed at the control subgrade presented peaks in VWC when precipitation occurred, implying that precipitation does impact the moisture of this layer, and the importance of precipitation on the VWC lowers as the depth from the subgrade surface increases.

When low APIs were present, the remediated section displayed a smaller VWC decrease than the control section. However, the period without precipitation in 2020 is not usual on a typical precipitation profile and may have influenced the results. Moreover, the remediated section did not show increases in the subgrade moisture after intense precipitation events, a trend that was not followed by the control section. Since water accumulation is one of the leading causes of the mentioned issues found at the site, the remediation seems to be improving the moisture release after precipitation events, therefore lowering the influence of precipitation events on the moisture changes at the subgrade material.

One important observation that when comparing α found for sensors T1, TG1, and TG2 with the α found for T2 (Table 6.3), it is possible to observe that T2 presented a value closer to the remediated section sensors (TG1 and TG2). After observing the position of the access pipes in the field, it was found out that sensor T2 is the closest to the remediated section and may be within the distance affected by the remediation due to a hydraulic gradient effect.

6.5 Contribution of VWC on Subgrade Strength

Until October 2020, the remediated section presented an improvement in the strength levels compared to the control section. Since the remediated section did not present considerable increases in VWC during high precipitation events, this section has maintained overall better strength levels, with its lower bound being 19 kPa higher than the control section's lowest strength.

Despite not having reached the highest strength seen for the soil (100 kPa), the remediated section showed only strength levels above 90 kPa during the entire study, while the control section frequently showed days with a soil strength within 72-85 kPa. Moreover, the control section presented high strength values only after October/2020 due to the extended period without precipitation events, i.e., the estimated strength for the control section could be different in a more common precipitation regimen.

Sattler et al. (1990) mentioned that including the matric suction into the track design brings significant differences when estimating the bearing capacity of the track embankment. Therefore, having a high lower bound for the suction values brings benefits to the track stability and safety factor, increasing bearing capacity and possibly mitigating problems such as cess heave and the onset of ballast pockets.

6.6 Comparison of Reconstruction Effect with Previous Studies Using Wicking Geotextile

The data analysis suggests that the reconstruction helped with water removal after a rainfall until the soil returned to its initial moisture. This observation is similar to the one made by Wang et al. (2017) in their laboratory tests using the wicking geotextile. This convergence of VWC to the initial value seen for the remediated section on high precipitation days indicates that the remediated site may be benefiting from the inclusion of the wicking geotextile.

Zornberg et al. (2017) indicated that the section remediated with Mirafi® H2Ri presented a narrower range in the VWC variation than the remediation using other geotextiles. Therefore, the

consistent values of VWC at the remediated subgrade may also be linked to a homogenization of the moisture brought by both the water redistribution feature of the wicking geotextile and the use of a homogeneous material for the sub-ballast.

Lima et al. (2017) mention that capillary barriers are structures that impede water flow due to the presence of capillary forces between a material with large pores and an unsaturated soil. When in contact with fine-grained soil, a geotextile can function as a capillary barrier and limit water flow either upwards or downwards. Azevedo & Zornberg (2013) mentioned that even though the lateral drainage function provided by the wicking fibers in Mirafi® H2Ri can minimize the moisture buildup after a capillary barrier was formed, a capillary barrier still developed. The presence of a capillary barrier between the subgrade and the geotextile sheet could explain the less pronounced effect that the dry period had on the remediated subgrade (sensor TG5) compared to the control section (sensor T5).

Several studies (Zhang and Galinmoghadam, 2020; Zornberg et al. 2017; Zhang and Connor, 2015) mentioned that water removal could significantly improve by exposing the end of the wicking geotextile to the atmosphere. The principle of the geotextile is based on the existence of a hydraulic gradient between the soil and relative humidity in the atmosphere. This hydraulic gradient then induces water removal by capillary effects. Zhang and Galinmoghadam (2020) also mentioned that one of their remediated sections presented a VWC slightly higher than the control section while the end of the geotextile was covered by soil. After the edge of the wicking geotextile was exposed, the VWC of this section started to deviate from the control section and performed better in terms of drainage.

Tencate (2020) also mentions that the most effective installations are daylighting or bio-wicking, where the first counts with at least 30.5 cm (12”) of the geotextile being exposed at the end. This exposed part could be protected or not by small riprap stones. Bio-wicking relies on local vegetation to draw water from the system through their roots, away from the exposed edge hidden beneath the vegetation. Therefore, to increase the geotextile water removal performance, its edges could be exposed by at least 30.5 cm at the remediated section.

7. CONCLUSIONS AND RECOMMENDATIONS

This research had the purpose of understanding the benefits of the reconstruction using a wicking geotextile regarding the drainage performance of a low-permeability subgrade and its possible benefits to the strength of the material. The study consisted of carrying a series of material characterization tests and using a test site northeast of Edmonton, Alberta, at the Scotford subdivision. The use of adjacent sites allowed a direct comparison of the performance of the reconstructed site to a common setup. The key findings and conclusions of the first year of monitoring are as following:

- The effect of the wicking geotextile cannot be separated from the effect of the clean materials used in the reconstruction by only using the field data. Further research is required to achieve this goal.
- The readings from 5TE sensors were chosen for the analysis rather than the Diviner 2000 measurements due to the higher frequency of data collection and better repeatability of readings.
- The remediated section presented higher recorded VWC values in the sub-ballast shoulder compared to those found for the control section, even though the variations in VWC were similar or lower. A series of factors may lead to this difference, and further research must be performed to understand the mechanism beneath it.
- The VWC read by all sensors at the sub-ballast presented peaks coinciding with peaks in precipitation, and one sensor installed close to the surface of the subgrade (T4) also presented many peaks with precipitation. These peaks in VWC coinciding with precipitation events confirmed that precipitation is the primary source of moisture within the embankment and the subgrade surface.
- Sensor T5 (subgrade, control section) has shown slight peaks in VWC with precipitation, while sensor TG5 (subgrade, remediated section) has shown little to no disturbance in its VWC even on days of high precipitation. This behaviour indicates that the remediation improved drainage after precipitation events.
- During a dry period of 33 days in September/October 2020, all sensors installed at the subgrade presented a decrease in VWC due to the lack of a water source. Sensor T5 (control section) was the most affected, presenting a considerable decrease in its VWC. The

presence of a capillary break between the wicking geotextile and the subgrade interface is believed to be responsible for the lower impact of this period on the remediated subgrade (sensor TG5).

- The decrease in VWC for sensor T5 during the dry period affected the analysis using the Antecedent Precipitation Model and the curve-fitting. For this reason, an analysis was also performed without considering the wetting period that occurred after October 2020.
- The remediated section presented lower VWC variations (lower α) than the control section relative to API in all situations, i.e., this section tends to be less sensitive to precipitation events. This aspect may be attributed to a faster moisture release in the remediated section right after a precipitation event. Therefore, the remediation improved the drainage of the track embankment.
- All remediated section sensors installed at the sub-ballast presented a similar variation of VWC with API, evidencing that homogenization of the variation in moisture may also be one of the benefits brought by the reconstruction.
- Sensor T2 (sub-ballast shoulder, control section), which was the closest to the remediated section, presented a variation in VWC similar to those found for sensors TG1 and TG2 (sub-ballast shoulder, remediated section). This behaviour may indicate that the remediation may influence the VWC of an area larger than the one in which it was done due to a hydraulic gradient brought by the local reconstruction.
- The suction values found for the sub-ballast showed that this material is close to dry conditions at both remediated and control sections. Therefore, the remediation did not bring an impact on its strength.
- The subgrade strength has maintained consistent levels at the remediated section with values around 94 kPa, while the control section presented subgrade strength values varying between 70-100 kPa. It was observed that the control section only reached high strength levels after an unusually long period without precipitation in October 2020. Therefore, it is possible to conclude that the remediation also improved the subgrade strength levels.
- The issues present at the site are mostly related to the increases in the subgrade moisture with precipitation and consequent decrease in soil strength. The remediation could be a good alternative for mitigating these problems.

This study addressed solely the improvement in drainage and strength brought by the reconstruction and the wicking properties of Mirafi® H2Ri. It did not consider the other possible benefits of Mirafi® RS580i and Mirafi® H2Ri, including reinforcement, stress redistribution, frost heave mitigation, separation, and filtration. The reconstruction was able to enhance the track lateral drainage by decreasing the impact of precipitation events on the soil VWC.

The reconstruction led to the decoupling of the moisture at the subgrade from precipitation events. Since the monitoring was performed only for one-year cycle, it is fair to say these conclusions were based on limited data and further analysis is desirable.

The chosen installation method for the wicking geotextile is recommended by Tencate (2020) to redistribute water within the embankment. This method could improve the subgrade strength variability along the treated area and, therefore, mitigate issues such as the formation of ballast pockets. This characteristic, however, was not assessed in this study.

7.1 Recommendations for Future Research

Since there was an unusually long period without precipitation in 2020 and a precipitation deficit was seen according to historical data, the moisture analysis could be affected by this period. Continued monitoring is recommended in order to compare both sections in a year with a typical precipitation regimen. Moreover, the track reconstruction is relatively recent, and the data is only enough to analyze one freeze-thaw cycle. Therefore, continued monitoring would also help with understanding the long-term effects of the reconstruction on the moisture and strength levels and its impacts on the long-term issues found at the site. A more complex model involving more environmental conditions such as soil temperature, air temperature, wind speed, and relative humidity may also be developed using software to understand what other aspects influence soil moisture.

The manufacturer mentions that the most effective installations of the wicking geotextile are daylighting or bio-wicking, where the first counts with at least 30.5 cm (12”) of the geotextile being exposed at the end. Consequently, it would be recommended to expose the end of the wicking geotextile at the site to verify how this method improves the drainage performance of the embankment compared to the method used in this study.

The Diviner 2000 readings were not used in the analysis due to the high data variability and lack of 5TE sensors at the subgrade for comparison. It also presented a limited quantity of readings. The calibration seemed to help with the correlation 5TE-Diviner 2000; however, it is recommended that the calibration is redone for both sub-ballast and subgrade soils, with further analysis being performed considering the readings from the Diviner probe.

Either numerical modeling or large-scale laboratory tests can also be performed to separate the effect of the remediation with cleaner materials from the effect of the wicking geotextile in the track drainage performance by simulating rainfall.

Large-scale laboratory tests could also lead to a broader understanding of the contributions brought by the geotextiles incorporated into the reconstruction besides the drainage performance. For example, along with the drainage improvement, the stress redistribution and its effects on the track settlement could be quantified using pressure cells and strain gauges in the large-scale tests. These tests may include a simulation without geotextiles, one simulation including both geotextiles, and the last simulation only using the wicking geotextile at the subgrade surface. The inclusion of site instrumentation such as accelerometers for monitoring track settlement and numerical modeling may also help clarify the contributions of the reinforcement on other aspects of the track. Additionally, some factors may have led the remediated section track centreline to show slightly higher moisture contents in periods with low API than the control section centreline. These include the possibility of a capillary barrier formation at the sub-ballast-geotextile interface or the homogenization of moisture within the remediation promoted by the wicking geotextile. Therefore, it would be interesting to explore these factors to understand the mechanisms behind this condition.

Frost heave and clay pumping were also cited as an issue on the track; therefore, it is important to comprehend the effect of the remediation on frost heave and clay pumping activity. Moreover, the use of track geometry measurement systems may also help with understanding the effects of the inclusion of the geotextiles on the track degradation in a long-term situation.

Zornberg et al. (2017) mentioned that the moisture content at State Highway 21, Texas remained relatively uniform over time and across the entire width of the road shoulder where Mirafi® H2Ri was installed. The sections treated with other geotextiles, however, presented non-uniform moisture contents. Since the wicking geotextile has the function of water redistribution, it would

also be interesting to use a series of moisture sensors within both control and remediated sections at different locations to observe how the VWC varies within these locations. Then, the effects of the remediation on the track moisture heterogeneity and differential settlement could be assessed.

REFERENCES

Abdulnabi, A. (2018). *Prediction of Rainfall Runoff in Geoenvironmental Engineering Practice* (Published doctoral dissertation). University of Alberta. DOI:

<https://doi.org/10.7939/R30P0X66H>

Alvarenga, C., Haji Abdulzaragh, P., Hendry, M. T. (2020). Monitoring of the change of moisture beneath a railway embankment and the effectiveness of a wicking geotextile. Proceedings of the 73rd CGS Conference, GeoVirtual 2020, Calgary, September 14, 2020.

ASTM D 7928-17 (2017). "Standard Test Method for Particle-Size Distribution (Gradation) of Fine-Grained Soils Using the Sedimentation (Hydrometer) Analysis". ASTM International, West Conshohocken, PA, USA

ASTM D1556 / D1556M - 15e1 Standard Test Method for Density and Unit Weight of Soil in Place by Sand-Cone Method

ASTM D2216-10 (2010). "Standard Test Methods for Laboratory Determination of Water (Moisture) Content of Soil and Rock by Mass." *Annual Book of ASTM Standards*, Vol. 04.08, ASTM International, West Conshohocken, PA

ASTM D4318-17 (2017). "Standard Test Methods for Liquid Limit, Plastic Limit and Plasticity Index of Soils." *Annual Book of ASTM Standards*, Vol. 4.08, ASTM International, West Conshohocken, PA.

ASTM D6836-16 (2008). "Standard test methods for determination of the soil-water characteristic curve for desorption using a hanging column, pressure extractor, chilled mirror hygrometer, and/or centrifuge".

ASTM D6913/D6913M-17 (2017). "Standard Test Methods for Particle-Size Distribution (Gradation) of Soils Using Sieve Analysis." *Annual Book of ASTM Standards*, Vol. 4.09, ASTM International, West Conshohocken, PA.

ASTM D854-06 (2007). "Standard Test Method for Specific Gravity of Soil Solids by Water Pycnometer." *Annual Book of ASTM Standards*, Vol. 04.02, ASTM International, West Conshohocken, PA

ASTM, D3080. (2011). "Standard test method for direct shear test of soils under consolidated drained conditions".

Azevedo, M., & Zornberg, J. G. (2013). Capillary barrier dissipation by new wicking geotextile. In *Panamerican Conference on Unsaturated Soils*, Cartagena de Indias, Colombia, pp. 559-565.

Baier, W., & Robertson, G. W. (1966). A New Versatile Soil Moisture Budget. *Canadian Journal of Plant Science*, 46(3), 299-315. doi:10.4141/cjps66-049

Bradley, A. H., Thiam, P., Drummond, S., Murchison, P., & Laprade, R. (2017). Incorporating a new wicking geotextile in northern, low volume highways to mitigate pavement edge cracking.

In *TAC 2017: Investing in Transportation: Building Canada's Economy--2017 Conference and Exhibition of the Transportation Association of Canada*.

Bulut, B., Yilmaz, M., Afshar, M. H. & Şorman, Ü., Yucel, I., Cosh, M. & Şimşek, Osman. (2019). Evaluation of Remotely-Sensed and Model-Based Soil Moisture Products According to Different Soil Type, Vegetation Cover and Climate Regime Using Station-Based Observations over Turkey. *Remote Sensing*. 11. 1875. 10.3390/rs11161875.

Canadian Pacific Railway (2020). *Transload & trucking*. Retrieved October 19, 2020, from <https://www.cpr.ca/en/choose-rail/transload-trucking>.

Clifton Associates (2019). *Grade Stabilization - Scotford Subdivision* (Rep. No. CG3204). Calgary, AB.

Das, Braja M. (2007). *Principles of Foundation Engineering, 7th Edition*. Stamford: Cengage Learning.

Ebrahimi, A., Tinjum, J. M., & Edil, T. B. (2012). Protocol for testing fouled railway ballast in large-scale cyclic triaxial equipment. *Geotechnical Testing Journal*, 35(5), 796-804.

Environment and Climate Change Canada (ECCC) (2020). *Historical Data: 2008-2018*. Accessed April 09, 2020, from https://climate.weather.gc.ca/historical_data/search_historic_data_e.html.

Fredlund, D. G. (2006). Unsaturated Soil Mechanics in Engineering Practice. *Journal Of Geotechnical and Geoenvironmental Engineering*, 132(3), 286-321.

Fredlund, D. G., & Houston, S. L. (2013). Interpretation of soil-water characteristic curves when volume change occurs as soil suction is changed. *Advances in unsaturated soils*, 1, 15.

Fredlund, D. G., & Morgenstern, N. R. (1978). Stress state variables for unsaturated soils. *Journal of Geotechnical and Geoenvironmental Engineering*, 103(ASCE 12919).

Fredlund, D. G., and Xing, A. (1994). Equations for the soil-water characteristic curve. *Canadian Geotechnical Journal*, 31(4), 521-532.

Fredlund, D. G., Rahardjo, H., & Fredlund, M. D. (2012). *Unsaturated Soil Mechanics in Engineering Practice*. Hoboken, NJ: Wiley. doi:10.1002/9781118280492

Fredlund, D. G., Vu, H. Q., & Stianson, J. (2010). Engineering protocols for the assessment of the net moisture flux at the ground surface. *Geotechnical Engineering*, 41(1), 193.

Geosynthetic Institute (2019). *Exposed Lifetime Prediction of Geosynthetics Using Laboratory Weathering Devices*. Retrieved January 06, 2021, from <https://geosynthetic-institute.org/grispecs/g20.pdf>

Google Earth. (2020). [Scotford Subdivision Sites]. Retrieved October 21, 2020, from <https://earth.google.com/web/>

Google Earth. (n.d.). [Location of Weather Stations]. Retrieved October 21, 2020, from <https://earth.google.com/web/>

Gui, M., & Yu, C. (2008). Rate of strength increase of unsaturated lateritic soil. *Canadian Geotechnical Journal*, 45(9), 1335-1343. doi:10.1139/T08-065

Guo, J., Wang, F., Zhang, X., & Han, J. (2017). Quantifying water removal rate of a wicking geotextile under controlled temperature and relative humidity. *Journal of Materials in Civil Engineering*, 29(1), 04016181.

Hayashi, M., Mohammed, G. A., Harrer, K., & Farrow, C. R. (2012). *Performance evaluation and improvement of the Versatile Soil Moisture Budget (VSMB) model*. University of Calgary, Calgary, AB.

Hendry, M., Onwude, L., & Segoo, D. (2016). A laboratory investigation of the frost heave susceptibility of fine-grained soil generated from the abrasion of a diorite aggregate. *Cold Regions Science and Technology*, 123, 91-98. doi:10.1016/j.coldregions.2015.11.016

Ho, D. Y., & Fredlund, D. G. (1982). A multistage triaxial test for unsaturated soils. (1/2), 18-25.

Hoskin Scientific Ltd. (n.d.). *ECH2O 5TE soil moisture sensor*. Retrieved March 12, 2021, from http://www.hoskin.ca/catalog/index.php?main_page=product_info&cPath=1_59_71_201&products_id=285&zenid=mej7662t1djic0rjkmf6krk2t1

Hosseini, S. M. R., Naeini, S. A., & Hassanlourad, M. (2017). Monotonic, cyclic and post-cyclic behaviour of an unsaturated clayey soil. *International Journal of Geotechnical Engineering*, 11(3), 225-235. doi:10.1080/19386362.2016.1210868

Indraratna, B., & Salim, W. (2005). *Mechanics of ballasted rail tracks: a geotechnical perspective*. CRC Press.

Indraratna, B., Nimbalkar, S., & Rujikiatkamjorn, C. (2012). Stabilising railway embankments with geosynthetic grids and drains and a class A prediction of track behaviour. Accessed June 19, 2019, from <https://pdfs.semanticscholar.org/c2a2/d3b7644a45c4cddf98f79f85c803f2644857.pdf>.

Indraratna, B., Salim, W., & Rujikiatkamjorn, C. (2011). *Advanced rail geotechnology-ballasted track*. CRC press.

Jong, D. T., Bosscher, P. J., & Benson, C. H. (1998). Field assessment of changes in pavement moduli caused by freezing and thawing. *Transportation Research Record*, 1615(1), 41-48.

Lima, M. J., Azevedo, M. M., Zornberg, J. G., & Palmeira, E. M. (2017). Capillary barriers incorporating non-woven geotextiles. *Environmental Geotechnics*, 5(3), 168-175.

Kohler, M. A., Linsley, R. K. (1951). Variations in storm rainfall over small areas. *Transactions, American Geophysical Union*, 32(2), 245. doi:10.1029/tr032i002p00245

Konrad, J. (1999). Frost susceptibility related to soil index properties. *Canadian Geotechnical Journal*, 36(3): 403-417.

- Leishman, E. M., Hendry, M. T., & Martin, C. D. (2017). Canadian main track derailment trends, 2001 to 2014. *Canadian Journal of Civil Engineering*, 44(11), 927-934.
- Li, D., & Selig, E. T. (1995). Evaluation of railway subgrade problems. *Transportation Research Record*, 1489, 17.
- Li, D., Sussmann, T. R., and Selig, E. T. (1996). *Procedure for Railway Track Granular Layer Thickness Determination*. Association of American Railroads, Report Number R-898.
- Li, D., Sussmann, T. R., Hyslip, J. P. & Chrismer, S. M. (2002). *Railway Geotechnics*. London: CRC Press. doi:10.1201/b18982
- Malekian, R., Gordon, R., Madani, A., & Robertson, S. (2014). Evaluation of the Versatile Soil Moisture Budget model for a humid region in Atlantic Canada. *Canadian Water Resources Journal / Revue Canadienne Des Ressources Hydriques*, 39(1), 73-82. doi:10.1080/07011784.2014.888891
- Meter Environment (2018). *Frequently Asked Questions*. Retrieved April 05, 2021, from <https://www.metergroup.com/environment/faqs/>
- Meter Environment (2019). *Method A: Soil-specific calibrations for METER soil moisture sensors*. Accessed May 29, 2019, from <https://www.metergroup.com/environment/articles/method-a-soil-specific-calibrations-for-meter-soil-moisture-sensors/>.
- Pickles, C. B., & Zornberg, J. G. (2012, May). Hydraulic classification of unsaturated nonwoven geotextiles for use in capillary barriers. In *Proceedings of GeoAmericas 2012, the second Pan-American Geosynthetics Conference* (pp. 1-4).
- Roustaei, M., Hendry, M.T. and Roghani, A. (2019). Frost susceptibility of subgrade soil beneath railway tracks: Case Study. *The 72nd Canadian Geotechnical Conference. St. John's, NF*, 29 Sep-2Oct.
- Rushton, K. R., & Ghataora, G. (2014, February). Design for efficient drainage of railway track foundations. In *Proceedings of the Institution of Civil Engineers-Transport* (Vol. 167, No. 1, pp. 3-14). Thomas Telford Ltd.
- Sahlour, F. (2015). Moisture influence on structural behaviour of pavements. *Doctoral Dissertation*.
- Sattler, K, Elwood, D, Hendry, MT, et al (2020a) "Open source software for data collection from SDI-12 sensors connected to an Arduino microcontroller", DOI: <https://doi.org/10.7939/r3-7y8z-dh16>.
- Sattler, K, Elwood, D, Berscheid, B, Hendry, MT, Abdulrazagh, P, Huntley, D (2020b) "Field application of inexpensive custom-build programmable dataloggers for routine instrumentation needs" In *Proceedings of the 73rd Canadian Geotechnical Conference*, Calgary, Canada, Sept 13-16
- Sattler, K, Elwood, D, Hendry, MT, et al (2021) "Field collection of geotechnical measurements for remote or low-cost datalogging requirements" *ASTM Geot Test J*, in press.

- Sattler, P., Fredlund, D. G., Lam, L. W., Clifton, A. W., & Klassen, M. J. (1990). Implementation of a bearing capacity design procedure for railway subgrades: A case study. *Transportation Research. Record*, 191-197.
- Selig, E. T., & Waters, J. M. (1994). *Track Geotechnology and Substructure Management*. Thomas Telford.
- Sentek Pty Ltd (1999). *Diviner 2000 User Guide Version 1.5*. City of Norwood Payneham & St Peters, SA. Australia. Accessed May 28, 2019, from <https://sentektechnologies.com/download/diviner-2000-user-guide/>.
- Tencate (2015). *Mirafi® H2Ri Woven Geosynthetic for improved Soil Stabilization and Base Course Reinforcement through Continuous Moisture Management*. Accessed April 30, 2019, <https://www.tencategeo.us/en-us/products/woven-geotextiles/mirafi-h2ri>.
- Tencate (2018). *Mirafi® RS580i*. Accessed April 30, 2019, <https://www.tencategeo.us/en-us/products/woven-geotextiles/mirafi-rsi-series>.
- Tencate (2020). *Installation Guidelines for Mirafi® H2Ri Moisture Management System*. Retrieved March 23, 2021, from https://www.tencategeo.us/media/0dcf4b31-c2bb-4844-9132-61b6a6fcb1a/CTkwZQ/TenCate%20Geosynthetics/Documents%20AMER/Installation%20Guidelines/Roadway%20and%20Railway%20Construction/IG_H2Ri%200520
- Tencate (n.d.). *The durability of geotextiles*. Retrieved January 06, 2021, from <https://www.tencategeo.us/media/50b6a456-96ab-4943-9985-a137c8ad43c3/U-y8rA/TenCate%20Geosynthetics/Documents%20AMER/Industry%20Papers/The%20durability%20of%20geotextiles.pdf>
- Trani, L. D. O., & Indraratna, B. (2010). Assessment of sub-ballast filtration under cyclic loading. *Journal of Geotechnical and Geoenvironmental Engineering*, 136(11), 1519-1528.
- Vanapalli, S. K., & Fredlund, D. G. (1999). Empirical procedures to predict the shear strength of unsaturated soils. In *Eleventh Asian regional conference on soil mechanics and geotechnical engineering* (pp. 93-96).
- Vanapalli, S. K., Fredlund, D. G., Pufahl, D. E., & Clifton, A. W. (1996). *Model for the prediction of shear strength with respect to soil suction*. *Canadian Geotechnical Journal*, 33(3), 379-392. doi:10.1139/t96-060
- Wang, F., Han, J., Zhang, X., & Guo, J. (2017). Laboratory tests to evaluate effectiveness of wicking geotextile in soil moisture reduction. *Geotextiles and Geomembranes*, 45(1), 8-13. <https://doi.org/10.1016/j.geotextmem.2016.08.002>.
- Xie, W. P., & Yang, J. S. (2013). Assessment of soil water content in field with antecedent precipitation index and groundwater depth in the Yangtze River Estuary. *Journal of Integrative Agriculture*, 12(4), 711-722. DOI: [https://doi.org/10.1016/S2095-3119\(13\)60289-0](https://doi.org/10.1016/S2095-3119(13)60289-0)

Zhang, X., & Connor, B. (2015). *Evaluate H2RI Wicking Fabric for Pavement Application - Year 2* (Rep. No. 2013-S-UAF-0026). Seattle, WA: PacTrans.

Zhang, X., & Galinmoghadam, J. (2020). *Performance of Wicking Geotextile on Mitigating Water Pumping Issue on I-44 Highway* (p. 0-64, Rep. No. CMR 20-003). Rolla, MO: Missouri University of Science and Technology.

Zhang, X., Presler, W., Li, L., Jones, D., & Odgers, B. (2014). Use of Wicking Fabric to Help Prevent Frost Boils in Alaskan Pavements. *Journal of Materials in Civil Engineering*. Retrieved November 18, 2020, from [https://ascelibrary.org/doi/10.1061/\(ASCE\)MT.1943-5533.0000828](https://ascelibrary.org/doi/10.1061/(ASCE)MT.1943-5533.0000828)

Zornberg, J. G., Azevedo, M., Sikkema, M., & Odgers, B. (2017). Geosynthetics with enhanced lateral drainage capabilities in roadway systems. *Transportation Geotechnics*, 12, 85-100. doi:10.1016/j.trgeo.2017.08.008

APPENDIX I – Material Characterization Results

- I.1 – Moisture Content Tests
- I.2 – Sieve Analyses
- I.3 – Atterberg Limits
- I.4 – Consolidated Direct Shear
- I.5 – SWCCs
- I.6 – Field Density Test

I.1 – Moisture Content Tests

Table I.1. Moisture content result for the Top Control Ballast sample.

Moisture Content Test	
Soil Location and Date	Ballast top before excavation - 23/04/2019
Soil description	Gravel. Great diameter did not pass 1 1/2'. Presence of pieces of wood from sleepers.
Container Number	BT01
Container Mass (g)	538.1
Initial Container + Moist Specimen Mass (g)	7744.7
Date/time in oven	May 2, 10:58
First Container + Dry Specimen Mass (g)	7633.9
Date/time in oven	May 2, 13:27
Secondary Container + Dry Specimen Mass (g)	7580.3
Date/time in oven	May 3, 08:42
Final Container + Dry Specimen Mass (g)	7580.3
Date/time in oven	May 3, 10:41
Mass of Water	164.4
Mass of Solids	7042.2
Water Content	2.33
Average moisture content	2.33

Table I.2. Moisture content result for the Bottom Control Ballast sample.

Moisture Content Test	
Soil Location and Date	Ballast bottom before excavation - 23/04/2019
Soil description	Gravel. Great diameter did not pass 1 1/2' sieve. Presence of fine materials around gravel. Presence of pieces of wood from sleepers
Container Number	BB01
Container Mass (g)	543.4
Initial Container + Moist Specimen Mass (g)	6204.6
Date/time in oven	May 2, 10:15
First Container + Dry Specimen Mass (g)	6098.5
Date/time in oven	May 2, 13:25
Secondary Container + Dry Specimen Mass (g)	6005.5
Date/time in oven	May 3, 08:38
Final Container + Dry Specimen Mass (g)	6005.1
Date/time in oven	May 3, 10:52
Mass of Water	199.5
Mass of Solids	5461.7
Water Content	3.65
Average moisture content	3.65

Table I.3. Moisture content result for the Control Subballast sample.

Moisture Content Test		
Soil Location and Date	Subballast before excavation - 23/04/2019	
Soil description	Material passed sieve 1 1/2". Brown, presence of fine-grained material and gravels.	
Container Number	SBB03	BT02
Container Mass (g)	46.9	48.2
Initial Container + Moist Specimen Mass (g)	5583.9	5970.4
Date/time in oven	May 2, 13:00	May 2, 15:13
First Container + Dry Specimen Mass (g)	5408.9	5751.3
Date/time in oven	May 2, 15:45	May 3, 10:55
Secondary Container + Dry Specimen Mass (g)	5346.5	5747
Date/time in oven	May 3, 8:48	May 4, 11:00
Final Container + Dry Specimen Mass (g)	5346.5	5746.3
Date/time in oven	May 3, 10:50	May 6, 8:40
Mass of Water	237.4	224.1
Mass of Solids	5299.6	5698.1
Water Content	4.48	3.93
Average moisture content	4.2	

Table I.4. Moisture content result for the Clean Ballast sample.

Moisture Content Test			
Soil Location and Date	Ballast after excavation - 24/04/2019		
Soil description	Gravel of great dimensions, did not pass any sieve.		
Container Number	SB02	SBB03	BA01
Container Mass (g)	46.6	47.7	529.3
Initial Container + Moist Specimen Mass (g)	5588.8	5512.9	6209.6
Date/time in oven	May 3, 12:10	May 3, 12:30	May 3, 13:33
First Container + Dry Specimen Mass (g)	5586.5	5510.8	6204.8
Date/time in oven	May 3, 15:56	May 3, 15:42	May 3, 15:45
Secondary Container + Dry Specimen Mass (g)	5578.7	5503.6	6197.8
Date/time in oven	May 3, 8:48	May 3, 8:30	May 3, 8:40
Final Container + Dry Specimen Mass (g)	5578.7	5501.3	6197.1
Date/time in oven	May 3, 10:50	May 3, 10:40	May 3, 10:46
Mass of Water	10.1	11.6	12.5
Mass of Solids	5532.1	5453.6	5667.8
Water Content	0.18	0.21	0.22
Average moisture content	0.2		

Table I.5. Moisture content result for the Clean Subballast sample.

Moisture Content Test			
Soil Location and Date	Subballast after excavation - 24/04/2019		
Soil description	Material passed 19 mm sieve. Brown, fine-grained material with the presence of small gravels.		
Sample #	10	4	2
Container Number	SB01	SB02	SB03
Container Mass (g)	550.9	46.99	4
Initial Container + Moist Specimen Mass (g)	3325.5	993.2	356
Date/time in oven	May 2, 10:30	May 2, 12:10	May 2, 12:39
First Container + Dry Specimen Mass (g)	3222.5	964.7	241.1
Date/time in oven	May 2, 15:50	May 2, 15:42	May 2, 15:40
Secondary Container + Dry Specimen Mass (g)	3220.1	960.6	345.4
Date/time in oven	May 3, 8:48	May 3, 8:30	May 3, 8:40
Final Container + Dry Specimen Mass (g)	3220.1	960.5	345.3
Date/time in oven	May 3, 10:50	May 3, 10:40	May 3, 10:46
Mass of Water	105.4	32.7	10.7
Mass of Solids	2669.2	913.51	341.3
Water Content	3.95	3.58	3.14
Average moisture content	3.6		

Table I.6. Moisture content result for the Subgrade material.

Moisture Content Test			
Soil Location and Date	Subgrade at -80cm before excavation - 23/04/2019		
Soil description	Clayey, brown material. Presence of sand and gravel.		
Container Number	SG01	SG02	SG03
Container Mass (g)	50.7	586	50.9
Initial Container + Moist Specimen Mass (g)	1297.5	2740.5	1308.8
Date/time in oven	May 2, 12:10	May 3, 10:50	May 3, 10:51
First Container + Dry Specimen Mass (g)	1228.2	2532.7	1219.9
Date/time in oven	May 2, 15:30	May 3, 15:52	May 3, 15:53
Secondary Container + Dry Specimen Mass (g)	1108.6	2361	1086.2
Date/time in oven	May 3, 8:35	May 4, 11:30	May 4, 11:31
Final Container + Dry Specimen Mass (g)	1108	2352.2	1083.3
Date/time in oven	May 3, 10:37	May 6, 8:40	May 6, 8:41
Mass of Water	189.5	388.3	225.5
Mass of Solids	1057.3	1766.2	1032.4
Water Content	17.92	21.99	21.84
Average moisture content	20.6		

I.2 – Sieve Analyses

Table I.7. Grain-size Analysis result for the Control Top Ballast sample.

Grain Size Analysis Report			Date:	10/05/2019
Sample Name:	Ballast Top 23/04			
Mass Sample:	4855.40			
Sieve Number (Ref. Weight)	Mesh Size (mm)	Mass Sieve + Sand (gm)	Percent Retained	Percent Passing Through
	38.10	1495.90	25.6%	74.4%
	25.0	1883.20	32.2%	42.2%
	19.10	749.60	12.8%	29.4%
	9.50	726.70	12.4%	16.9%
4	4.760	290.10	4.9%	12.0%
10 (411.6)	2.0	170.90	2.9%	9.0%
20	0.841	99.90	1.7%	7.3%
40 (415.9)	0.425	51.40	0.9%	6.4%
60 (380.7)	0.250	39.60	0.7%	5.8%
100 (513.0)	0.149	43.40	0.7%	5.0%
140 (349.3)	0.106	27.50	0.5%	4.5%
200	0.074	24.70	0.4%	4.1%
Pan	0.0	241.30	4.1%	0.0%

Table I.8. Grain-size Analysis result for the Control Bottom Ballast sample.

Grain Size Analysis Report			Date:	10/05/2019
Sample Name:	Ballast Bottom 23/04			
Mass Sample:	4017.0			
Sieve Number (Ref. Weight)	Mesh Size (mm)	Mass Sieve + Sand (gm)	Percent Retained	Percent Passing Through
	38.10	1254.60	23.04%	76.96%
	25.0	1467.90	26.96%	50.00%
	19.10	692.40	12.72%	37.29%
	9.50	602.10	11.06%	26.23%
4	4.760	261.80	4.81%	21.42%
10 (411.6)	2.0	216.50	3.98%	17.45%
20	0.841	173.20	3.18%	14.27%
40 (415.9)	0.425	99.40	1.83%	12.44%
60 (380.7)	0.250	72.60	1.33%	11.11%
100 (513.0)	0.149	76.10	1.40%	9.71%
140 (349.3)	0.106	48.10	0.88%	8.83%
200	0.074	40.0	0.73%	8.09%
Pan	0.0	440.70	8.09%	0.00%

Table I.9. Grain-size Analysis result for the Control Subballast sample.

Grain Size Analysis Report			Date:	07/05/2019
Sample Name:		Subballast 23/04		
Mass Sample:		1831.20		
Sieve Number (Ref. Weight)	Mesh Size (mm)	Mass Sieve + Sand (gm)	Percent Retained	Percent Passing Through
	25.0	590.50	24.7%	75.3%
	19.10	281.40	11.7%	63.6%
	9.50	615.30	25.7%	37.9%
	4.760	344.0	14.4%	23.5%
10 (411.6)	2.0	248.0	10.3%	13.2%
20	0.841	161.70	6.8%	6.4%
40 (415.9)	0.425	93.0	3.9%	2.5%
60 (380.7)	0.250	33.60	1.3%	1.2%
100 (513.0)	0.149	15.10	0.6%	0.5%
140 (349.3)	0.106	5.50	0.2%	0.3%
Pan	0.0	6.90	0.3%	0.0%

Table I.10. Grain-size analysis results for the Clean Ballast samples.

Grain Size Analysis Report			Date:	07/05/2019
Sample Name:		Ballast 24/04		
Mass Sample:		2440.60		
Sieve Number (Ref. Weight)	Mesh Size (mm)	Mass Sieve + Sand (gm)	Percent Retained	Percent Passing Through
	25.0	2416.70	99 %	1%
	19.10	0.0	0.0%	1%
	12.50	23.90	1%	0.0%
Pan	0	0	0.0%	0.0%

Grain Size Analysis Report			Date:	10/05/2019
Sample Name:		Ballast 24/04		
Mass Sample:		2231.60		
Sieve Number (Ref. Weight)	Mesh Size (mm)	Mass Sieve + Sand (gm)	Percent Retained	Percent Passing Through
	38.10	1813.10	81.2%	18.8%
	25.0	394.6	17.7%	1.1%
	19.10	0.0	0.00%	1.1%
	12.50	23.9	1.1%	0.0%
Pan	0	0	0.00%	0.0%

Table I.11. Grain-size analysis result for the Clean Subballast sample.

Grain Size Analysis Report			Date:	07/05/2019
Sample Name:	Subballast 24/04			
Mass Sample:	451.70			
Sieve Number (Ref. Weight)	Mesh Size (mm)	Mass Sieve + Sand (gm)	Percent Retained	Percent Passing Through
	25.0	9.30	1.1%	99.9%
	19.10	128.50	15.1%	83.8%
	9.50	213.50	25%	58.8%
	4.760	100.40	11.7%	47.1%
10 (411.6)	2.0	92.20	10.8%	36.3%
20	0.841	57.10	6.7%	29.6%
40 (415.9)	0.425	109.40	12.8%	16.8%
60 (380.7)	0.250	90.50	10.6%	6.3%
100 (513.0)	0.149	35.10	4.1%	2.2%
140 (349.3)	0.106	10.90	1.3%	0.9%
Pan	0.0	7.50	0.9%	0.0%

Table I.12. Grain-size analysis result for the Subgrade sample.

Grain Size Analysis Report			Date:	10/05/2019
Sample Name:	Subgrade (80cm)			
Mass Sample:	521.3			
Sieve Number (Ref. Weight)	Mesh Size (mm)	Mass Sieve + Sand (gm)	Percent Retained	Percent Passing Through
	25.0	82.80	7.8%	92.2%
	19.10	14.90	1.4%	90.8%
	9.50	52.90	5%	85.8%
	4.760	28.10	2.6%	83.1%
10 (411.6)	2.0	38.0	3.6%	79.6%
20	0.841	39.10	3.7%	75.9%
40 (415.9)	0.425	43.70	4.1%	71.7%
60 (380.7)	0.250	58.0	5.5%	66.3%
100 (513.0)	0.149	78.90	7.4%	58.8%
200	0.074	84.90	8.0%	50.8%
-	0.051826	-	13.4%	37%
-	0.01966	-	6.4%	31%
-	0.011677	-	4.0%	27%
-	0.008309	-	0.8%	26%
-	0.005997	-	3.2%	23%
-	0.003033	-	3.9%	19%
-	0.001305	-	3.9%	15%

Figure I.1. Particle size distribution plots for Control Ballast top sample.

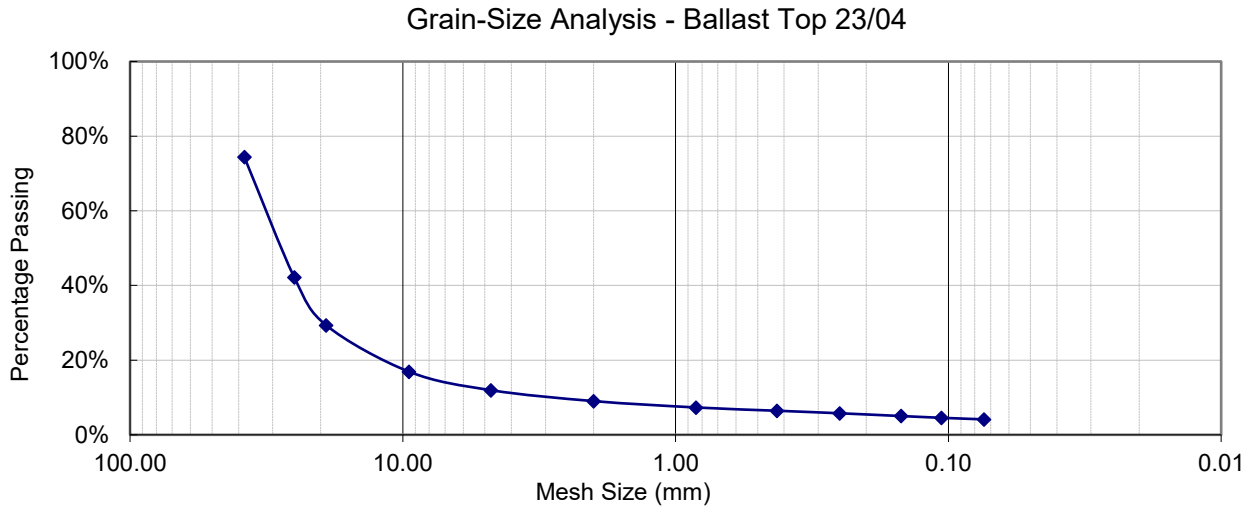


Figure I.2. Particle size distribution plots for Control Ballast bottom sample.

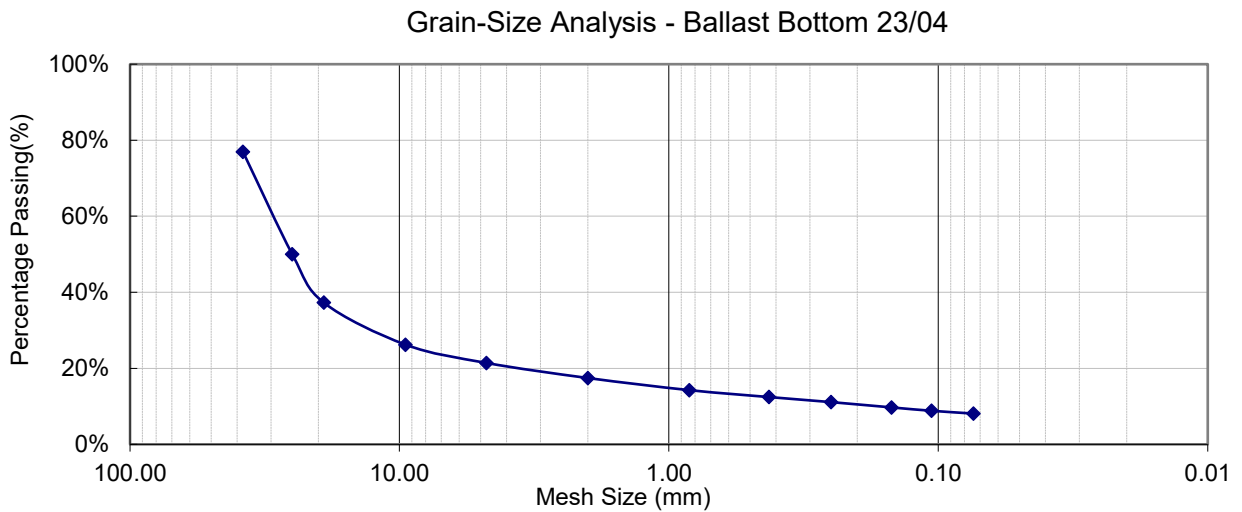


Figure I.3. Particle size distribution plots for Control Subballast sample.

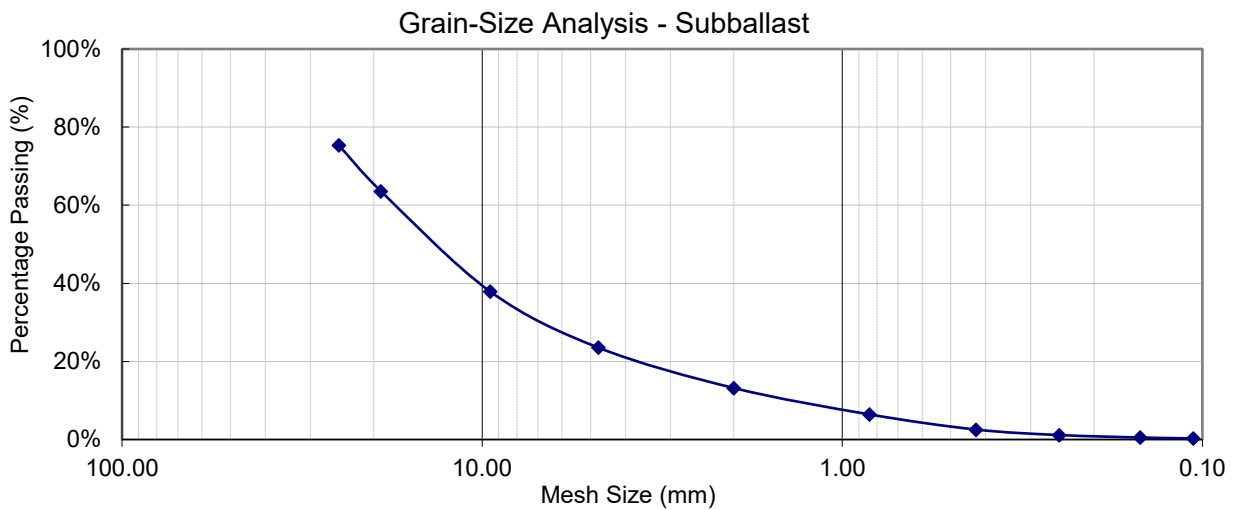


Figure I.4. Particle size distribution plots for Clean Ballast samples

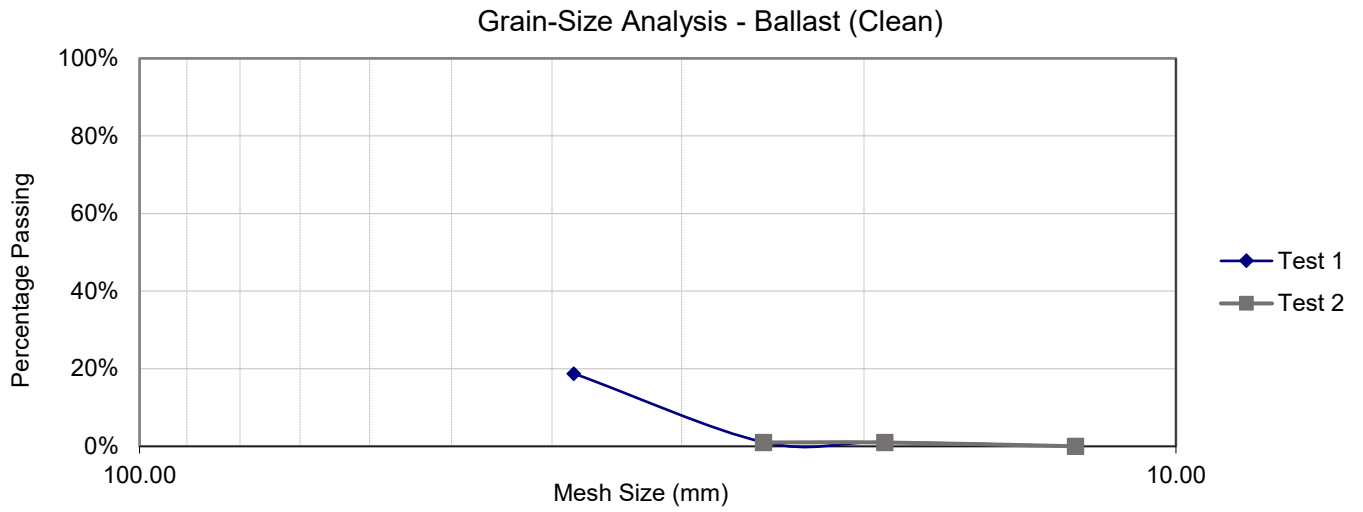


Figure I.5. Particle size distribution plots for Clean Subballast samples.

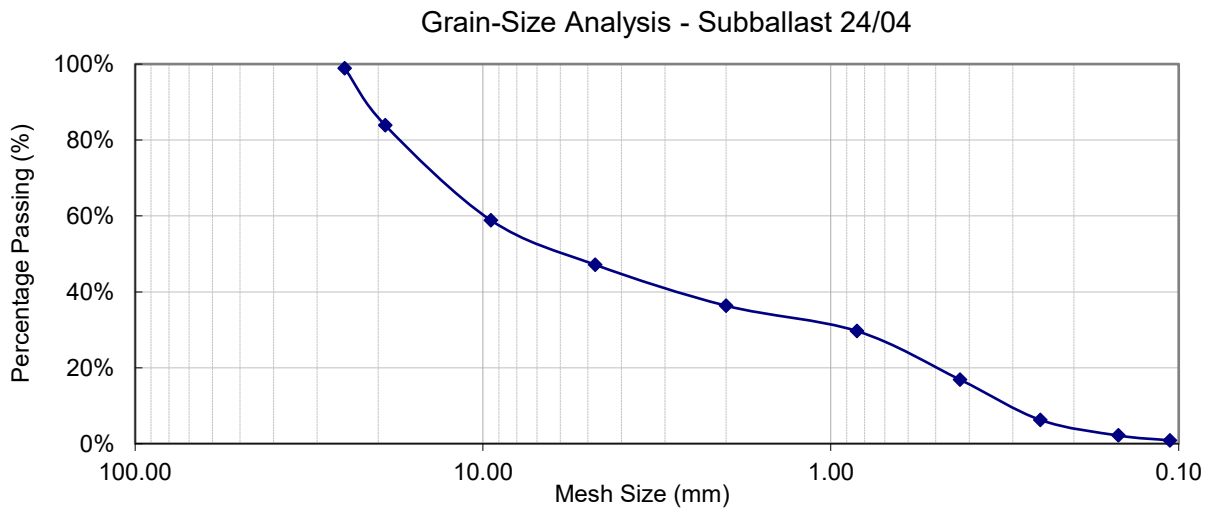
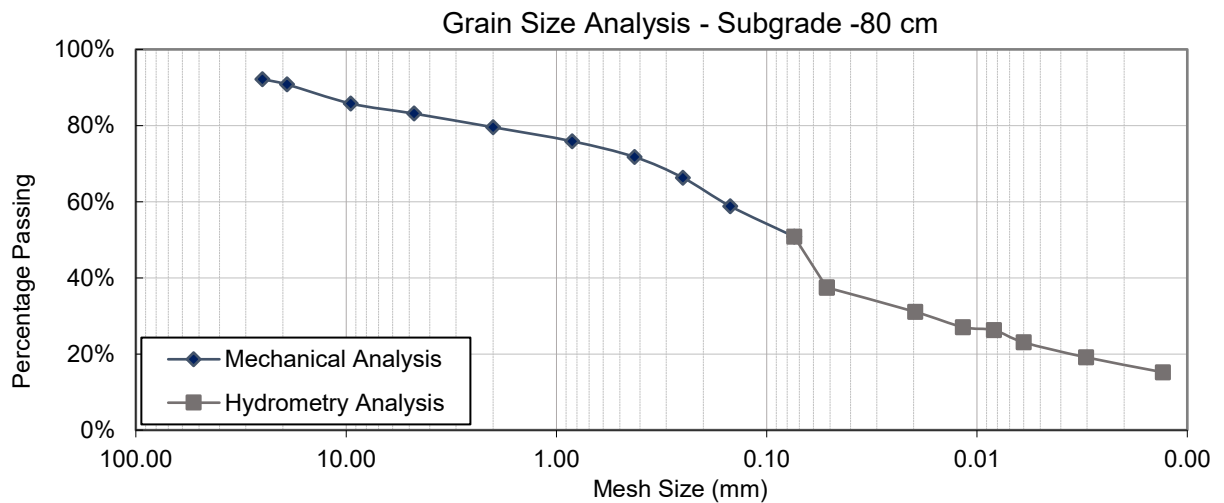


Figure I.6. Particle size distribution plots for Subgrade sample.



I.3 – Atterberg Limits

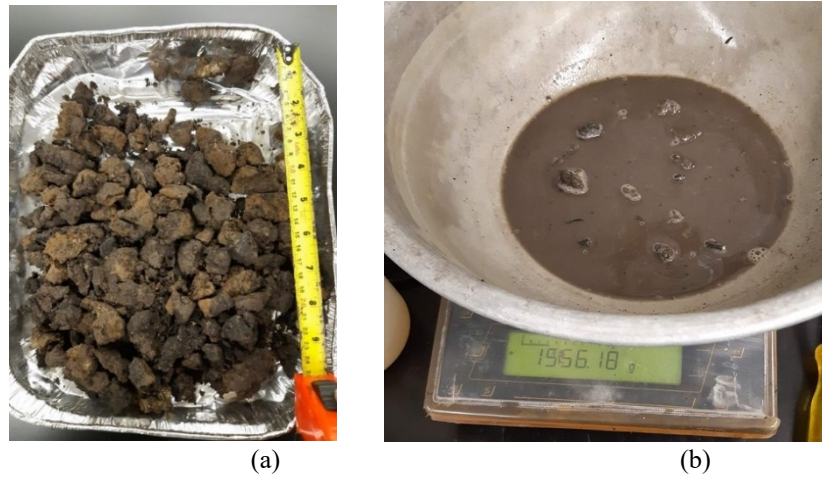


Figure I.7. Subgrade Atterberg Limits. (a) Soil before wet preparation. (b) Soil after wetting.

Table I.13. Atterberg Limits Results for Subgrade soil.

Soil type:	Subgrade		Location:	Scotford					
Sample Depth:	80 cm		Date:	July 22 nd , 2019					
USCS Soil Classification:	Sandy lean clay with gravel		Procedure:	A- Wet preparation					
TEST			Plastic Limit			Liquid Limit			
Variable	NO		1	2	3	1	2	3	4
	Var.	Units							
Number of Blows	N	blows	-	-	-	27	27	34	35
Can Number	---	---	1151	325	P1	P2-53	G1-S1	10-20	6b1
Mass of Empty Can	M _C	(g)	1.90	1.37	2.23	1.40	1.4	1.40	2.06
Mass Can & Soil (Wet)	M _{CMS}	(g)	2.72	1.87	2.54	9.93	9.80	7.66	9.32
Mass Can & Soil (Dry)	M _{CDS}	(g)	2.59	1.79	2.49	7.47	7.45	5.95	7.37
Mass of Soil	M _S	(g)	6.21	6.3	6.5	6.07	6.05	4.55	5.31
Mass of Water	M _W	(g)	1.17	1.2	1.25	2.46	2.35	1.71	1.95
Water Content	w	(%)	18.8	19.0	19.2	40.5	38.8	37.6	36.7

Table I.14. Atterberg Limits Summary.

Liquid Limit (LL or w_L) (%):	40.5
Plastic Limit (PL or w_P) (%):	19
Plasticity Index (PI) (%):	21
USCS Classification:	CL

I.4 – Consolidated Direct Shear

Table I.15. Direct Shear Summary for Clean Subballast with $\sigma=100$ kPa.

Consolidated Drained Direct Shear							
Tested by:	Camila Alvarenga			Date Tested:	27-07-2020		
Sample No :	SB-01			Confining Stress:	100 kPa		
Sample Description:	Subballast Clean material						
Deformation rate peak (in/min):	0.0032			Deformation rate residual (in/min):	-		
Test Details:							
Sample Diameter (mm) :	63.29333333			Sample Height (mm):	27.79		
Sample Area (A_0) (mm ²):	3146.341206			Sample Volume (mm ³):	87436.82211		
Mold Mass (g):	1043.2			Soil + Mold Mass (g):	1214.8		
Sample Mass (Wet) (g):	171.6			Sample Mass (Dry) (g):			
Total Unit Weight, γ (kgf/m ³):	1.96255989			Dry Unit Weight, γ_d (kgf/m ³):			
initial void ratio:	0.57						
Final Water Content:	Container No.	Mass of Empty Container (g)	Mass of Soil and Container Wet (g)	Mass of Soil and Container Dry (g)	Mass of Water (g)	Mass of Soil (g)	Water Content (%)
Initial 2	40kPa	3.6	51	47.3	3.7	43.7	8.47
Final		3.6	124.5	109.9	14.6	106.3	13.73
Average					0	0	
File name	start time	Sample Load (kPa)	Pressure Load from the calibration curve (psi)	End Time	Displacements and load		
					Hdsp (mm)	Vdsp (mm)	
					0	0	
				-	14.84884	0.93726	

Sub-ballast (Clean) - 100 kPa

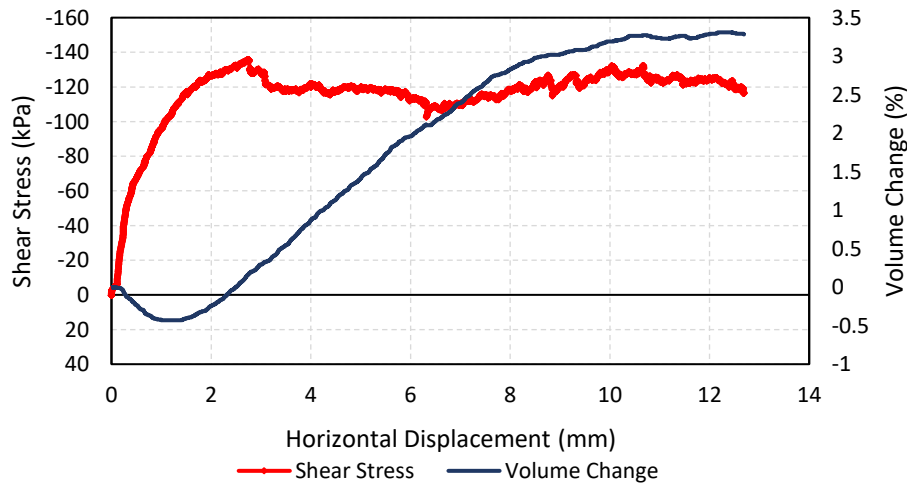


Figure I.8. Hor. Displacement vs. Shear Stress/Volume Change for Clean Subballast with $\sigma=100$ kPa.

Table I.16. Direct Shear Summary for Clean Subballast with $\sigma=200$ kPa.

Consolidated Drained Direct Shear							
Tested by: Camila Alvarenga			Date Tested: 31-07-2020				
Sample No : SB-02			Confining Stress: 200 kPa				
Sample Description: Subballast Clean material							
Deformation rate peak (in/min):		0.0032		Deformation rate residual (in/min):		-	
Test Details:							
Sample Diameter (mm) :		63.3		Sample Height (mm):		26.93	
Sample Area (A_0) (mm ²):		3146.3		Sample Volume (mm ³):		84731	
Mold Mass (g):		1043.2		Soil + Mold Mass (g):		1211.9	
Sample Mass (Wet) (g):		168.7		Sample Mass (Dry) (g):			
Total Unit Weight, γ (kgf/m ³):		1.99		Dry Unit Weight, γ_d (kgf/m ³):			
initial void ratio:		0.57					
Final Water Content:	Container No.	Mass of Empty Container (g)	Mass of Soil and Container Wet (g)	Mass of Soil and Container Dry (g)	Mass of Water (g)	Mass of Soil (g)	Water Content (%)
Initial 2	40kPa	3.6	129.2	127	2.2	123.4	2%
Final	shearfinal ₁	5	131.9	117.6	14.3	112.6	12.70 %
File name	start time	Sample Load (kPa)	Pressure Load from the calibration curve (psi)	End Time	Displacements and load		
						Hdsp (mm)	Vdsp (mm)
						0	0
						6.39	0.876

Sub-ballast (Clean) - 200 kPa

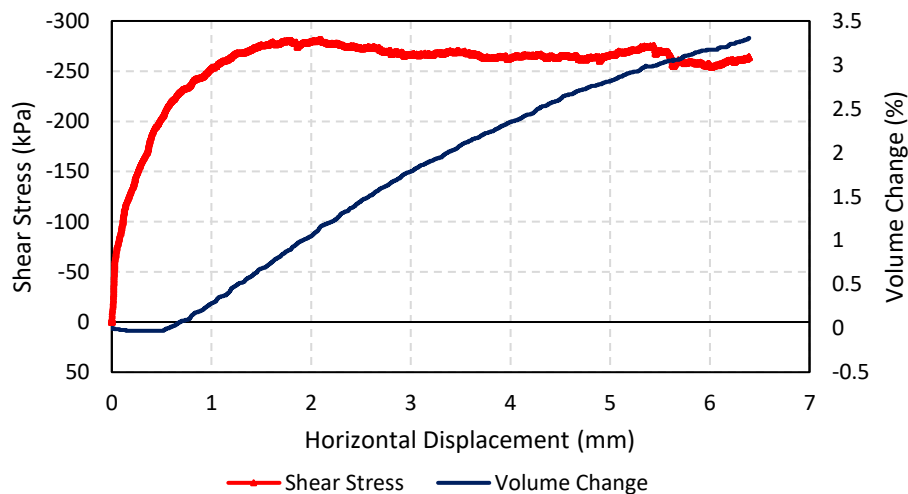


Figure I.9. Hor. Displacement vs. Shear Stress/Volume Change for Clean Subballast with $\sigma=200$ kPa.

Table I.17. Direct Shear Summary for Clean Subballast with $\sigma=500$ kPa.

Consolidated Drained Direct Shear							
Tested by: Camila Alvarenga		Date Tested: 05-08-2020					
Sample No : SB-03		Confining Stress: 500 kPa					
Sample Description:		Subballast Clean material					
Deformation rate peak (in/min): 0.0032		Deformation rate residual (in/min): -					
Test Details:							
Sample Diameter (mm) :		63.29		Sample Height (mm):		26.5	
Sample Area (A_0) (mm ²):		3146.34		Sample Volume (mm ³):		83378.04	
Mold Mass (g):		1043.2		Soil + Mold Mass (g):		1221.9	
Sample Mass (Wet) (g):		178.7		Sample Mass (Dry) (g):			
Total Unit Weight, γ (kgf/m ³):		2.14		Dry Unit Weight, γ_d (kgf/m ³):			
initial void ratio:		0.57					
Final Water Content:	Container No.	Mass of Empty Container (g)	Mass of Soil and Container Wet (g)	Mass of Soil and Container Dry (g)	Mass of Water (g)	Mass of Soil (g)	Water Content (%)
Initial 2	shearinitial1	5	261.8	255.8	6	250.8	0.02
Failure plane	initial1	3.7	117.5	105	12.5	101.3	0.12
Final	final2	5	69.9	62.2	7.7	57.2	0.13
File name	start time	Sample Load (kPa)	Pressure Load from the calibration curve (psi)		End Time	Displacements and load	
						Hdsp (mm)	Vdsp (mm)
						0	0
					-	6.904	1.194

Sub-ballast (Clean) - 500 kPa

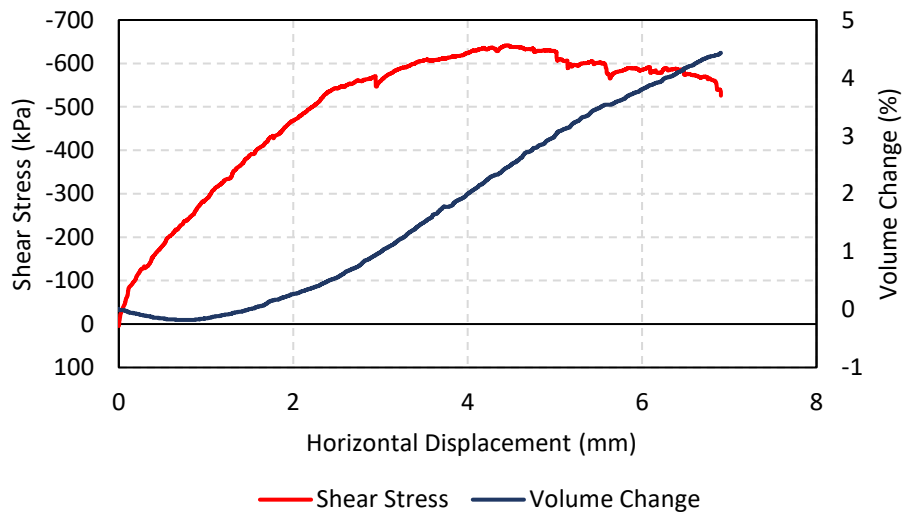


Figure I.10. Hor. Displacement vs. Shear Stress/Volume Change for Clean Subballast with $\sigma=500$ kPa.

Table I.18. Direct Shear Summary for Control Subballast with $\sigma=100$ kPa.

Consolidated Drained Direct Shear							
Tested by: Camila Alvarenga		Date Tested: 11-08-2020					
Sample No : FSB-02		Confining Stress: 100 kPa					
Sample Description:							
Deformation rate peak (in/min): 0.0032		Deformation rate residual (in/min): -					
Test Details:							
Sample Diameter (mm) : 63.29		Sample Height (mm): 24.52					
Sample Area (A_0) (mm^2): 3146.34		Sample Volume (mm^3): 77153.53					
Mold Mass (g): 126.6		Soil + Mold Mass (g): 310.3					
Sample Mass (Wet) (g): 183.7		Sample Mass (Dry) (g):					
Total Unit Weight, γ (kgf/m^3): 2.38		Dry Unit Weight, γ_d (kgf/m^3):					
initial void ratio: 0.57							
Final Water Content:	Container No.	Mass of Empty Container (g)	Mass of Soil and Container Wet (g)	Mass of Soil and Container Dry (g)	Mass of Water (g)	Mass of Soil (g)	Water Content (%)
Initial 2	initial2	3.6	112.9	103.5	9.4	99.9	0.09
Final	shearfinal1	5.3	180.7	161.6	19.1	156.3	0.12
File name	start time	Sample Load (kPa)	Pressure Load from the calibration curve (psi)		End Time	Displacements and load	
						Hdsp (mm)	Vdsp (mm)
						0	0
					-	-0.24	2.00

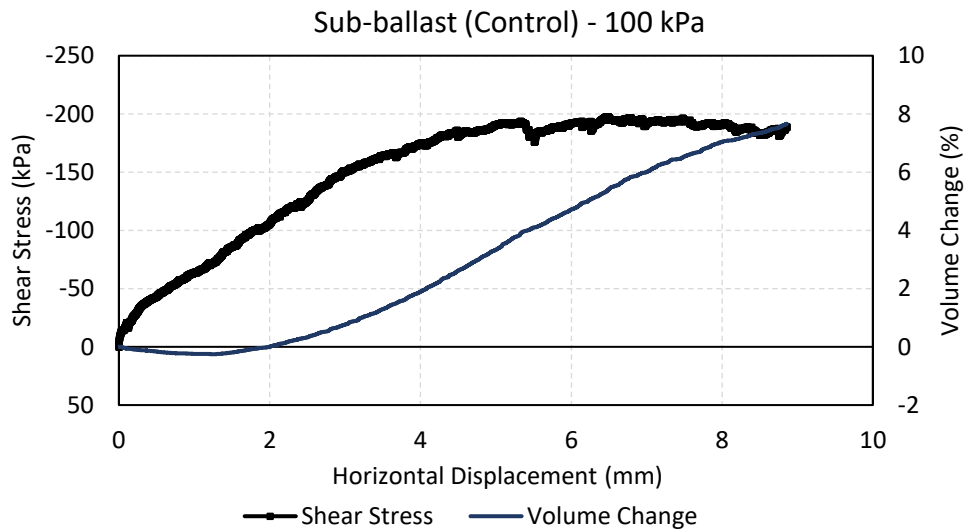


Figure I.11. Hor. Displacement vs. Shear Stress/Volume Change for Control Subballast with $\sigma=100$ kPa.

Table I.19. Direct Shear Summary for Control Subballast with $\sigma=200$ kPa.

Consolidated Drained Direct Shear							
Tested by: Camila Alvarenga		Date Tested: 07-08-2020					
Sample No : FSB-01		Confining Stress: 200 kPa					
Sample Description:							
Deformation rate peak (in/min):		0.0032		Deformation rate residual (in/min):		-	
Test Details:							
Sample Diameter (mm) :		63.29		Sample Height (mm):		26.1	
Sample Area (A_0) (mm ²):		3146.34		Sample Volume (mm ³):		81962.2	
Mold Mass (g):		125.1		Soil + Mold Mass (g):		314.1	
Sample Mass (Wet) (g):		189		Sample Mass (Dry) (g):			
Total Unit Weight, γ (kgf/m ³):		2.31		Dry Unit Weight, γ_d (kgf/m ³):			
initial void ratio:		0.57					
Final Water Content:	Container No.	Mass of Empty Container (g)	Mass of Soil and Container Wet (g)	Mass of Soil and Container Dry (g)	Mass of Water (g)	Mass of Soil (g)	Water Content (%)
Initial 1	final1	5	166.4	153.5	12.9	148.5	0.09
Final	shearfinal1	5	187.3	164.3	23	159.3	0.14
File name	start time	Sample Load (kPa)	Pressure Load from the calibration curve (psi)		End Time	Displacements and load	
						Hdsp (mm)	Vdsp (mm)
						0.61	0
					-	9.55	1.28

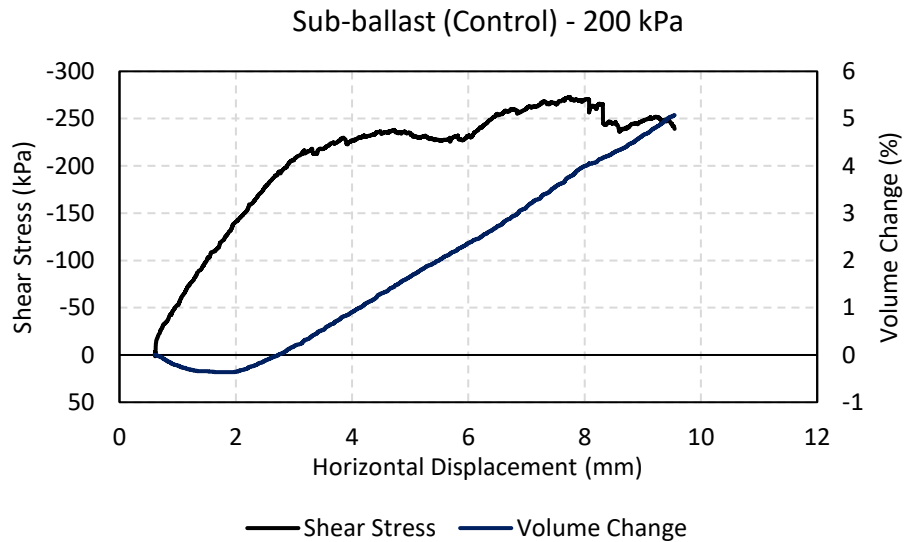


Figure I.12. Hor. Displacement vs. Shear Stress/Volume Change for Control Subballast with $\sigma=200$ kPa.

Table I.20. Direct Shear Summary for Control Subballast with $\sigma=400$ kPa.

Consolidated Drained Direct Shear							
Tested by: Camila Alvarenga		Date Tested: 13-08-2020					
Sample No : FSB-03		Confining Stress: 400 kPa					
Sample Description:							
Deformation rate peak (in/min): 0.0032		Deformation rate residual (in/min): -					
Test Details:							
Sample Diameter (mm) : 63.29		Sample Height (mm): 25.2					
Sample Area (A_0) (mm ²): 3146.34		Sample Volume (mm ³): 79253.7					
Mold Mass (g): 126.5		Soil + Mold Mass (g): 306.6					
Sample Mass (Wet) (g): 180.1		Sample Mass (Dry) (g):					
Total Unit Weight, γ (kgf/m ³): 2.27		Dry Unit Weight, γ_d (kgf/m ³):					
initial void ratio: 0.57							
Final Water Content:	Container No.	Mass of Empty Container (g)	Mass of Soil and Container Wet (g)	Mass of Soil and Container Dry (g)	Mass of Water (g)	Mass of Soil (g)	Water Content (%)
Initial 2	final2	3.6	164.3	146.2	18.1	142.6	0.13
Final	shearfinal1	5	175.9	155.1	20.8	150.1	0.14
File name	start time	Sample Load (kPa)	Pressure Load from the calibration curve (psi)		End Time	Displacements and load	
						Hdsp (mm)	Vdsp (mm)
						0	0
					-	8.61	1.68

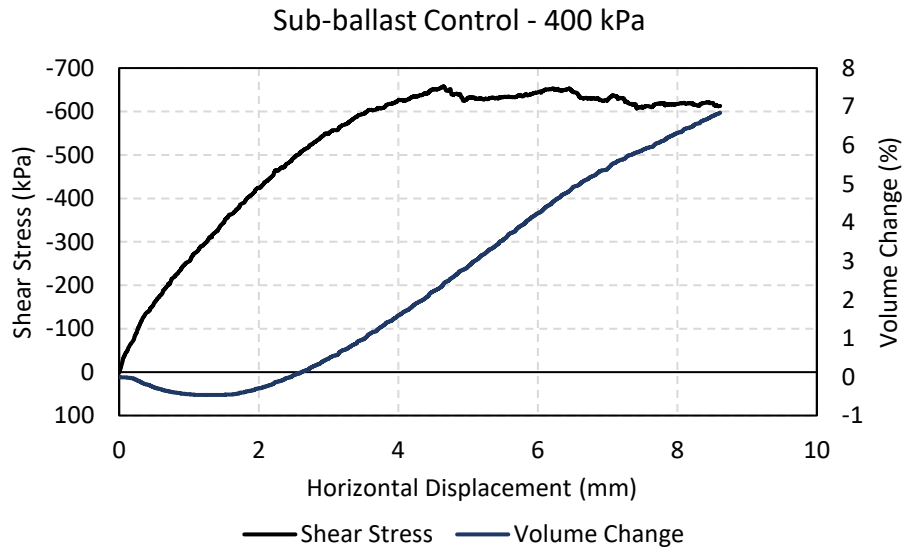


Figure I.13. Hor. Displacement vs. Shear Stress/Volume Change for Control Subballast with $\sigma=400$ kPa.

Table I.21. Direct Shear Summary for Subgrade with $\sigma=100$ kPa.

Consolidated Drained Direct Shear							
Tested by: Camila Alvarenga		Date Tested: 18-08-2020					
Sample No : SG-01		Confining Stress: 100 kPa					
Sample Description:							
Deformation rate peak (in/min): 0.0003		Deformation rate residual (in/min): -					
Test Details:							
Sample Diameter (mm) : 63.29		Sample Height (mm): 25.4					
Sample Area (A_0) (mm ²): 3146.34		Sample Volume (mm ³): 79885.6					
Mold Mass (g): 126.5		Soil + Mold Mass (g): 306.6					
Sample Mass (Wet) (g): 180.1		Sample Mass (Dry) (g):					
Total Unit Weight, γ (kgf/m ³): 2.25		Dry Unit Weight, γ_d (kgf/m ³):					
initial void ratio: 0.57							
Final Water Content:	Container No.	Mass of Empty Container (g)	Mass of Soil and Container Wet (g)	Mass of Soil and Container Dry (g)	Mass of Water (g)	Mass of Soil (g)	Water Content (%)
Initial 2	dsin3	3.6	59.1	48.8	10.3	45.2	0.23
Final	shearfinal1	5	165.6	134.1	31.5	129.1	0.24
Average							0.235
File name	start time	Sample Load (kPa)	Pressure Load from the calibration curve (psi)	End Time	Displacements and load		
						Hdsp (mm)	Vdsp (mm)
						0	0
					-	10.56	-0.50

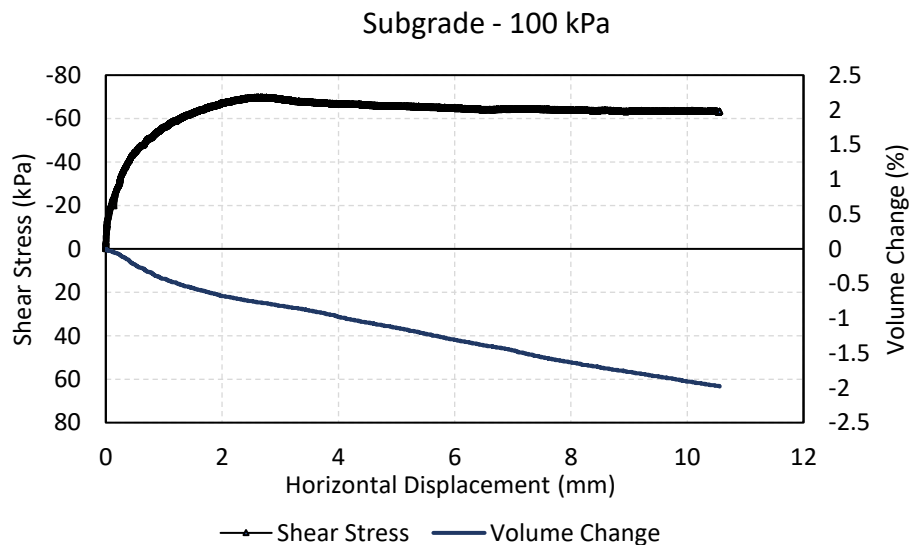


Figure I.14. Hor. Displacement vs. Shear Stress/Volume Change for Subgrade with $\sigma=100$ kPa.

Table I.22. Direct Shear Summary for Subgrade with $\sigma=200$ kPa.

Consolidated Drained Direct Shear							
Tested by: Camila Alvarenga		Date Tested: 28-08-2020					
Sample No : SG-03		Confining Stress: 200 kPa					
Sample Description:							
Deformation rate peak (in/min): 0.0003		Deformation rate residual (in/min): -					
Test Details:							
Sample Diameter (mm) : 63.29		Sample Height (mm): 25.4					
Sample Area (A_0) (mm ²): 3146.34		Sample Volume (mm ³): 79885.6					
Mold Mass (g): 126.1		Soil + Mold Mass (g): 292.7					
Sample Mass (Wet) (g): 166.6		Sample Mass (Dry) (g):					
Total Unit Weight, γ (kgf/m ³): 2.09		Dry Unit Weight, γ_d (kgf/m ³):					
initial void ratio: 0.57							
Final Water Content:	Container No.	Mass of Empty Container (g)	Mass of Soil and Container Wet (g)	Mass of Soil and Container Dry (g)	Mass of Water (g)	Mass of Soil (g)	Water Content (%)
Initial 1	initial2	3.7	78.7	65.2	13.5	61.5	0.22
Final	final2	3.6	166.4	137.7	28.7	134.1	0.21
Average							0.215
File name	start time	Sample Load (kPa)	Pressure Load from the calibration curve (psi)		End Time	Displacements and load	
						Hdsp (mm)	Vdsp (mm)
						0	-2.57
					-	10.67	-3.46

Subgrade- 200 kPa

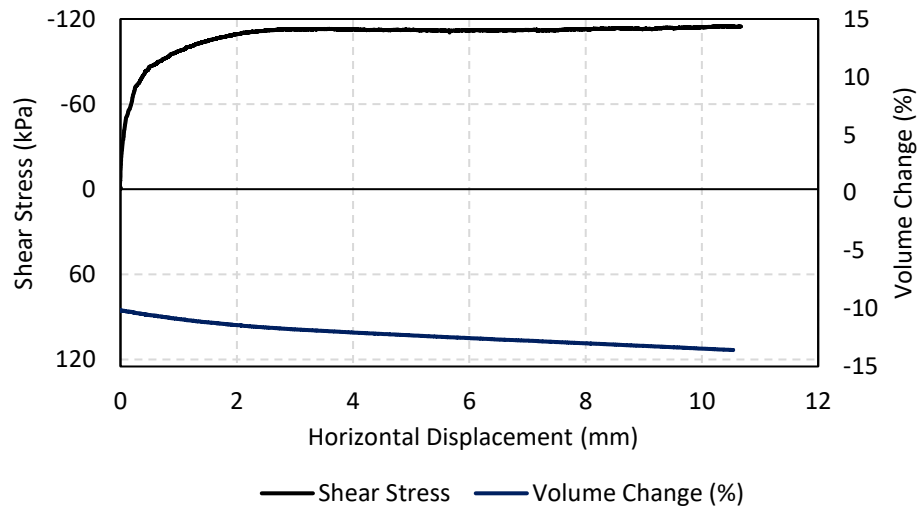


Figure I.15. Hor. Displacement vs. Shear Stress/Volume Change for Subgrade with $\sigma=200$ kPa.

Table I.23. Direct Shear Summary for Subgrade with $\sigma=400$ kPa.

Consolidated Drained Direct Shear							
Tested by: Camila Alvarenga		Date Tested: 24-08-2020					
Sample No : SG-02		Confining Stress: 400kPa					
Sample Description:							
Deformation rate peak (in/min): 0.0003		Deformation rate residual (in/min): -					
Test Details:							
Sample Diameter (mm) : 63.29		Sample Height (mm): 25.4					
Sample Area (A_0) (mm ²): 3146.34		Sample Volume (mm ³): 79885.6					
Mold Mass (g): 125		Soil + Mold Mass (g): 285.8					
Sample Mass (Wet) (g): 160.8		Sample Mass (Dry) (g):					
Total Unit Weight, γ (kgf/m ³): 2.01		Dry Unit Weight, γ_d (kgf/m ³):					
initial void ratio: 0.57							
Final Water Content:	Container No.	Mass of Empty Container (g)	Mass of Soil and Container Wet (g)	Mass of Soil and Container Dry (g)	Mass of Water (g)	Mass of Soil (g)	Water Content (%)
Initial	shearinitial1	5	106.5	91.4	15.1	86.4	0.17
Final	shearfinal1	4.8	171.9	147.2	24.7	142.4	0.17
Average							0.17
File name	start time	Sample Load (kPa)	Pressure Load from the calibration curve (psi)	End Time	Displacements and load		
						Hdsp (mm)	Vdsp (mm)
						0	0.58166
						12.73556	-0.55429

Subgrade- 400 kPa

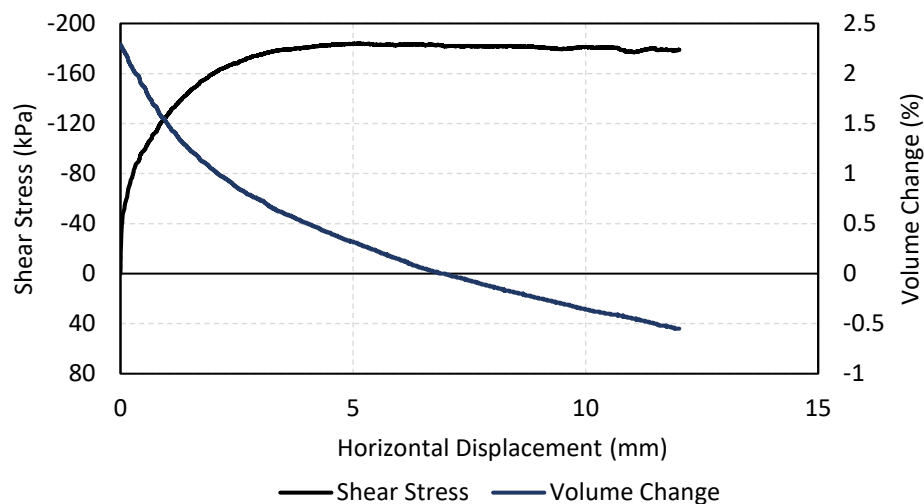


Figure I.16. Hor. Displacement vs. Shear Stress/Volume Change for Subgrade with $\sigma=400$ kPa.

I.5 – SWCCs

Table I.24. Soil-water characteristic curve test data for the first Clean Subballast test.

SWCC - Subballast (Clean)						
		Initial volume		Final water content		
cell (g)	1658.16		Dia.(cm)	6.9	tare (g)	3.7
cell+sample (g)	1852.06		Initial height (cm)	3.3	tare+wet (g)	198.4
			Initial vol. (cm3)	123.4	tare+dry (g)	193.9
sample (g)	193.9		Final volume			
soil (g)	193.9		Dia. (cm)	6.9		
w.c. (%)	0		Final vol. (cm3)	112.2		
suction	weight	w.c.	final w.c. (Grav.)	vol. w.c.	Grav. W.C.	Vol. W.C.
(kPa)	(g)		(dec.)	(dec.)	(%)	(%)
0.2	1824.7	0.86	0.152	0.306	15.2	30.6
0.3	1823.23	0.85	0.144	0.291	14.4	29.1
0.5	1824.6	0.86	0.151	0.305	15.1	30.5
0.8	1823.53	0.85	0.146	0.294	14.6	29.4
1	1824.61	0.86	0.151	0.305	15.1	30.5
2	1824.51	0.86	0.151	0.304	15.1	30.4
3	1817.29	0.82	0.114	0.229	11.4	22.9
6	1806.79	0.77	0.059	0.120	5.9	12.0
10	1803.98	0.75	0.045	0.091	4.5	9.1
15	1802.39	0.74	0.037	0.074	3.7	7.4
30	1802.15	0.74	0.036	0.072	3.5	7.2
50	1800.52	0.73	0.027	0.055	2.7	5.4
100	1799.8	0.73	0.023	0.047	2.3	4.7

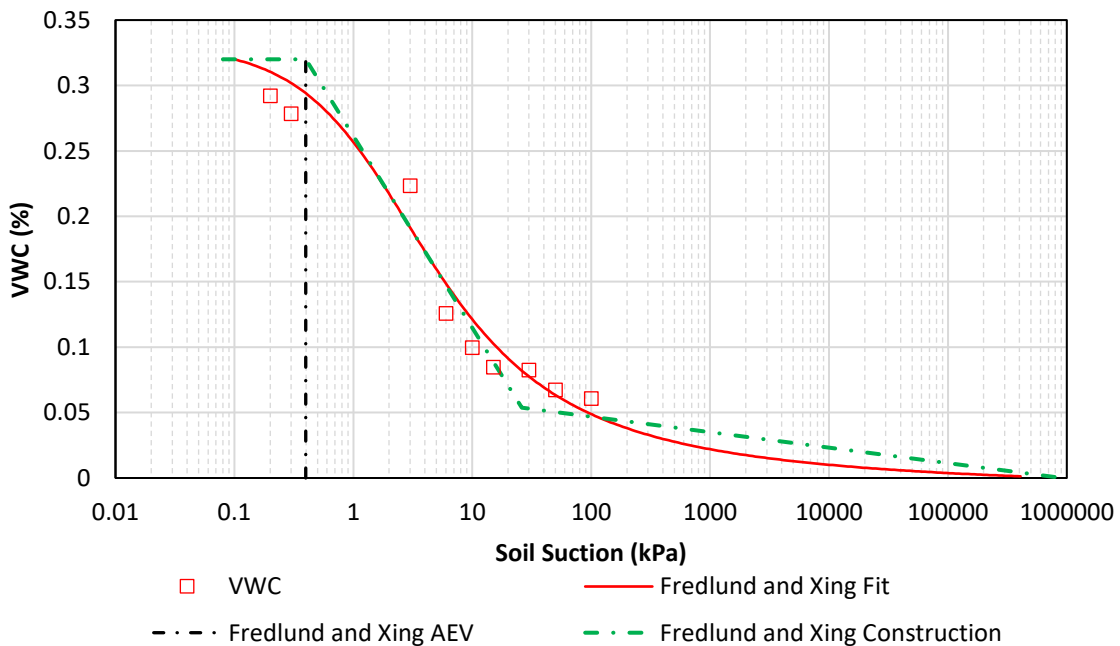


Figure I.17. Soil-water characteristic curve for first Clean Subballast test.

Table I.25. Soil-water characteristic curve test data for second Clean Subballast test.

SWCC - Subballast (Remediated)						
		Volume			Final water content	
cell (g)	1669.2		Dia.(cm)	6.9	tare (g)	3.76
cell+sample (g)	1918.87		Initial height (cm)	2.5	tare+wet (g)	161.93
			Initial vol. (cm3)	93.5	tare+dry (g)	155.41
water (g)	0		Final height (cm)	2.3		
soil (g)	249.67		Dia. (cm)	6.9		
w.c. (%)	0		Final vol. (cm3)	86.0		
suction	weight	w.c.	final w.c. (Grav.)	vol. w.c.	Grav. W.C.	Vol. W.C.
(kPa)	(g)		(dec.)	(dec.)	(%)	(%)
0.2	1824.7	-0.38	0.126	0.221	12.6	22.1
0.3	1823.23	-0.38	0.103	0.182	10.3	18.2
0.5	1824.6	-0.38	0.108	0.191	10.9	19.1
0.8	1823.53	-0.38	0.104	0.184	10.4	18.4
1	1824.61	-0.38	0.109	0.191	10.9	19.1
2	1824.51	-0.38	0.108	0.191	10.8	19.1
3	1817.29	-0.41	0.079	0.140	7.9	14.0
6	1806.79	-0.45	0.037	0.066	3.7	6.6
10	1803.98	-0.46	0.026	0.046	2.6	4.6
15	1802.39	-0.46	0.020	0.035	2.0	3.5
30	1802.15	-0.46	0.019	0.0330	1.9	3.3
50	1800.52	-0.47	0.012	0.0216	1.2	2.2
100	1799.8	-0.48	0.009	0.0165	0.9	1.6

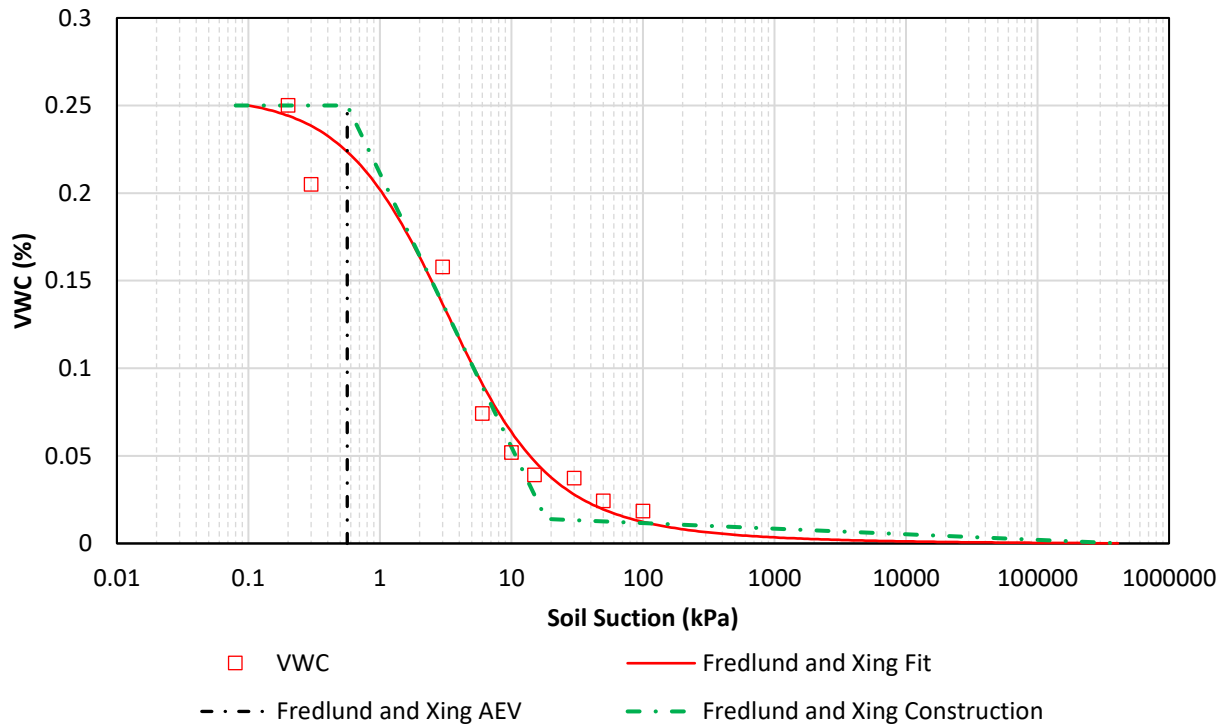


Figure I.18. Soil-water characteristic curve for second Clean Subballast test.

Table I.26. Soil-water characteristic curve test data for first Control Subballast test.

SWCC - Subballast (Control)						
		Volume			Final water content	
cell (g)	1652.98		Dia.(cm)	6.9	tare (g)	3.7
cell+sample (g)	1892.83		Initial height (cm)	4.5	tare+wet (g)	215.96
			Initial vol. (cm3)	168.3	tare+dry (g)	200.72
sample (g)	239.85		Final volume			
water (g)	42.83		Final height (cm)	4.2		
soil (g)	197.02		Dia. (cm)	6.9		
w.c. (%)	0.217		Final vol. (cm3)	157.0		
Suction	Weight	w.c.	Final w.c. (Grav.)	Vol. w.c.	Grav. W.C.	Vol. W.C.
(kPa)	(g)		(dec.)	(dec.)	(%)	(%)
0.1	2004.04	0.78	0.468	0.573	46.8	57.3
0.2	2004.04	0.78	0.468	0.573	46.8	57.3
0.3	2004.04	0.78	0.468	0.573	46.8	57.3
0.4	2004.04	0.78	0.468	0.573	46.8	57.3
0.6	2004.04	0.78	0.468	0.573	46.8	57.3
1	2003.76	0.78	0.466	0.572	46.6	57.2
1.5	1993.16	0.73	0.412	0.506	41.2	50.6
2	1978.87	0.65	0.340	0.417	34.0	41.7
3	1976.38	0.64	0.327	0.401	32.7	40.1
9	1943.45	0.47	0.160	0.196	16.0	19.6
15	1939.8	0.45	0.142	0.174	14.2	17.4
30	1930.81	0.41	0.096	0.118	9.6	11.8
60	1929.7	0.40	0.090	0.111	9.0	11.1
80	1927.89	0.39	0.081	0.100	8.1	10.0
150	1927.13	0.39	0.077	0.095	7.7	9.5

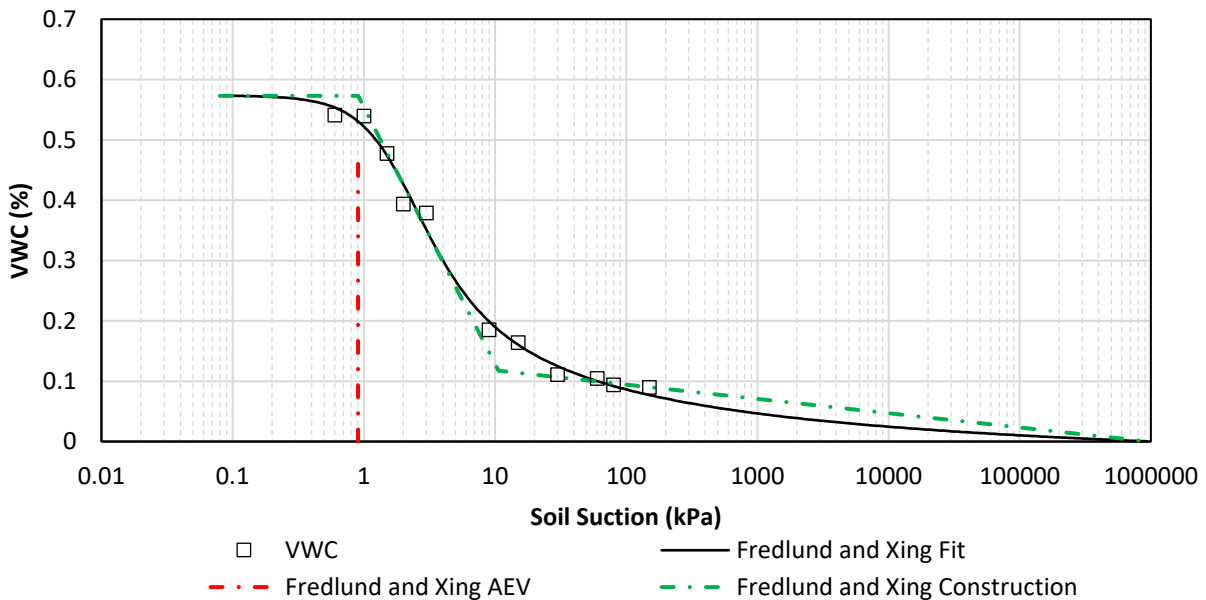


Figure I.19. Soil-water characteristic curve for first Control Subballast test.

Table I.26. Soil-water characteristic curve test data for second Control Subballast test.

SWCC - Subballast (Control)						
		Volume			Final water content	
cell (g)	1652.98		Dia.(cm)	6.9	tare (g)	3.7
cell+sample (g)	1918.87		Initial height (cm)	4.5	tare+wet (g)	287.26
			Initial vol. (cm3)	168.27	tare+dry (g)	269.31
sample (g)	301.81		Final volume			
water (g)	36.2		Final height (cm)	4		
soil (g)	265.61		Dia. (cm)	6.9		
w.c. (%)	0.136		Final vol. (cm3)	149.6		
Suction (kPa)	Weight (g)	w.c.	Final w.c. (Grav.) (dec.)	Vol. w.c. (dec.)	Grav. W.C. (%)	Vol. W.C. (%)
1	1954.79	0.271	0.225	0.393	22.5	39.3
1.6	1944.29	0.232	0.186	0.324	18.6	32.4
3	1932.85	0.189	0.143	0.249	14.3	24.9
6	1929.39	0.176	0.129	0.226	12.9	22.6
15	1923.35	0.153	0.107	0.186	10.7	18.6
30	1923.2	0.153	0.106	0.185	10.6	18.5
40	1921.8	0.147	0.101	0.176	10.1	17.6
80	1917.78	0.132	0.086	0.150	8.6	15.0
150	1915.8	0.124	0.078	0.137	7.8	13.7
300	1912.95	0.114	0.068	0.118	6.8	11.8

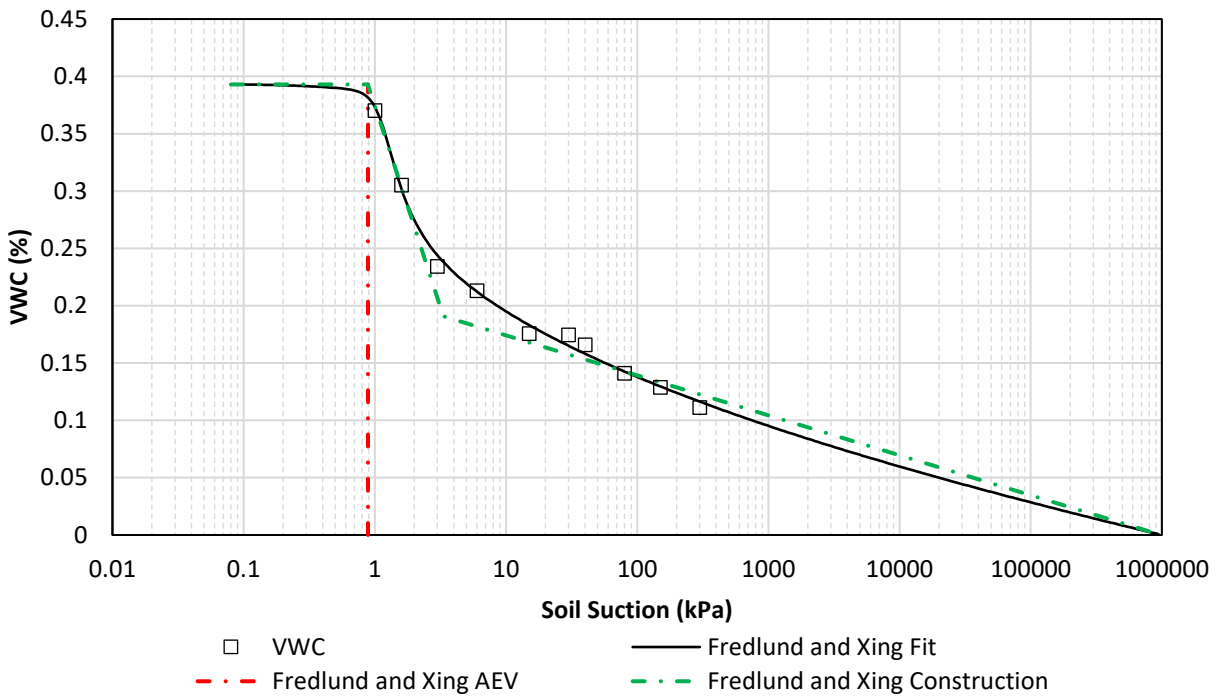


Figure I.20. Soil-water characteristic curve for second Control Subballast test.

Table I.27. Soil-water characteristic curve test data for first Subgrade test.

SWCC - Subgrade						
		Volume			Final water content	
cell (g)	1664.59		Dia.(cm)	6.9	tare (g)	3.68
cell+sample (g)	1828.01		Initial height (cm)	3.83	tare+wet (g)	216.43
			Initial vol. (cm3)	143.2	tare+dry (g)	197.76
sample (g)	220.87		Final volume			
water (g)	26.79		Final height (cm)	3		
soil (g)	194.08		Dia. (cm)	6.9		
w.c. (%)	0.138		Final vol. (cm3)	112.2		
suction	weight	w.c.	final w.c. (Grav.)	vol. w.c.	Grav. W.C.	Vol. W.C.
(kPa)	(g)		(dec.)	(dec.)	(%)	(%)
0.1	1885.46	0.434048	0.365	0.504	36.56	50.4
0.2	1885.04	0.431884	0.363	0.501	36.34	50.1
0.3	1884.64	0.429823	0.361	0.498	36.13	49.8
0.5	1881.87	0.41555	0.347	0.478	34.71	47.8
1	1864.15	0.324248	0.256	0.352	25.58	35.2
2	1861.47	0.310439	0.242	0.333	24.20	33.3
3	1861.47	0.310439	0.242	0.333	24.20	33.3
6	1851.66	0.259893	0.191	0.264	19.1	26.7
10	1849.6	0.249279	0.181	0.249	18.1	24.9
30	1844.04	0.220631	0.152	0.210	15.2	21.0
80	1846.52	0.233409	0.165	0.227	16.5	22.7
150	1833.18	0.164674	0.096	0.133	9.6	13.3

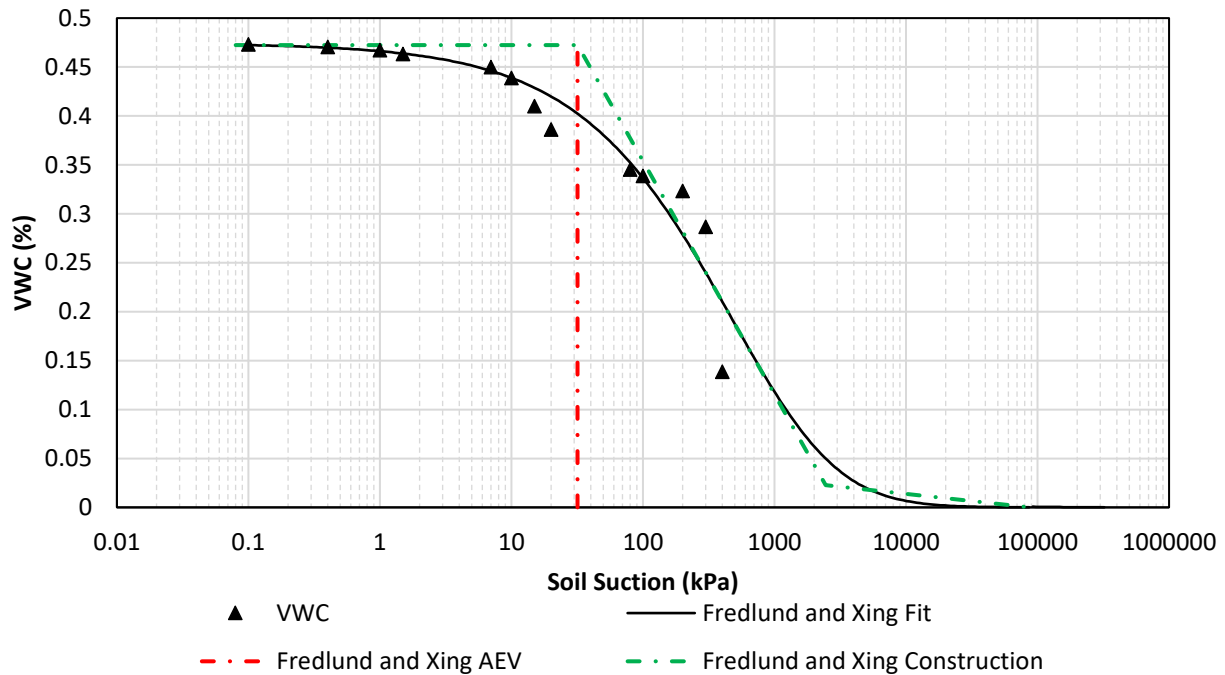


Figure I.21. Soil-water characteristic curve for first Subgrade test.

Table I.27. Soil-water characteristic curve test data for second Subgrade test.

SWCC - Subgrade						
		Volume			Final water content	
cell (g)	1627.1		Dia.(cm)	6.9	tare (g)	3.7
cell+sample (g)	1828.01		Initial height (cm)	3.83	tare+wet (g)	232.59
			Initial vol. (cm3)	143.2144	tare+dry (g)	229.62
sample (g)	279.4		Final volume			
water (g)	78.49		Final height (cm)	3.63		
soil (g)	200.91		Dia. (cm)	6.9		
w.c. (%)	0.39067244		Final vol. (cm3)	135.7359		
suction	weight	w.c.	final w.c. (Grav.)	vol. w.c.	Grav. W.C.	Vol. W.C.
(kPa)	(g)		(dec.)	(dec.)	(%)	(%)
0.1	1906.5	0.781345	0.381066	0.484178	38.10661	48.41783
0.2	1905.82	0.77796	0.377682	0.479878	37.76815	47.98779
0.5	1904.81	0.772933	0.372654	0.47349	37.26544	47.34905
1	1904.65	0.772137	0.371858	0.472479	37.1858	47.24786
5	1904.5	0.77139	0.371111	0.47153	37.11114	47.153
10	1901.75	0.757702	0.357424	0.454139	35.74237	45.41385
20	1896.15	0.729829	0.329551	0.418723	32.95505	41.87232
80	1882.26	0.660694	0.260415	0.33088	26.04151	33.08805
100	1880.69	0.652879	0.252601	0.320952	25.26007	32.09515
200	1876.01	0.629585	0.229307	0.291354	22.93067	29.13544
300	1868.17	0.590563	0.190284	0.241773	19.02842	24.17729
400	1832.91	0.415061	0.014783	0.018783	1.478274	1.878278

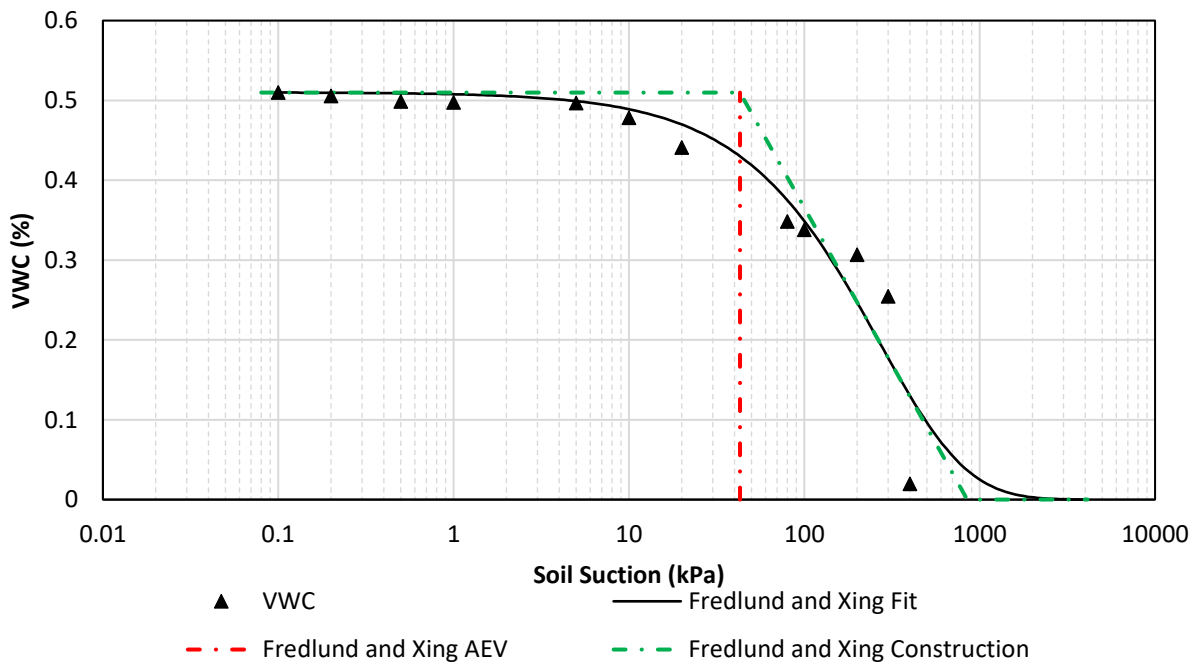


Figure I.22. Soil-water characteristic curve for second Subgrade test.

I.6- Field Density Test

Table I.28. Field density data from the subgrade material.

Density of Soil in Place by the Sand-Cone Method (T 191)					
Field Density Test Station:	1	2	3		
Offset:					
Orig. Mass Jar, Cone & Sand, g (G):	5442.00	5461.00	3845.00		
Final Mass Jar, Cone & Sand, g (H):	1078.00	1514.00	651.00		
Mass of Sand Used, g (I): (G- H)	4364.00	3947.00	3194.00		
Moist Mass, Container & total Material from hole, g (J):	3941.50	4343.50	3105.50		
Mass Container, g (K):	82.00	330.50	83.50		
Moist Mass, total material from hole, g (L): (J- K)	3859.50	4013.00	3022.00		
Wet Mass, Moisture Sample & tin, g (M):	164.0	251.0	274.0		
Mass of tin, g (N):	3.5	3.5	3.5		
Wet Mass Moisture Sample, g (O): (M - N)	160.5	247.5	252.5		
Dry Mass Moisture Sample & Tin, g (P):	133.0	215.0	273.5		
Dry Mass Moisture Sample, g (Q): (P - N)	129.5	211.5	214.5		
Moisture Content, % (R): ((O - Q)/Q)	23.9%	17.0%	17.7%		
Dry Mass of Materials from test hole, g (S): (L / (1 + R))	3115.0	3429.9	2567.5	Average	
Vol. of Hole, cm ³ (T): (I - F) / C	1934.1	1702.5	1284.1		
Dry Density of Tested Material, g/cm ³ (U): (S / T)	1.6	2.0	2.0	1.9	

APPENDIX II – Sensor Calibration Results

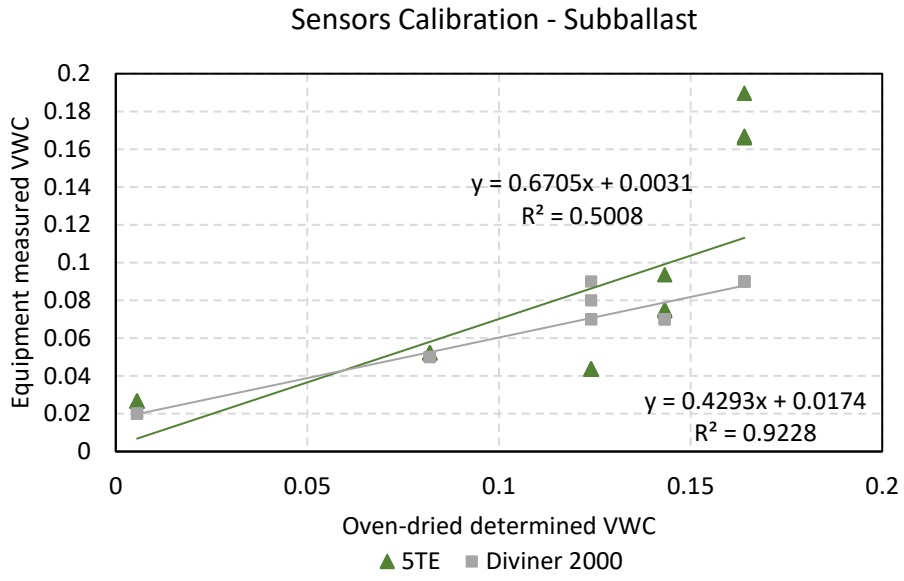


Figure II.0.1. Diviner and 5TE sensor calibration for Clean Sub-ballast.

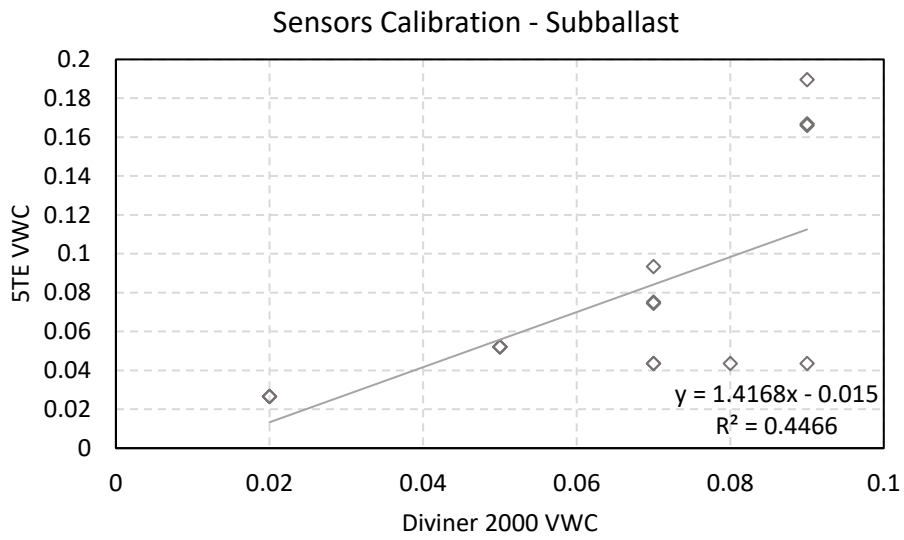


Figure II.0.2. Diviner vs. 5TE measurements for Clean Sub-ballast.

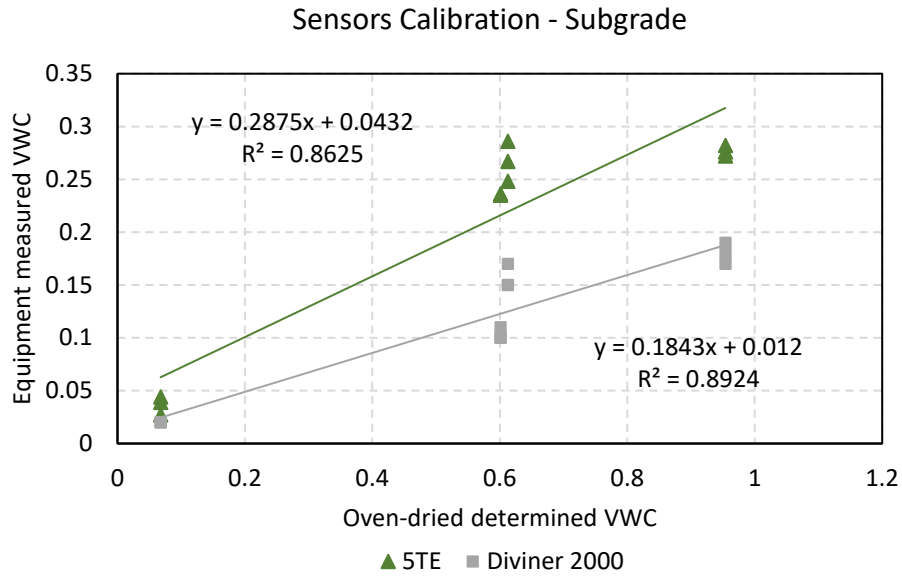


Figure II.0.3. Diviner and 5TE sensor calibration for Subgrade.

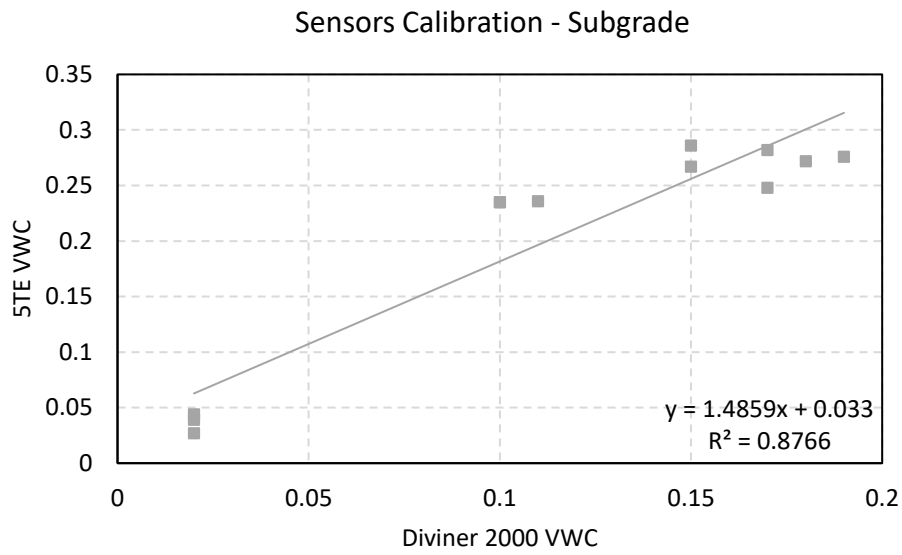


Figure II.0.4 Diviner vs. 5TE measurements for Subgrade.